Titre: Title:	Evaluation of Hyperthermia Using Magnetic Nanoparticles and Alternating Magnetic Field
Auteur: Author:	Seyed Nasrollah Tabatabaei Shafie
Date:	2010
Type:	Mémoire ou thèse / Dissertation or Thesis
Référence: Citation:	Tabatabaei Shafie, S. N. (2010). Evaluation of Hyperthermia Using Magnetic Nanoparticles and Alternating Magnetic Field [Mémoire de maîtrise, École Polytechnique de Montréal]. PolyPublie. https://publications.polymtl.ca/300/

UNIVERSITÉ DE MONTRÉAL

EVALUATION OF HYPERTHERMIA USING MAGNETIC NANOPARTICLES AND ALTERNATING MAGNETIC FIELD

SEYED NASROLLAH TABATABAEI SHAFIE

INSTITUT DE GÉNIE BIOMÉDICAL

ÉCOLE POLYTECHNIQUE DE MONTRÉAL

MÉMOIRE PRÉSENTÉ EN VUE DE L'OBTENTION

DU DIPLÔME DE MAÎTRISE ÈS SCIENCES APPLIQUÉES

(GÉNIE BIOMÉDICAL)

AVRIL 2010

UNIVERSITÉ DE MONTRÉAL

ÉCOLE POLYTECHNIQUE DE MONTRÉAL

Ce mémoire intitulé:

EVALUATION OF HYPERTHERMIA USING MAGNETIC NANOPARTICLES AND ALTERNATING MAGNETIC FIELD

présenté par : TABATABAEI SHAFIE, Seyed Nasrollah

en vue de l'obtention du diplôme de : Maîtrise ès sciences appliquées

a été dûment accepté par le jury d'examen constitué de :

M. SAVARD Pierre, Ph.D., président

M. MARTEL Sylvain, Ph.D., membre et directeur de recherche

M. MÉNARD David, Ph.D., membre

DEDICATION

First and foremost I would like to thank my research advisor, **Dr. Sylvain Martel**. His belief in me and my decision to continue graduate studies in nanotechnology provided motivation to achieve goals I would not have imagined possible.

In addition to Dr. Martel's mentorship, I appreciate **Dr. Pierre Savard** (Dept. of Biomedical Engineering) and **Dr. David Menard** (Dept. of Engineering Physics) for always taking time for technical discussions and sharing ideas when necessary. I would like to thank the kind staff of École Polytechnique de Montréal and particularly **Mme. Francine Cournoyer** for all her administrative help and support.

It was an honour conducting research at **Nanorobotics Laboratory** with its unique liberal, friendly yet professional environment. I dearly thank **Ouajdi Falfoul** and **Dr. Jean-Baptiste Mathieu** for their honest friendship and patience while answering my questions (regardless of how dull they may have sounded like), I thank **Charles Tremblay** for his great technical support and tolerance in the lab (even when I left my coat on the back of my chair), **Pierre Pouponneau** for providing insight into the chemistry of nanoparticles (and never forgot that I once splashed nanoparticles on my shirt), my best Jewish-American friend **Evan Shechter** for his help with the scientific grammar and interesting political discussions, **Dr. Mahmood Mohammadi** for assisting me to exercise my beliefs, and special thanks to **Jacinthe Lapointe** for her support on different component of the same research project. Also my appreciation goes to all of my lab mates: **Dr. Neila Kaou, Nisryn Mokrani, Oualid El Halimi, Gael Bringout, Vivian Lalande, Manuel Vonthron, Nina Olamaei, Elmira Khoshbakht Marvi, Samira Taherkhani, Ke Peng, Fatemeh Afkhami** and **Frederick Gosselin** for their friendship and help to create an exciting research atmosphere.

Great gratitude goes to my family for their support of all my life choices. My parents, **Reza** and **Monir**, I dedicate this to you for you have never limited my dreams and provided me with all I have ever asked for and more. You are the reason I have any interest in science and higher education. I thank my sister, **Zahra**, for being a significant source of moral support. My younger sisters, **Maryam** and **Mahdieh**, I thank you for your constant spiritual support. I would like to

thank my grandmother, **Ozma Khanoum**, my aunt, **Dr. Diana Tabatabaei**, and my uncle, **Dr. Jamshid Etezadi**, for believing in me and guiding me through life as their son during the past three years. Finally and certainly not least, I would like to thank my beloved wife, **Mona**, for being the light of my life and simply *being*; your faith in me is cherished.

"There is only one virtue in the world, knowledge, and only one sin, ignorance, and in between, having open eyes or being blind is the difference between an informed and an uninformed man"

- *Avicenna*

ACKNOWLEDGMENT

This project is supported in part by a Canada Research Chair (CRC) in Micro/Nanosystem Development, Fabrication and Validation, the Canada Foundation for Innovation (CFI), the National Sciences and Engineering Research Council of Canada (NSERC), and the Fonds Québécois de Recherche sur la Nature et les Technologies (FQRNT). This work was also supported by US grant Number R21EB007506 from the National Institute Of Biomedical Imaging And Bioengineering. The content is solely the responsibility of the authors and does not necessarily represent the official views of the National Institute of Imaging And Bioengineering or the National Institutes of Health.

RÉSUMÉ

Pendant des années, l'élévation de la température du corps, connu sous le nom d'hyperthermie, a été utilisée pour traiter les cellules cancéreuses. L'hyperthermie peut être atteinte via diverses méthodes invasives et non invasives, dont certaines sont pratiquées aux niveaux de la recherche clinique, et certaines autres ont déjà atteint l'approbation pour la pratique en clinique. Les nanoparticules magnétiques (NPM) peuvent générer de la chaleur et donc chauffer leur entourage une fois qu'ils sont placés dans un champ magnétique alternatif. Contrairement aux autres méthodes d'hyperthermie, l'hyperthermie par NPM utilisant un champ magnétique alternatif fournit un contrôle avancé et peut avoir un effet très localisé. En plus, les NPM ont un énorme potentiel pour les applications biomédicales d'imagerie, de diagnostic et de traitements. En plus, les NPM peuvent être propulsées par les gradients magnétiques vers un emplacement désiré du corps. La propulsion et le contrôle et l'hyperthermie permettent l'introduction d'un système robotique miniaturisé pour les applications thérapeutiques localisées. En effet, une fois chargé avec des agents thérapeutiques, les NPM peuvent être propulsées, ciblés vers l'organe malade et ensuite chauffés utilisant des champs magnétiques alternatifs qui induira une séquence d'actionnement des médicaments. Dans ce mémoire, les attributs physiques des NPM tel que l'aimantation, les domaines magnétiques, l'hystérésis, la relaxation et ainsi que divers mécanismes de chauffage sont étudiés. Aussi les limites biologiques qui permettent de déterminer la fréquence et l'intensité des champs magnétiques alternatifs utilisés pour l'hyperthermie sont expliquées.

Des NPM commercialement disponibles ont été utilisées pour étudier l'effet de la concentration sur l'élévation de température. Ainsi des échantillons de 1ml de magnétite en forme de fluide (ferrofluides) dont le diamètre des particules se situe entre 5 à 10 nm comprenant une couche de dextran ont été utilisés. Les tests sont réalisés avec des concentrations de 10, 25 et 50 mg/ml de ferrofluide. Les échantillons isolés avec polystyrène (Styrofoam) ont été chauffés par une bobine d'induction générant un champ magnétique alternatif d'environ 80 kA m^{-1} à 150 kHz. Après 900 secondes, les échantillons ont montré 11,11°C, 27,78°C et 55,56°C d'élévation de température ΔT respectivement.

Pour examiner l'effet des couches enrobant les NPM sur l'élévation de la température, différents types d'enrobage a été expérimentés. Les différents enrobages sont l'amidon, l'acide oléique,

Polyacrylamide, Poly (acide maléique-co-oléfines), l'alcool de polyvinyle, SiMAG carboxyle, nanoparticules non couchés chargé anionique et cationique. Un échantillon de 0,5 ml de 25 mg/ml de NPM avec chaque enrobage a été placé à l'intérieur d'un champ magnétique alternatif de 2 kA m^{-1} à 160 kHz pour 3000 secondes. Le débit d'absorption spécifique (SAR) estimé à partir du graphe de l'élévation de la température en fonction du temps et le SAR obtenu utilisant la courbe d'hystérésis ont été comparés. Les équations thermodynamiques ont été utilisées pour tracer la distribution de chaleur en fonction du temps et de la distance, les simulations obtenues sont en corrélation avec les résultats expérimentaux. Un échantillon de 1 ml de fluidMAG-PMO-2 a été aussi placé à l'intérieur d'un bécher qui contenait de l'eau déminéralisée à 37ºC et été agité à 50 rpm. La température de l'échantillon atteint 42,44ºC lorsque un champ magnétique alternatif de 4,5 kA m^{-1} à 160 kHz est appliqué pour 1680 secondes.

Enfin, les NPM encapsulés dans les hydrogels thermosensibles (NPM-PNIPA), servant comme mécanisme d'actionnement des médicaments par hyperthermie ont été testés. Les chaînes de polymère d'hydrogel expulsent leur contenu liquide quand ils atteignent la température critique (LCST) résultant dans la réduction du volume de ces derniers. Ici, 0,5 ml de NPM-PNIA avec une concentration de 5 et 10 mg magnétite /ml ont été placés dans un gel d'agar et aussi dans du Styrofoam et soumis à un champ magnétique alternatif de 9,2 kA m^{-1} à 145 kHz. Après 30 minutes, une élévation maximum de 2,9°C pour la concentration de 5 mg magnétite/ml de NPM-PNIA et 3,3°C pour la concentration de 10 mg magnétite/ml a été enregistrée dans le gel d'agar. Pour Styrofoam l'élévation maximum de température obtenue est de 2,1°C et 4,4°C pour les concentrations de 5 et 10 mg magnétite/ml, respectivement. Aussi un changement de volume remarquable dans NPM-PNIA ayant 10 mg magnétite/ml a été observé. Ensuite, près de 100 NPM-PNIA sphères (diamètre d'environ 1mm) ont été placées dans un champ magnétique alternatif de 4 kA m^{-1} à 160 kHz. Après 1500 secondes, une élévation de 2°C a été observée.

Dans ce mémoire, l'hyperthermie via l'induction du NPM a été étudiée. L'effet de la concentration des NPM et certains enrobages ont été évalués. Des NPM-PNIA sphériques ont été aussi chauffées avec l'induction d'un champ magnétique alternatif. En raison de la présence des NPM, l'hydrogel NPM-PNIA peut être propulsé par le gradient d'un champ magnétique tel que celui d'un système d'Imagerie par Résonance Magnétique (IRM). Une fois que ces hydrogels contenant des agents thérapeutiques atteignent leur cible, un champ magnétique alternatif respectant les limites physiologiques tolérables est capable d'induire suffisamment de chaleur

pour réduire leur volume et donc actionner une séquence locale de libération du médicament. Il s'agit d'un pas de plus vers la libération ciblée d'agents thérapeutiques actionnée par l’hyperthermie induite par des champs magnétiques alternatifs.

ABSTRACT

Elevation of body temperature, otherwise known as hyperthermia, has been used to treat cancerous cells for many decades. Hyperthermia can be achieved via various invasive and non-invasive methods, some of which are being practiced at clinical levels, and some others have already reached clinical trials. Magnetic nanoparticles (MNP) can generate heat and thus heat their surroundings once they are placed in an alternating magnetic field (AC magnetic field). In contrast to other hyperthermia methods, hyperthermia via MNP in an AC magnetic field provides advanced control and can be highly localized. In addition, MNP have enormous potential in biomedical applications such as imaging, medical diagnosis and treatment. Also, agglomeration of MNP can be propelled with an inhomogeneous magnetic field towards a desired location. The propulsion, control and hyperthermia allow the introduction of a miniaturized robotic system. Indeed, MNP micro-carriers loaded with therapeutic agents can be propelled and tracked to a specific diseased organ and be heated upon exposure to the AC magnetic field and then begin hyperthermia and drug actuation sequence. In this thesis, the physical attributes of the MNP such as the magnetization, magnetic domains, hysteresis, and relaxations as well as various heating mechanisms are discussed. Also biological limits that determine the frequency and the intensity of AC magnetic fields used for hyperthermia are explained.

Commercially available MNP were used to study the concentration effect of the MNP on the temperature. Thus, samples of 1ml of magnetite in the form of fluid (ferrofluids) whose particle diameter were between 5 to 10 nm with a layer of dextran coating were used. The tests were performed with concentrations of 10, 25 and 50 mg / ml of ferrofluid. The insulated samples by Styrofoam were heated by an induction coil generating an AC magnetic field near 80 kA m^{-1} at 150 kHz. After 900 seconds, the samples showed 11.11°C, 27.78°C and 55.56°C temperature elevations respectively.

To examine the effect of the coating of the MNP on the rise in temperature, various types of coating was tested. The coatings were Starch, Oleic acid, Polyacrylamide, Poly (maleic acid-co-olefin), Polyvinyl alcohol, SiMAG Carboxyl, uncoated anionic and cationic charge magnetite nanoparticles. Therefore, 0.5 ml of 25 mg/ml of each coating was placed inside an AC magnetic field of 2 kA m^{-1} at 160 kHz for 3000 seconds. The SAR estimated from the graph of the temperature rise as function of time and the SAR obtained using the hysteresis curve were

compared. The thermodynamic simulations correlated closely with the experimental plots of the distribution of temperature as function of time and distance.

A 1ml sample of fluidMAG-PMO-2 was placed inside of a beaker that contained deionised water at 37ºC and was stirred at 50 rpm. The sample temperature reached 42.44ºC when AC magnetic field of 4.5 kA m^{-1} at 160 kHz was applied for 1680 seconds.

Finally, MNP encapsulated within thermo-sensitive hydrogels (MNP-PNIPA) serving as a mechanism of actuation of drug release by hyperthermia were tested. The hydrogel polymer chains collapse and expel the liquid content when they reach the critical solution temperature (LCST) resulting in the reduction of the volume of the latter. Here, 0.5 ml MNP-PNIPA samples with a concentration of 5 and 10 mg magnetite/ml were placed once in agar gel and once in an agar gel and also in the Styrofoam and subjected to an AC magnetic field of 9.2 kA m^{-1} to 145 kHz. After 30 minutes, a maximum elevation of 2.9°C for the concentration of 5 mg magnetite/ml MNP-PNIPA and 3.3°C for a concentration of 10 mg magnetite/ml was recorded in the agar gel. The maximum temperature rise for Styrofoam was 2.1°C and 4.4°C respectively. Also remarkable change of volume in MNP-PNIPA of 10 mg magnetite/ml was observed. Then, nearly 100 MNP-PNIA spheres (about 1mm diameter) were placed in an alternating magnetic field of 4 kA m^{-1} to 160 kHz. After 1500 seconds, a rise of 2°C was observed.

In this thesis, hyperthermia via induction of MNP has been studied. The effect of the concentration of MNP and some coatings were evaluated. The NPM-spherical PNIPA were also heated with the induction of an alternating magnetic field. Due to the presence of MNP, the MNP-PNIPA hydrogel can be propelled by the gradient of a magnetic field such as that of magnetic resonance imaging (MRI). Once these hydrogels containing therapeutic agents reach their target, an AC magnetic field within the tolerable physiological limits is able to induce sufficient heat to reduce their volume and thus activate a sequence of local drug release. This is a step closer to the targeted delivery of therapeutic agents activated by hyperthermia and induced by AC magnetic fields.

CONDENSÉ EN FRANÇAIS

Chapitre 1

Cancer

Des cellules cancéreuses peuvent être produites en raison de facteurs externes comme le tabac, les produits chimiques, les radiations et les organismes infectieux ainsi que des facteurs internes, tels que les mutations héréditaires, les hormones, les facteurs immunitaires et les mutations qui se produisent dans le métabolisme. Lorsque les cellules cancéreuses sont produites sans retenue, une tumeur se forme.

Hyperthermie

L'hyperthermie est définie comme une élévation anormale de la température. En oncologie, l'hyperthermie se définie par l'échauffement d'organes ou de tissus à des températures entre 40°C et 45°C, à un point qui provoque l'inactivation cellulaire modérée et réversible. L'hyperthermie peut être considérée comme une thérapie complémentaire qui maximise l'effet des agents chimiothérapeutiques et de la radiothérapie. Les données disponibles suggèrent que l'hyperthermie modérée, inférieure à 42°C, augmente le flux sanguin vers la tumeur. Ce qui entraîne une meilleure oxygénation ainsi qu'une hausse de l'apport nutritif à la tumeur. Parmi les différentes applications de l'hyperthermie, l'actionnement est d'un grand intérêt lorsque l'hyperthermie localisée est utilisé pour déclencher un mécanisme de libération du médicament.

Les Méthodes d'Hyperthermie

1. L'hyperthermie de l'ensemble du corps: Dans cette méthode, tout le corps est chauffé, soit en empêchant le transfert de chaleur du corps vers le milieu environnant, ou en plaçant le patient dans un bain d'eau chauffée.
2. L'hyperthermie par des applicateurs sans fil:
    a. Ultrasons focalisés de haute intensité (HIFU)

        Des ondes ultrasonores focalisées sont transmises à des tissus mous, ce qui cause des frictions moléculaires et de la chaleur mécanique. Les HIFU ne sont pas idéaux pour les zones situées près des os ou de l'air.

b. Applicateurs électromagnétiques (technique non invasive):
    i. Radiofréquence (RF): la technique de thermothérapie est basée sur le courant qui est induit par les ondes RF (0.5 - 300 MHz) dans un tissu biologique pour osciller les électrons libres et les ions. La chaleur est produite par la collision de ces électrons et ions avec des atomes immobiles.
    ii. L'antenne capacitive: la région d'intérêt du corps est placée entre deux plaques chargées. Un champ électrique induit entre ces plaques génère de la chaleur dans les tissus indépendamment de la profondeur de cible. Toutefois la graisse autour du tissu cible peut provoquer un échauffement superficiel excessif.
    iii. L'antenne inductive: La bobine d'induction crée des courants de Foucault dans le tissu et augmente la température. Cette chaleur est liée à la conductivité électrique du tissu. La variation de la conductivité des tissus peut provoquer une température non-uniforme.

c. Micro-ondes: Basé sur le principe de chauffage diélectrique, les molécules d'eau absorbent l'énergie des micro-ondes. Étant donné que ces molécules contiennent des charges positives et négatives - les molécules d'eau sont bipolaires - elles essaient de s'aligner avec le champ électromagnétique des micro-ondes. Due à la haute fréquence, le mouvement moléculaire rapide provoque une élévation locale de la température.

3. Insertion de source(s) de chaleur (technique invasive): Des sources d'hyperthermie sont chirurgicalement placées à l'intérieur ou autour de la zone cible:
    a. Chauffage micro-ondes: ondes électromagnétiques d'antennes micro-ondes insérées à l'intérieur du tissu
    b. Chauffage par radiofréquences: l'insertion d'une paire ou d'un réseau d'électrodes RF macroscopiques à l'intérieur du tissu.
    c. Semences ferromagnétiques: des semences ferromagnétiques, aussi grandes que quelques centimètres, sont implantées et placées dans un champ magnétique oscillant.
    d. Nanoparticules: production de chaleur à partir de nanoparticules.

Chapitre 2

Les deux composantes du champ électromagnétique, plus précisément, le champ électrique ainsi que la variation du champ magnétique, sont responsables de la production de chaleur dans un tissu. Les effets thermiques sont déterminés par les propriétés diélectriques du tissu et les propriétés magnétiques du milieu. Étant donné que les matières biologiques n'ont pas d'importantes propriétés magnétiques, les nanoparticules magnétiques, ou NPM, biocompatibles sont utilisées pour augmenter l'influence de la variation du champ magnétique. Dans ce projet, l'accent est mis sur la composante magnétique d'un champ électromagnétique de basse fréquence.

Les nanoparticules magnétiques en hyperthermie

Les NPM composée de métaux comme le fer, le cobalt et le nickel et leurs alliages sont utiles en raison de leurs propriétés magnétiques et multifonctionnelles. Ces nanoparticules sont capables de créer de la chaleur une fois placées dans un champ magnétique alternatif externe. Parmi les compositions chimiques différentes des NPM, l'oxyde de fer a été le plus utilisé pour l'hyperthermie. Cela est dû à sa biocompatibilité, sa biodégradabilité et sa faible toxicité.

Génération de chaleur des NPM utilisant un champ magnétique alternatif

La chaleur générée par les NPM soumises à un champ magnétique alternatif (champ magnétique AC) est principalement causée par les trois mécanismes suivants: perte par hystérésis, relaxation brownien et de Néel.

Les domaines magnétiques contiennent un grand nombre de moments magnétiques atomiques. En l'absence d'un champ magnétique externe, les moments magnétiques sont alignés le long des axes cristallographiques magnétiques appelés « axes faciles ». L'énergie nécessaire pour faire pivoter les domaines magnétiques avec un champ magnétique externe est appelée anisotropie de l'énergie E = KV, où K est la constante d'anisotropie effective et V est le volume du noyau magnétique.

Les matériaux ferromagnétiques qui se composent de plusieurs domaines magnétiques sont appelés matériaux multi-domaines. Lorsque ces matériaux sont soumis à une augmentation et une diminution du champ magnétique externe H, la courbe d'aimantation ne coïncide pas. Par conséquent, le matériel démontre «un comportement d'hystérésis» et des pertes par hystérésis se manifestent par transfert de chaleur vers le milieu environnant. Mathématiquement, le taux

d'absorption spécifique (SAR) est proportionnel au produit de la fréquence par l'intégrale fermée de la boucle d'hystérésis. En d'autres termes, plus la zone à l'intérieur de la boucle est grande, plus il y a de chaleur dissipée dans la région environnante. Toutefois, pour bénéficier de la génération de chaleur d'une boucle d'hystérésis complète, les particules doivent être saturées avec des champs magnétiques élevés de l'ordre de quelques milliers d'Oersted, ce qui ne convient pas pour le corps humain.

Une fois soumis à un champ magnétique externe alternatif, le matériau magnétique présente un cycle d'hystérésis étroit. L'orientation des moments magnétiques de ces particules, appelées particules superparamagnétiques, change continuellement, ce qui empêche les pertes par hystérésis de se produire. Dans un champ magnétique alternatif de haute amplitude, l'énergie peut permettre aux moments magnétiques de s'aligner le long de la direction du champ externe en surmontant la barrière d'énergie thermique. Cependant, une fois que le champ magnétique externe est enlevé, les moments magnétiques prennent un certain temps à perdre cet alignement. Ceci est connu comme le mécanisme de relaxation de Néel qui peut également provoquer une libération d'énergie sous forme de chaleur.

Le troisième mécanisme de chauffage est la relaxation brownienne qui survient à la fois sur les multi-domaines et les particules n'ayant qu'un seul domaine. Le temps de relaxation brownien, τB, est défini comme le temps que prend la particule à tourner sous l'influence du champ magnétique externe, de la viscosité du milieu, ainsi que du volume hydrodynamique des particules.

Débit d'absorption spécifique (SAR)

Le SAR (W g-1) est proportionnel au taux de variation de la température du matériau magnétique et il est donné par la formule suivante:

$$SAR = \frac{c\,V_s}{m}\frac{dT}{dt}$$

où c est la capacité thermique spécifique de l'échantillon (4.185 J l^{-1} K^{-1} pour l'eau), m est la masse des particules magnétiques, V_s représente le volume de l'échantillon et $\frac{dT}{dt}$ exprimée en °Ks^{-1} est la variation de température qui est obtenue de façon expérimentale.

Dissipation thermique

En théorie, l'énergie provenant des particules magnétiques uniformément distribuées à l'intérieur d'une tumeur sphérique de rayon R soumis à un champ magnétique alternatif dissipera la chaleur aux tissus environnants tant que la température n'atteindra pas l'état d'équilibre. La figure 1, dans laquelle *r* représente la distance entre le centre du volume sphérique et un point à l'infini, illustre ce concept.

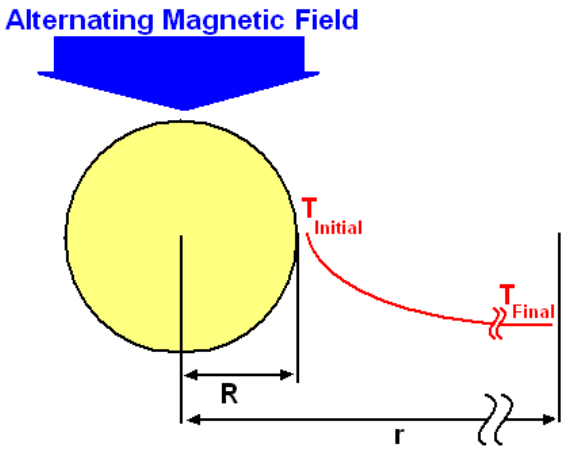

Figure 1. La température en fonction de la distance

Les équations thermodynamiques de transfert de chaleur en fonction du temps (figure 2) aident à optimiser et prédire le temps d'exposition nécessaire afin d'élever la température des tissus jusqu'à une température cible respectant les limites physiologiques.

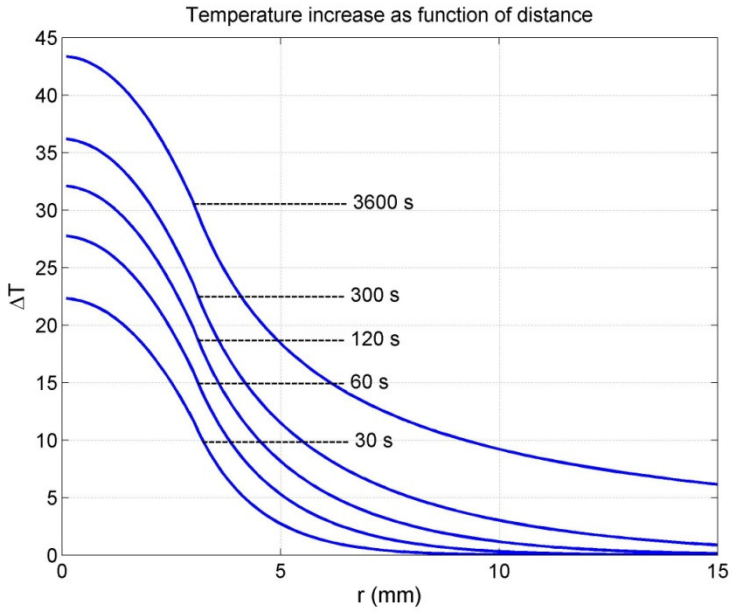

Figure 2. Simulation MATLAB® pour augmentation de la température en fonction de la distance (Appendis A.3)

Les propriétés magnétiques adaptées à l'hyperthermie

Les propriétés magnétiques adaptées à l'hyperthermie ne sont pas seulement régies par les paramètres magnétiques des NPM, mais aussi par les limites physiologiques qui sont conçues pour protéger les organismes vivants contre les champs magnétiques élevés. Ces paramètres sont la taille, la concentration des NPM, les limites maximales de l'amplitude et de la fréquence du champ magnétique alternatif.

Hydrogel

Le PPNIPA est un hydrogel qui réduit sa taille lorsqu'il est chauffé et se gonfle lorsqu'il est refroidi. Ce mécanisme discontinu et réversible se produit à une température de transition appelée LCST (Lower Critical Solution Temperature). Aux températures inférieures au LCST, les liaisons hydrogènes entre les groupes hydrophiles de la chaîne polymère sont dominantes. Lorsque la température est élevée au dessus du LCST, les liaisons hydrogènes deviennent faibles et les liaisons hydrophobes deviennent plus fortes. Ainsi l'eau est expulsée hors de l'hydrogel. Ce phénomène entraîne un changement de couleur (l'hydrogel devient opaque) et un changement de volume. Le LCST du PPNIPA est autour de 32 ° C, et peut être augmenté au-dessus de la

température corporelle. Dans notre cas, le LCST pour le PPNIPA contenant des NPM a été déterminé à 29 ° C (figure 3).

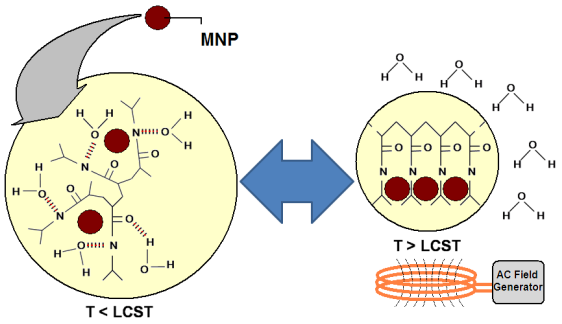

Figure 3. Des NPM incorporées dans l'hydrogel PNIPA

NPM et le gradient de champ magnétique

Le gradient de champ magnétique de l'IRM permet d'orienter l'agglomération des NPM. La force créée à l'intérieur de l'IRM peut être calculée à partir de l'équation suivante :

$$\vec{F} = \left(V\vec{\mathbf{M}}.\boldsymbol{\nabla}\right)\vec{\mathbf{B}}$$

Dans l'équation ci-dessus, $\vec{F}$ est la force magnétique (N), $\vec{\mathbf{M}}$ est l'aimantation du matériau (A m^{-1}), V est le volume du matériau magnétique (m^3), $\vec{\mathbf{B}}$ est l'induction magnétique (T) et ∇B est le gradient (variation spatiale) de l'induction magnétique (T m^{-1}).

Chapitre 3

Effet de la concentration sur la génération de chaleur

Des NPM commercialement disponibles ont été utilisées pour étudier l'effet de la concentration sur l'élévation de température. Ainsi des échantillons de 1ml de nanoparticules de magnétite en dispersion (ferrofluides), dont le diamètre se situe entre 5 et 10 nm et recouvertes d'une couche de dextran, ont été utilisés. Les tests sont réalisés avec des concentrations de 10, 25 et 50 mg/ml de ferrofluide. Les échantillons isolés avec du polystyrène (Styrofoam) ont été chauffés par une bobine d'induction générant un champ magnétique alternatif d'environ 80 kA m^{-1} à 150

kHz. Après 900 secondes, les échantillons ont montré 11.11°C, 27.78°C et 55.56°C d'élévation de température ΔT respectivement.

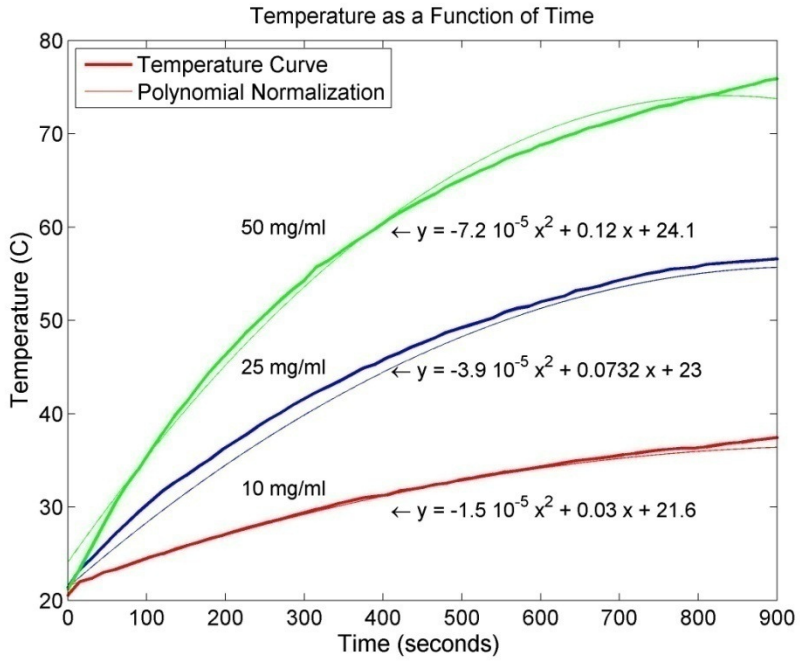

Figure 4. Élévation de la température en fonction de temps

Effet du revêtement des MNP sur la génération de chaleur

Différents types de couches recouvrant les NPM ont été expérimentés, pour examiner leur effet sur l'élévation de la température. Les différents enrobages sont l'amidon, l'acide oléique, le polyacrylamide, le poly (acide maléique-co-oléfines), l'alcool de polyvinyle, SiMAG carboxyle, ainsi que des nanoparticules non enrobées chargées positivement et négativement. Un échantillon de 0,5 ml de NPM à 25 mg/ml avec chaque enrobage a été placé à l'intérieur d'un champ magnétique alternatif de 2 kA m^{-1} à 160 kHz pour 3000 secondes (Figure 5). Le SAR estimé à partir du graphe de l'élévation de la température en fonction du temps et le SAR obtenu utilisant la courbe d'hystérésis ont été comparés. Les équations thermodynamiques ont été utilisées pour tracer la distribution de chaleur en fonction du temps et de la distance. Les simulations obtenues sont en corrélation avec les résultats expérimentaux.

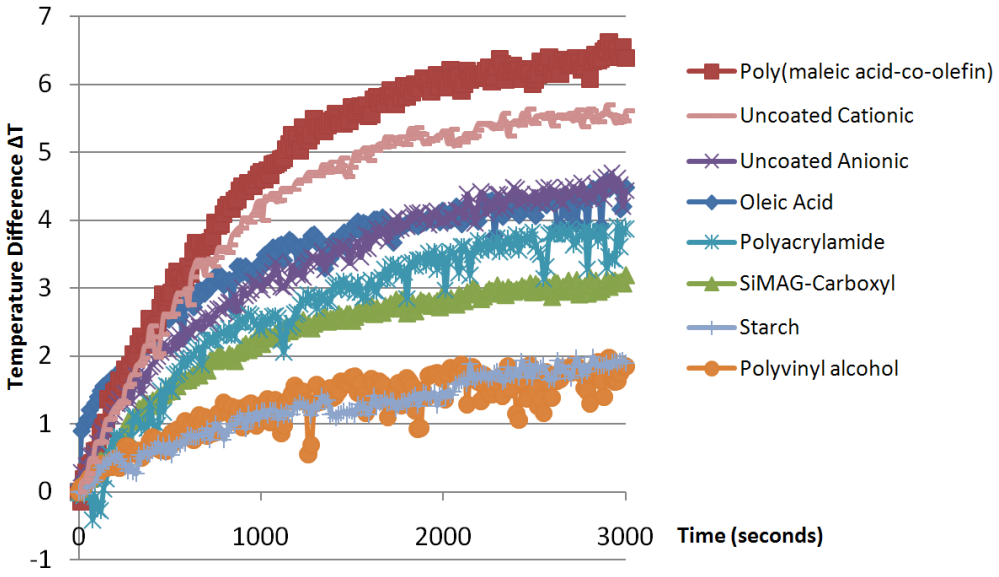

Figure 5. Effet de l'enrobage des NPM sur l'hyperthermie

Un échantillon de 1 ml de fluidMAG-PMO-2 a été aussi placé à l'intérieur d'un bécher qui contenait de l'eau déminéralisée à 37ºC et a été agité à 50 rpm. La température de l'échantillon a atteint 42,44ºC lorsque un champ magnétique alternatif de 4,5 kA m^{-1} à 160 kHz a été appliqué pour 1680 secondes.

NPM encapsulées dans l'hydrogel

Enfin, les NPM encapsulées dans les hydrogels thermosensibles (NPM-PPNIPA), servant comme mécanisme d'actionnement de la libération des médicaments par hyperthermie ont été testées. Les chaînes de polymère d'hydrogel expulsent leur contenu liquide quand ils atteignent la température critique (LCST), menant à la réduction du volume de l'hydrogel. Ici, des échantillons de 0,5 ml de NPM-PPNIPA avec des concentrations de 5 et de 10 mg de magnétite par ml ont été placés dans un gel d'agar et ont été soumis à un champ magnétique alternatif de 9,2 kA m^{-1} à 145 kHz. Après 30 minutes, une élévation maximale de 2,9°C a été enregistrée pour la concentration de 5 mg magnétite/ml de NPM-PNIA et de 3,3°C pour la concentration de 10 mg magnétite/ml. Les mêmes tests ont été effectués, mais en plaçant les échantillons dans du Styrofoam plutôt que l'agar, et les élévations maximales de température obtenues ont été de 2,1°C et 4,4°C pour les concentrations de 5 et 10 mg magnétite/ml, respectivement.

Un changement de volume remarquable de l'échantillon de NPM-PPNIPA ayant 10 mg de magnétite par ml a également été observé (Figure 6).

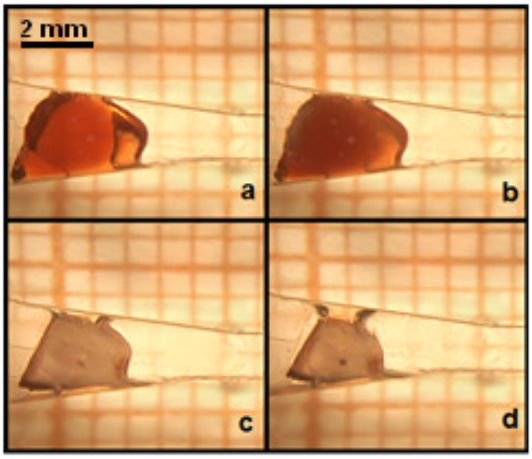

Figure 5. 60% changement de volume des hydrogels (a-d) @ 29°C

Par la suite, près de 100 sphères de NPM-PPNIPA (diamètre d'environ 1mm) ont été placées dans un champ magnétique alternatif de 4 kA m^{-1} à 160 kHz. Après 1500 secondes, une élévation de 2°C a été observée (Figure 6).

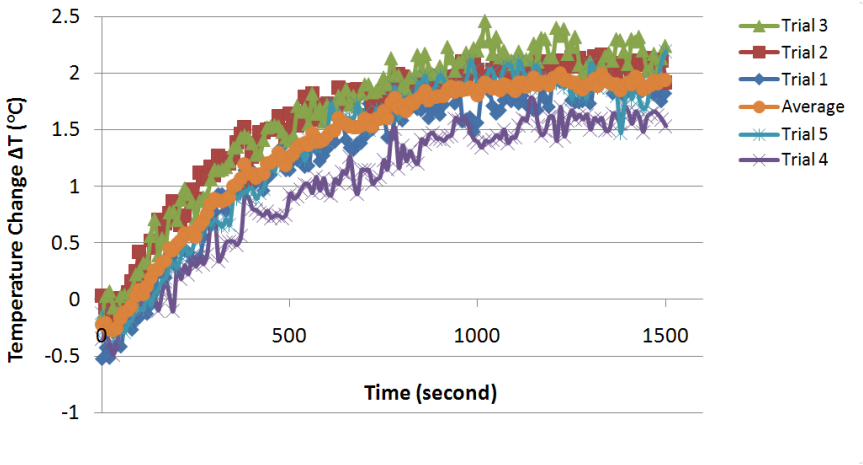

Figure 6. Élévation de température pour 100 NMP-PNIPA

Discussion et Conclusion

La motivation derrière le travail présenté dans ce mémoire était de réaliser un procédé d'activation pour un système robotique miniaturisé. De tels robots, aussi connus comme micro-carrier, se propulsent dans le réseau vasculaire d'un tissu cible comme une tumeur et l'augmentation de la température produite par hyperthermie actionne une séquence de libération du médicament. Dans la miniaturisation des robots navigables dans le corps humain, il est très important de réduire le nombre de composants. Cette réduction peut être obtenue en augmentant la fonctionnalité de chaque composant à son maximum. Un micro-carrier dans le corps humain a besoin de propulsion, de suivi et d'activation. Comme le montre la figure 7, les NPM peuvent contribuer à ces trois critères.

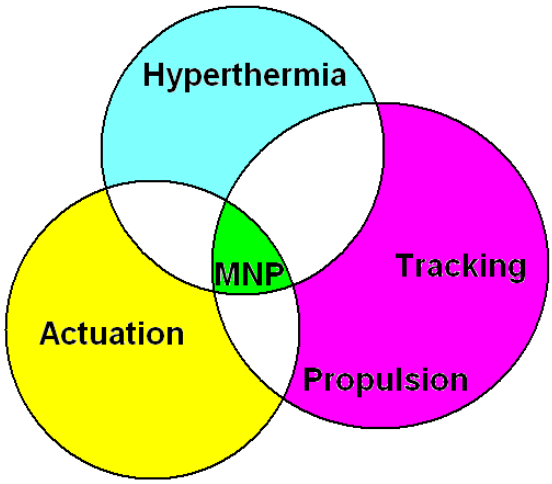

Figure 7. NPM comme actionneur hyperthermique navigables et détectables

Le SAR atteint une valeur maximale de 61,02 W g^{-1} pour les nanoparticules de magnétite de 20 nm enrobées avec du poly (acide maléique-co-oléfines) et soumises à des champs magnétiques alternatifs de 4,5 m KA-1 à 160 kHz. Ces nanoparticules peuvent être intégrées dans des micro-dispositifs de 50 µm de diamètre, contenant un médicament, et pouvant être immobilisés dans un volume cible de 30 mm de diamètre par embolisation. Pour propulser les transporteurs par le biais de capillaires utilisant les gradients de l'IRM, une agglomération des nanoparticules de magnétite occuperont environ 40% du volume du micro-carrier. L'eau, les chaînes de polymère

d'hydrogel et les agents thérapeutiques comptent pour les 60% restants de volume. La figure 8 montre cette situation hypothétique.

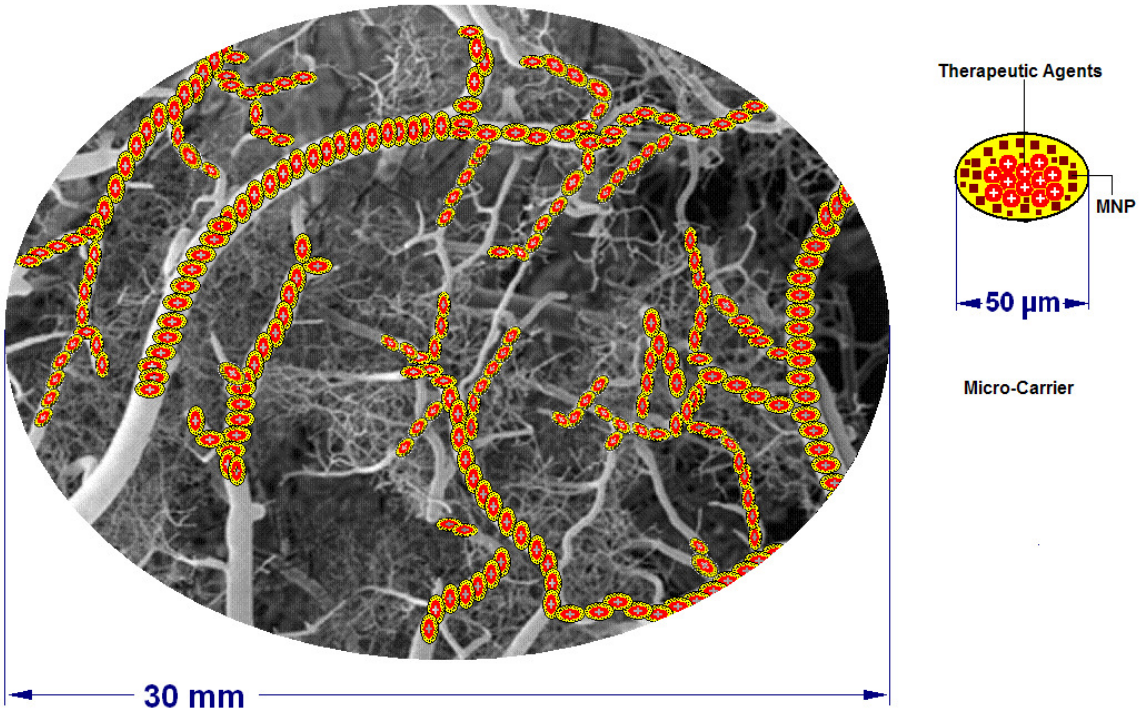

Figure 8. Embolisation de micro-carrier dans la zone cible

Une simulation par ordinateur prédit qu'après 700 secondes, la température au centre de la zone cible qui contient 110,000 micro-carriers serait élevée de 3 degrés. Une telle élévation est suffisante pour l'activation d'une séquence de libération d'agents thérapeutiques contenus dans les micro-carriers. 800 secondes après, l'élévation de la température serait d'environ 5 degrés, ce qui est suffisant pour l'hyperthermie modérée de la zone cible. Une présentation graphique de cette simulation est illustrée à la figure 9. Comme on le voit dans cette figure, l'élévation de la température décroît rapidement à mesure qu'on s'éloigne du centre de la zone ciblée. Cela signifie que pour une application d'hyperthermie, l'augmentation de la température peut être tenue loin des tissus sains avoisinants.

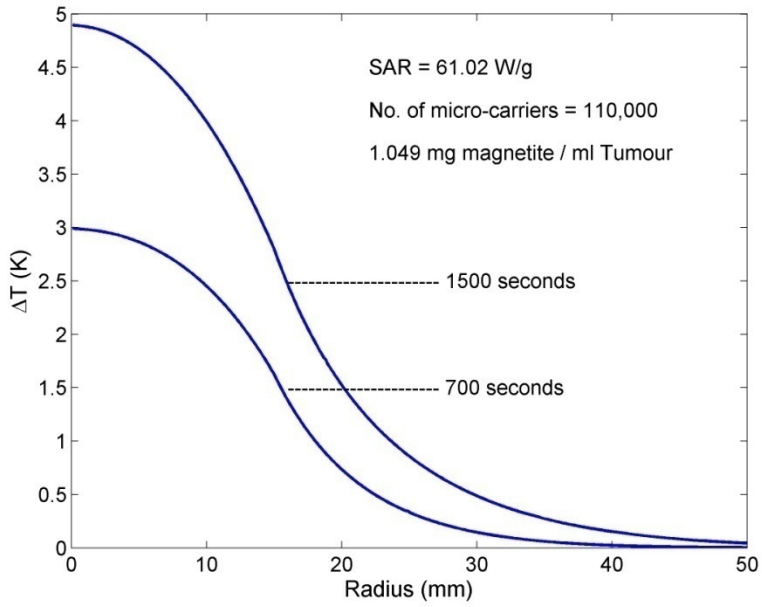

Figure 9. MATLAB® simulation, la température augmente en fonction du temps d'exposition aux champs magnétiques alternatifs pour une distance donnée.

Dans ce mémoire, l'hyperthermie via l'induction des NPM a été étudiée. Les effets de la concentration des NPM et de certains traitements de surface ont été évalués. Des NPM-PPNIPA sphériques ont aussi été chauffées avec l'induction d'un champ magnétique alternatif. En raison de la présence des NPM, l'hydrogel NPM-PPNIPA peut être propulsé par le gradient d'un champ magnétique tel que celui d'un système d'Imagerie par Résonance Magnétique (IRM). Une fois que ces hydrogels contenant des agents thérapeutiques atteignent leur cible, un champ magnétique alternatif respectant les limites physiologiques tolérables peut induire suffisamment de chaleur pour réduire leur volume et donc actionner une séquence locale de libération du médicament. Il s'agit d'un pas de plus vers la libération ciblée d'agents thérapeutiques actionnée par l'hyperthermie induite par des champs magnétiques alternatifs.

TABLE OF CONTENTS

LIST OF TABLES

LIST OF FIGURES

TABLE OF APPENDICES

LIST OF ACRONYMS AND ABREVIATIONS

AAS	Atomic Absorption Spectrometry
AC	Alternating Current
HIFU	High Intensity Focused Ultrasound
LCST	Lower Critical Solution Temperature
MNP	Magnetic Nanoparticles
MRI	Magnetic Resonance Imaging
PNIPA	N-isopropylacrylamide
PNIPA-MNP	PNIPA hydrogel encapsulated MNP
PMMA	Poly(methyl methacrylate)
SAR	Specific Absorption Rate
SLP	Specific Loss Power
TEM	Transmission Electron Microscopy
VSM	Vibrating Sample Magnetometer

INTRODUCTION

Elevation of body temperature, otherwise known as hyperthermia, has been used to treat cancerous cells for many decades. Hyperthermia can be achieved via various invasive and non-invasive methods, some of which are being practiced at clinical levels, and some others have already reached clinical trials. Magnetic nanoparticles (MNP) can generate heat and thus heat their surroundings once they are placed in an alternating magnetic field (AC magnetic field). In contrast to other hyperthermia methods, hyperthermia via MNP in an AC magnetic field provides advanced control and can be highly localized. In addition, MNP have enormous potential in biomedical applications such as imaging, medical diagnosis and treatment. Also, agglomeration of MNP can be propelled with the magnetic force from the gradient of a magnetic field towards a desired target location. The multi-functionality nature of MNP and their controllable physical parameters are the motives behind miniaturized robotic systems for tracking, propulsion and actuation of therapeutic agents inside human body.

This *evaluation* starts with a brief introduction to cancer and hyperthermia and follows by a short summary of key methods of hyperthermia as well as advantages of MNP and AC magnetic field. These advantages are not limited to tracking, propulsion and hyperthermia. For instance, the colloidal ability of MNP can alter the biological environment of the target tissue and initiate an immunological reaction. In later chapters, physical attributes of MNP, magnetic field and various heating mechanisms are introduced. Also biological and industrial limitations that lead to a set of magnetic parameters for MNP hyperthermia are explained. Thermo sensitive gels called hydrogels are introduced as potential carriers for the next generation of targeted drug delivery. These carriers are able to shrink and release their contained liquid with therapeutic agents upon elevation of temperature. Such elevation of temperature can be obtained from hyperthermia of the encapsulated MNP within the hydrogels by an AC magnetic field. The force that would propel these carriers in the vascular network to a target tissue is the gradient force of the magnetic field of a Magnetic Resonance Imaging (MRI) that applies on the agglomeration of MNP within the hydrogels. These MNP within the carriers can be seen as distortion of the images of the MRI and therefore can be tracked at the same time. Therefore, evaluation of hyperthermia to fit into realization of a systematic traceable and navigable hyperthermic drug release mechanism is a prerequisite.

CHAPTER 1 LITERATURE REVIEW

1.1 Cancer

Cells are the smallest living structural and functional units of the body. They have the ability to divide, synthesize protein, respond to extra cellular changes such as temperature and pH etc. Among all cell functionalities, DNA replication is one of the most important one. Errors in DNA replication are a major cause of damage to cells. In this sense, cells must produce exact copies of themselves in order to remain healthy. To do so, they must ensure that DNA replication is done correctly during each cell division cycle. One of many processes that ensure the divided cells are as healthy as the mother cell is called the *cell cycle checkpoint* process. It is a control system that checks the output of cell division step by step at several checkpoints. At any step, if the result is not satisfactory, the system prevents the parent cell from dividing any further. One of the important functions of the checkpoints is to check for any DNA damage. Once damage is found, the checkpoint uses another mechanism to pause any cell activity until the damage is repaired. In case the damage is un-repairable, the cell is sent to be destroyed or to *commit suicide* via apoptosis [1]. Despite the security checks, as a result of external factors such as tobacco, chemicals, radiation and infectious organisms as well as internal factors such as inherited mutations, hormones, immune conditions and mutations that occur from metabolism, damaged cells may still be produced [2] .While healthy cells duplicate exact copies of themselves, and stop reproducing when necessary, and stay together and self destruct when they are damaged beyond repair, unhealthy cells do not follow the same pattern. In some cases DNA error cannot be repaired or stays hidden and therefore the cell does not know when to stop reproducing or self-destruct. Sometimes these cells are produced far more than they can be terminated. These unhealthy cells could eventually lead to development of cancer cells. When cancer cells are produced unrestrained, a tumour is formed. Since these cells can travel in the body freely, they become more fatal once they rest in vulnerable organ such as soft heart tissue or bones. According to *American Cancer Society* there are more than 15 cancerous sites in the human body. These sites include oral cavity and pharynx, digestive system, respiratory system, bones and joints, soft tissue (including heart), skin, breast, genital system, urinary system, eye and orbit, brain and other nervous system, endocrine system, lymphoma, multiple myeloma and leukemia. Statistics from the *Canadian Cancer Society* suggests an estimated 171,000 new cases of cancer

in 2009 from which 75,300 patients will lose their lives. *American Cancer Society* predicts even more devastating numbers: in the year 2009 cancer is expected to take 562,340 American lives, more than 1500 Americans per day [3]. As cancer remains one of the leading death causes in North America, researchers around the world try to find more suitable treatments to battle this deadly disease.

1.2 Hyperthermia

Since the late 1960s, the concept of hyperthermia has drawn a lot of attention to the field of medicine. Hyperthermia is defined as an abnormal elevation of temperature. Unlike fever, which is regulated by the body's temperature set-point, hyperthermia can be created artificially by means of drugs or medical devices. Because of its cytotoxicity effect, it is sometimes used as a rehabilitation method and therefore named thermal (heat) therapy or thermotherapy. Hyperthermia can reduce arthritis pain, relieve muscle spasms, reduce inflammation, and increase blood flow to provide nutritious needs to injured tissue [4]. It is well-known that sustained elevation of temperature due to hyperthermia above 42°C – 43°C causes necrosis of living cells [5]. Clinical trials since the 1970s have led to the hypothesis that "the cytotoxicity effect of hyperthermia is mainly based on denaturation of cytoplasmic and membrane proteins". Cellular death rate due to heat exposure varies depending on the sustained temperature and the duration of hyperthermia. This rate is also dependent on the phase of the cell cycle, i.e. Mitosis, G1, DNA synthesis (S-phase), and G2 which explains the different mechanisms of cell deaths [6].

In oncology, hyperthermia refers to the heating of organs or tissues in various ways, to temperatures between 40°C and 45°C, at which point it causes moderate and reversible cellular inactivation. This heat can lead to preferential death of malignant cells by enhancing cell sensitivity and vulnerability towards more established forms of cancer therapy such as radiation [7, 8] and chemotherapy (thermal chemosensitization, thermal radiosensitization) [6, 9]. Hyperthermia leads to a synergistic effect in anti-cancer techniques such as chemotherapy. More specifically, hyperthermia can be seen as a complementary therapy that yields maximum benefit from chemotherapeutic agents such as alkylating agents, platinum compounds or threshold behaviour (anti-neoplastic) agents such as doxorubicin, and independent or additive agents such as fluorouracil, taxanes, and vinca alkaloids, while minimizing their applied dosage to the physiological system and thus reducing their toxic side effects that harm healthy cells [10].

Hyperthermia, as used in cancer treatment, is meant to target unhealthy cells and keep the healthy cells unharmed. Healthy cells have organized and systematic blood flow in their surrounding vascular network, and via such they can easily cool down and dissipate excessive heat by means of conduction and convection. Cancer cells on the other hand have often far less developed vascular network and therefore overheat [11]. Studies show that at temperatures *above* 42°C tumour blood flow decreases [6]. Here, changes such as viscosity of blood cell membrane lead to hypoxia, acidosis, and cell energy deprivation. Available data suggests that moderate hyperthermia *below* 42°C increases tumour blood flow which leads to higher supply of oxygen and nutritious supplements to the tumour. The resultant increase in blood flow assists in efficient delivery of drugs and chemotherapeutic agents to the tumour, and increased oxygen supply favours radiotherapy effects.

Hyperthermia also has other advantages that lead to cancerous cell death. Due to the elevation of cell temperatures during hyperthermia, cells undergo a series of morphological changes to their membranes, cytoskeletons, cellular proteins and nucleic acids [6]. Also, pre-clinical studies suggest that, similar to fever, hyperthermia is associated with immunological reactions and can stimulate and activate host immune systems against malignant cells [12]. Hyperthermia also seems to overcome drug resistance above moderate temperatures. The cytotoxicity of certain anti-neoplastic drugs such as doxorubicin is reported to be substantially enhanced above specific temperatures [13].

Among different applications of hyperthermia, ‘actuation’ is of high interest. Here, localized hyperthermia is used to trigger a drug release mechanism. For instance, therapeutic agents encapsulated in special thermo-sensitive hydrophilic polymers such as PNIPA [11, 14] are able to reduce in volume up to thousands of times when heated [15], therefore releasing the drugs contained within. This is discussed in more detail in the following chapters.

1.2.1 Methods of Hyperthermia

There is a wide spectrum of hyperthermia methods but it can be generally classified into three groups: whole body hyperthermia, hyperthermia by wireless applicators, and hyperthermia by insertion of heating source(s). Here, each approach is briefly discussed.

I. Whole body hyperthermia – This complementary technique to cytotoxic drugs and/or radiotherapy is one of the oldest among all other types of hyperthermia. In this method, the entire body is heated either by preventing body heat transfer to the surrounding medium, or placing the patient inside a bath of heated water operated by specialist in a controlled environment. As seen in Figure 1.1, the head of the patient is usually placed outside of the heating chamber to avoid further complications, and the rest of the body is heated inside the chamber. Whole body hyperthermia is commercially available, and due to its simplicity is usually recommended for patients at high risk of relapse after surgical removal of a tumour [16].

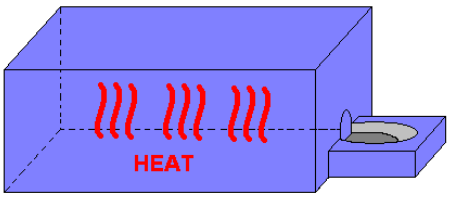

Figure 1.1. Whole body hyperthermia

Whole body hyperthermia lacks homogeneity of heat distribution in the tissue and may cause superficial overheating, thermal lesions, and discomfort caused by surface burning. Recently, a computerized perfusion method was suggested to solve this issue [17]. Nevertheless, sustained elevated body temperature may have a negative impact on healthy organs, such as the heart, which can result in cardiac disorders, and may cause changes in thrombocytopenia and the intravascular coagulation system. Other side effects may be a decrease in volume of blood plasma (hypovolaemia) and capillary leak syndrome [10].Therefore, pursuit of a localized hyperthermia method is still of high interest.

II. Wireless applicators (noninvasive): These methods can be considered regional or local hyperthermia methods. They consist of sending waves to the target area where, depending on the physical properties of the tissue and the applicator(s), the energy of the wave is transformed into heat. Such applicators are the subject of many clinical studies and are commercially available. Below, three major wireless applicators are mentioned.

a. High Intensity Focused Ultrasound (HIFU)

Ultrasound is a sound pressure wave that has frequencies higher than what humans are able to hear. It is used for imaging of soft tissue by penetrating ultrasonic waves inside the tissue and measuring the reflected signature. Ultrasound is a fairly simple, safe, highly controllable, cost effective and widely available technology. Once ultrasonic waves are focused and transmitted to the soft tissue, molecular friction causes mechanical heat. High Intensity Focused Ultrasound (HIFU) can further heat the tissue leading to thermo-ablation. In thermo-ablation the target temperature is high enough to burn and instantly destroy cells. Figure 1.2 illustrates a schematic and Magnetic Resonance Imaging (MRI) image of a uterine fibroid being treated by emitting ultrasound waves through a transducer. As seen in this figure, the waves are focused by a lens and beamed directly on the target tissue.

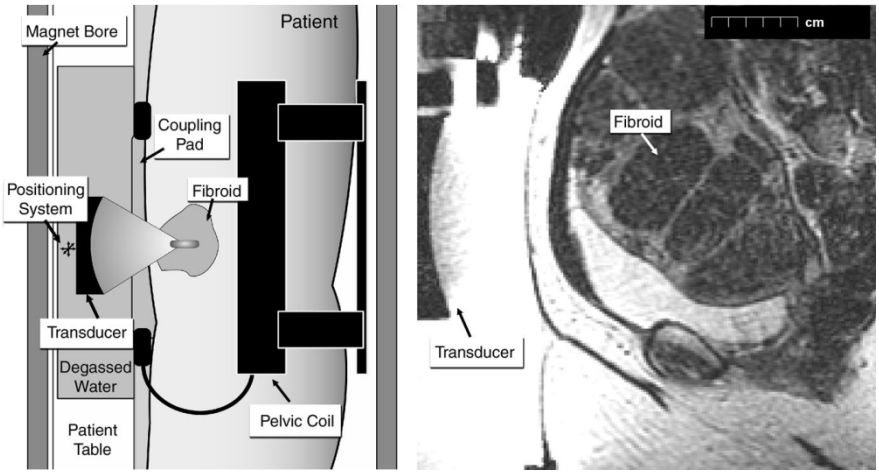

Figure 1.2. High Intensity Focused Ultrasound [18]

Despite impressive and promising results from recent clinical studies by InSightec© [19] HIFU may not be ideal for areas near bones or gas. Sound waves travel at different speeds depending on the reflection index of the medium. Sound waves are partially reflected rather than transmitted at the interface of air and tissue or tissue and bone, due to sudden change of reflection indices. At such interfaces the wave energy is absorbed elsewhere causing hot spots. Therefore HIFU would not be best for lungs and near bones. Also due to occasional non-uniform heat distribution, hot spots are common results of the treatment which cause discomfort for the patient [20].

b. Electromagnetic applicators (non-invasive):

1. Radiofrequency (RF) – This widely and commercially available thermotherapy technique is based on current that is induced by RF waves (0.5 – 300 MHz) in a biological tissue to oscillate free electrons and ions. Heat generation is due to collision of such electrons and ions with immobilized atoms. Elevation of temperature depends on the position and the geometry of the RF antenna as well as its frequency and power. There are two approaches for RF antennas: capacitive plates and inductive coils [21].

- Capacitive antenna: the region of interest of the body is placed between two charged plates. Electric field induced between these plates generates heat in the tissue regardless of target depth. However fat around the target tissue may cause excessive superficial heating. When the target area is deeper in the body, homogeneity and uniformity of heat distribution decreases rapidly. Figure 1.3 shows this type of RF applicator.

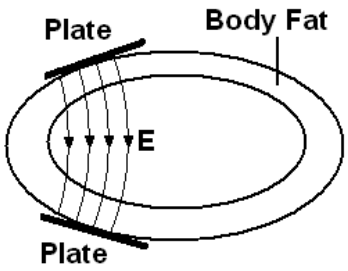

Figure 1.3. Capacitive Applicator

- Inductive antenna: this type of regional thermotherapy consists of an induction coil that creates eddy current in the tissue causing it to heat. This heat is related to electrical conductivity of the tissue. Thus variation in tissue conductivity may cause non-uniform temperature distribution, as some parts of the tissue may heat up more than others.

To solve inhomogeneous temperature distribution issues related to RF, researchers have introduced multiple and resonant cavity antennas [22, 23]. However more work is needed both theoretically and experimentally to overcome these issues.

2. Microwave – In the electromagnetic spectrum, microwaves are waves having frequencies between 300 MHz and 30 GHz (infrared frequencies). In a process called dielectric heating, water molecules within the biological entity absorb microwave energy. Since these molecules contain positive and negative charges – water molecules are bipolar – they try to align themselves with the electromagnetic field of the microwave. Due to high frequency, this leads to fast molecular motion and causes local elevation of target temperature. Microwave has a better convection profile than RF and therefore more efficient temperature distribution [24]. It is evident that apart from heat, the electrical field of the microwave leads to changes in secondary and tertiary structure of microorganisms which contributes further in cell death [25]. Clinical trials for noninvasive localized hyperthermia are considered with microwaves at 433 MHz [26], 915 MHz, and 2450 MHz [27]. Normally, microwave induced hyperthermia is best for superficial tumours because microwave cannot penetrate to target tissues deeper than few centimetres under the skin [28]. This is due to the high absorptive nature of water and its dense availability in human tissue. This is a disadvantage because it may cause uneven heat distribution and power absorption in and around deep seated target tissues. Researchers have partially addressed this issue by proposing the use of in phase multiple array antennas which allow for deeper penetration [29]. In this case, target volume, desired temperature and target depth determine the number of antennas, frequencies and power. To name a few approaches, researchers have used rotating spiral and multi loop antennas in many pre-clinical studies but these techniques still lack temperature homogeneity at deep seated target tissue [26, 30].

III. Insertion of heating source(s) (invasive): In this type of thermotherapy heating sources are surgically placed inside or around target area. This method was first presented in 1975 as ‘invasive interstitial technique for delivery of hyperthermia’ [31]. Due to the invasive nature of this technique, it can cause discomfort and complications prior to, during and after each

treatment. Also, slight movement of the implants as a result of any movement of the patient may affect the treatment measurements. This method can be performed via one of the following techniques:

a. Microwave heating: Electromagnetic waves from inserted microwave antennas or coaxial waveguides agitate polar molecules of water and cause them to heat [24]. This method was developed to minimize heterogeneity of microwave heat distribution in the tissue while further localizing microwave thermal therapy.

b. Radiofrequency heating: Insertion of a pair or an array of macroscopic RF electrodes inside the tissue to convert electromagnetic energy from RF waves to heat [21]. A down side to this is that after some time current that runs through these electrodes causes a charring effect. This effect leads to the formation of an insulator around the electrode that will interfere with desired wave emission [32]. Also there have been reports of local burning around the electrode due to excessive evaporation of water at this zone [24].

c. Ferromagnetic seeds: In this method implanted ferromagnetic seeds as large as a few centimetres – also known as thermoseeds – are placed inside an oscillating magnetic induction field. Thermoseeds absorb the field energy and induce eddy currents. Heat is then generated by the eddy current losses leading to interstitial hyperthermia. This heat is then transferred to the surrounding tissue by thermal conduction without the need for electrical connection between implanted seeds and a power source [33].

IV. Nanoparticles: Generation of heat from these particles, unlike thermoseeds, is not limited to eddy currents. Heat may also be generated due to hysteresis loss, relaxation losses, or other types of losses due to infrared or microwave energy absorption. In this method, nanoparticles have to be injected in the tissue at which thermal therapy is desired. That is why some may classify it as an invasive hyperthermia technique. In the following section, this approach is discussed in more detail.

1.3 Advantages of Nanoparticles

Various methods to synthesize nanoparticles provide scientists the ability to selectively control the core size of nanoparticles [34]. This ability allows researchers to use nanoparticles to target a wide range of biological entities, such as cells (10-100 μm), viruses (20-450 nm), proteins (5-50 nm) and genes (2 nm wide, 10-100 nm long) [35]. In addition, targeting biological entities has been achieved using the colloidal ability of nanoparticles and dispersion by means of specific antibody coatings, such as dextran, polyvinyl alcohol and phospholipids [35]. Such coatings also serve as a protective shell to minimize direct exposure of the nanoparticle core to the biological environment. For cancerous cells, once the nanoparticles are located within the cell via intracellular, interstitial or membrane bonding, experiments show that even after mitosis, 50% of the particles remain within the tumour cells [36]. This is advantageous, should repeated hyperthermia treatment become necessary. Other studies show that cells react to the topography cues of their environment and neighbouring cells. Nanoparticles attached to the cancer cells influence the shape of the cell cytoskeleton formation. These cells present nano-bumps and nano-spheres to the neighbouring cells encouraging them to switch from growth to apoptosis – cell's self destruction mechanism [37].

Magnetic nanoparticles (MNP) can be excited once placed in an alternating magnetic field (AC magnetic field), regardless of their depth inside biological tissue. On the contrary, other techniques such as RF, Microwave and HIFU, are not able to accurately target cancerous tissue. This is due to increasingly complex parameters as penetration depth increases [38]. On the other hand, homogenous cell temperature increase may be achieved without the formation of 'hot spots' if sufficient concentration of MNP with proper coatings and colloidal ability are used [36]. MNP experience a thrust force when exposed to a magnetic gradient field, therefore an agglomerated ensemble of MNP can be propelled through the circulatory system to a desired target area. Such gradient force can be obtained from a clinical MRI [39] where functionalized MNP are seen in real-time as distortions of the magnetic field during imaging sequence. MNP can be used as MRI contrast agents, a property that allows for confirmation of their distribution to the target area prior to any treatment [38].

A systematic hyperthermic drug release actuation can be obtained by encapsulating MNP in thermo-sensitive hydrogels along with therapeutic agents. Biocompatible temperature sensitive

gels are able to shrink up to thousand times in response to small temperature increase [11]. While acting like a sponge, these hydrogels may assist release of therapeutic agents embedded within the gel at an adjustable desired temperature. In a therapeutic setting, MNP can be used to heat the hydrogel once it is propelled to the desired location thereby releasing therapeutic agents at the target site only.

Last but not least, MNP can be engineered to have relatively low Curie temperature points which leads to self regulation and thus avoids overheating the tissue when excited by an AC magnetic field [40]. For instance, Ag-doped manganite nanoparticles have shown great self regulating properties and have a curie temperature range of 41 – 44ºC [41]. In this sense, use of invasive temperature measurements such as fibre optics probes becomes unnecessary and instead non-invasive methods such as MRI temperature mapping become more practical [42].

CHAPTER 2 THEORETICAL BACKGROUND

The two components to the electromagnetic field, which are electric field and variation of the magnetic field, are liable for generation of heat in a tissue. The thermal effects are determined by the dielectric properties of the tissue and the magnetic properties of the medium, respectively. As discussed in Section 2.3.2, low frequencies (~100 kHz) are best for deep tissue penetration. Since biological materials do not have significant magnetic properties, biocompatible MNP are used to increase the influence of the variation of the magnetic field. In this project, the emphasis is placed on the magnetic component of a low frequency electromagnetic field. The current chapter is allocated to literature reviews and describes the background physics as well as definition of basic concepts for this project.

2.1 Nanoparticles in Hyperthermia

The history of nanoparticles goes as far back as 9th century where ancient Muslim craftsmen used the glittering effect of nanoparticles in their products [43]. Today, modern science considers nanoparticles a link connecting bulk matter with its atomic or molecular structure. This property has led to interest in nanoparticles in such diverse fields as engineering, physics, chemistry and biology. In medicine, nanoparticles can be thought of as key elements of a new generation of medical diagnosis and treatment tools. For instance, fluorescent semiconductor nanoparticles, otherwise known as quantum dots, are used for imaging of biological entities [44]. Superparamagnetic nanoparticles are also commercially available as contrast agents for magnetic resonance imaging (MRI) to help diagnose various diseases [45].

In oncology, nanoparticles have successfully been used as anti-cancer drug and gene carriers to prevent and control cancer, as well as a detection tools for imaging in cancer diagnosis [46, 47]. Their multifunctional characteristic is what makes them great candidates for targeted drug delivery and cancer treatment. In the past decade, there has been significant interest in the use of nanoparticles for hyperthermia. For localized hyperthermia, nanoparticles such as ‘photo thermal gold nanorods’ were used to absorb near infrared irradiation energy and elevate local tissue temperature [48]. Gold nanoparticles are biocompatible and have flexible surface composition as well as unique optical properties that allow them to be highly absorbent of optical energies [49]. Another method called laser-induced thermal therapy employs silica core dielectric nanoparticles

coated with ultrathin gold metallic layer, also known as nanoshells, to absorb near infrared energy and convert this energy to heat [50]. Electromagnetic fields within the frequency range of tens of megahertz have also been used to generate heat using iron doped gold nanoparticles [49]. Other types of nanoparticles such as $La_{0.7}Sr_{0.3}MnO_3$ have also been used to generate heat once exposed to a microwave applicator [51].

MNP from metals such as iron, cobalt and nickel and their alloys are useful due to their magnetically induced and multifunctional properties. These nanoparticles are able to create heat once placed in an external AC magnetic field. Among different chemical compositions of MNP, iron oxide has been given special attention for hyperthermia. That is due to its proven biocompatibility, biodegradability and low toxicity [52]. Iron oxide particles for magnetic hyperthermia were first suggested in 1957 [53]. Since then other MNP compounds such as iron cobalt with particularly higher magnetization than iron oxide have been suggested [54]. Iron cobalt has shown higher induction efficiency than iron oxide, however due to unknown toxicity issues of this magnetic compound further investigation is required before it can reach human clinical trials. Various compositions such as Cu-Ni, Gd-substituted Mn-Zn ferrite, $CoFe_2O_4$, and Mn-Zn ferrite have also been used for the purpose of hyperthermia [55-58].

2.2 Heat Generation of MNP Inside an AC magnetic field

The heat generated by the MNP inside of an alternating magnetic field (AC magnetic field) is mainly caused by three major mechanisms; hysteresis loss, Néel and Brownian relaxations. Particle size, shape, composition, concentration and viscosity of the suspension medium as well as magnitude and frequency of the applied magnetic field determine the relative strength of each of these mechanisms.

2.2.1 Magnetic Domains

Large magnetic materials consist of several domains in order to minimize magnetostatic energy of the material. The magnetostatic energy is the energy of the magnet in its own field. In the System of International (SI) Units, magnetostatic energy is given by $\left(\frac{1}{2}\right)\int \mathbf{H}^2\, dv$ where dv is an element of the volume, H is the magnetic field and the integration is evaluated over all space [59]. As shown in Figure 2.1 [59], by splitting the crystal into several domains, the spatial extent

of the *H* field decreases. This is because as the number of domains increase, the north and the south poles become closer and therefore it reduces magnetostatic energy of the material.

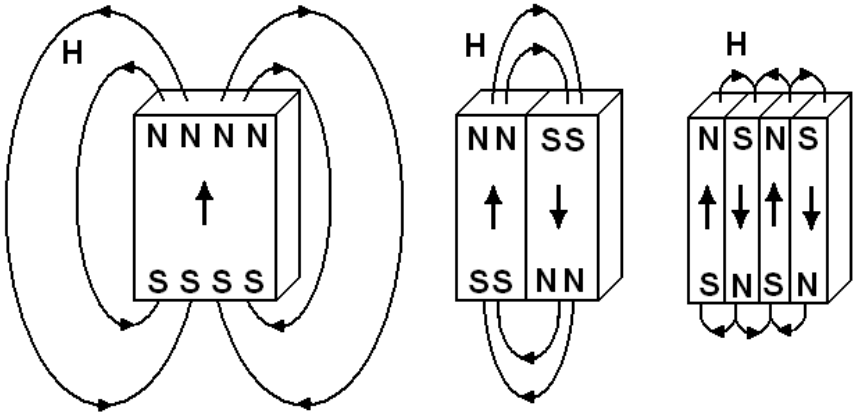

Figure 2.1. Magnetostatic energy reduces as crystal is split into domains

The boundary separating the two neighbouring domains is called a domain wall. Each domain contains large numbers of atomic magnetic moments, *m* created by microscopic current related to the spin of the electrons. Indeed, all materials are classified by the orientation of their magnetic moments and form various types of magnetism mainly known as ferromagnetism, ferrimagnetism, antiferromagnetism, paramagnetism and diamagnetism. The complete theory of magnetism is well beyond the scope of this introduction. However, Figure 2.2 [60] illustrates the orientation of the magnetic moments for these types of magnetism.

Magnetic moments of ferri-, ferro- and antiferromagnetic materials are aligned with each other below a critical temperature – the Curie temperature – to reduce the exchange energy of the material. The exchange energy is caused by the interactions among internal magnetic moments. According to the Weiss domain theory [61], the direction of the aligned moments varies from domain to domain, and in the absence of an external magnetic field this direction is aligned along magnetic crystallographic axes called ‘easy axes’. In fact, domain walls consist of smooth gradual rotation of the direction of the *m* vectors within the crystal shown in Figure 2.3 [60].

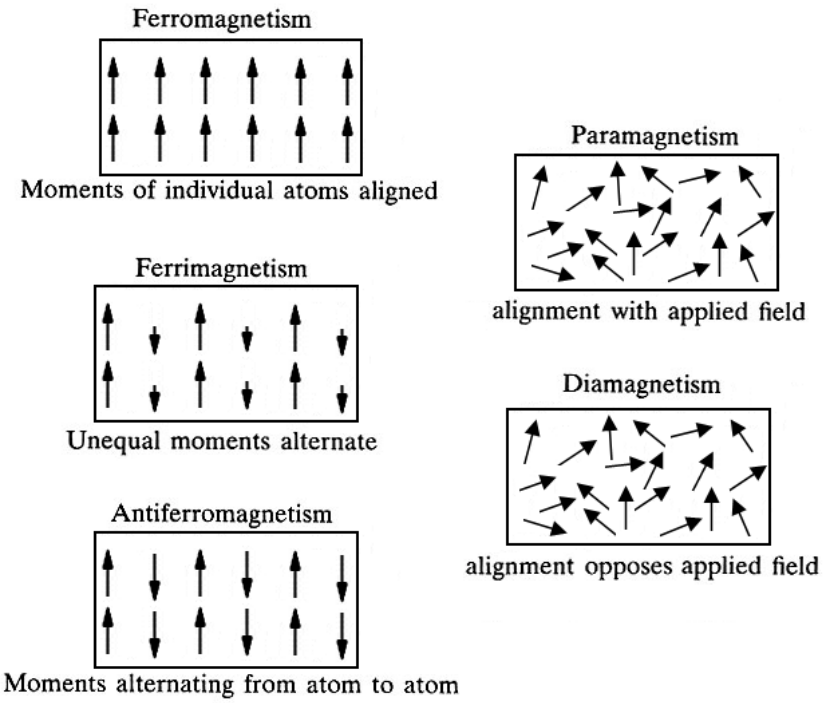

Figure 2.2. Different types of magnetism

The spin-orbit coupling, meaning interaction between spin and the orbital motion of each electron, exhibits a resistive force against any attempt by an external magnetic field to rotate the spin axis. The energy required to overcome the spin-orbit coupling that keeps particles magnetized in a specific direction is called anisotropy energy, $E = KV$, where K is the effective anisotropy constant and V is the volume of the magnetic core [59, 62]. The anisotropy constant is a sum of several terms such as magnetocrystalline, shape and surface anisotropy as well as dipole-dipole interaction between the crystals [63]. Here, it is assumed that the MNP have spherical shapes and are mono-dispersed in solvent with low volume fractions. Therefore magnetocrystalline and surface anisotropy contribute the most to the effective anisotropy constant of MNP.

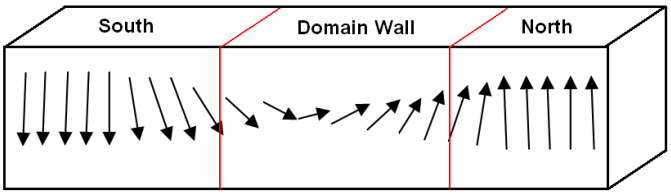

Figure 2.3. Presentation of domain wall

As the external magnetic field strength increases, the net *m* vectors of the domains of a ferri- and ferromagnetic material become more aligned with the external magnetic field direction to minimize the crystal potential energy and cause displacement of the domain walls. Figure 2.4 [59] shows that as the external field strength becomes larger, the magnetic moments opposing it become smaller. If the external field is high enough, it can align all *m* vectors to the magnetic field direction and the material can act as a single domain particle with a unidirectional magnetic moments.

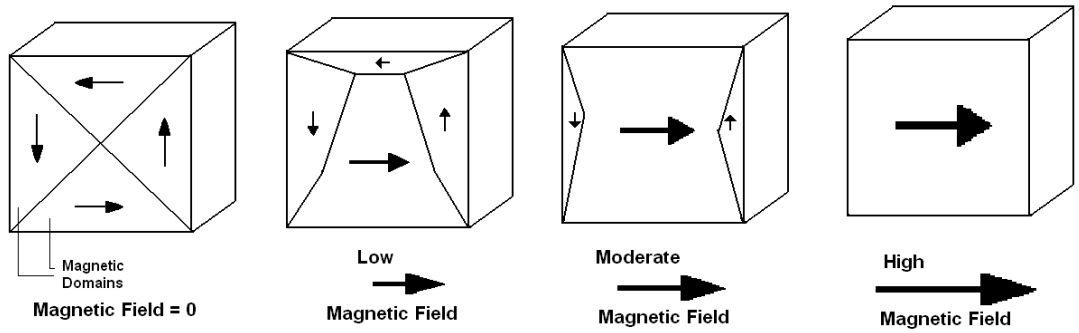

Figure 2.4. Multi-domain material inside applied external magnetic field

In this investigation, ferrimagnetic iron oxide (magnetite) nanoparticles were chosen. As shown in Figure 2.2, these nanoparticles display lower magnetic response compare to ferromagnetic materials. This is because a ferrimagnetic material consist of *m* vectors that are not all aligned in one direction, therefore the net *m* vector is smaller than that of a ferromagnetic material where the *m* vectors are all aligned in one direction. However, in addition to magnetite biocompatibility and low toxicity advantages, these particles are less sensitive to oxidation than ferromagnetic materials and therefore maintain stable magnetic behaviour [60] in rich oxygen environments such as in a human body.

2.2.2 Hysteresis

The energy from exposure to moderate external field **H** (Figure 2.5 point 1) [60] leads magnetic moments to overcome the anisotropy energy. This results in an irreversible sudden rotation of the magnetic moments into a new set of magnetic crystallographic axes. These axes are nearest to the external field direction. The directions of the moments within domain walls are indeed a balance between exchange and anisotropy energies. Therefore a change in the external field energy can

alter this balance and cause moments to rotate. Further increase in field amplitude leads to saturation of magnetization M_S of the magnetic moments (Figure 2.5 point 2) and a reversible and gradual alignment with the external field direction and hence creation of a sample that acts as a single domain [61]. The M_S value for a bulk matter is different for nanoparticles of the same material. For example, experimental values for M_S of magnetite nanoparticles are between 30 – 60 emu g^{-1}, whereas this value for the bulk magnetite is reported to be as high as 92 emu g^{-1} [60]. The reason for such difference is not entirely clear and still under investigation. By reducing the applied magnetic field to zero, magnetization **M** of the domains decreases gradually to remanent magnetization – M_R (Figure 2.5 point 3). The magnetization can be reduced to zero by applying a magnetic field in the opposite direction and a magnitude equal to the coercive field H_C (Figure 2.5 point 4). At this point domains are demagnetized completely, but they can gradually begin to realign in the opposite direction if the external field is increased in the negative direction and reaches M_S (Figure 2.5 point 5). Once again, by reducing the external field to strength zero, magnetic moments reach M_R in the negative **M** axis (Figure 2.5 point 6). An applied magnetic field magnitude equal to coercive field H_C in the positive direction will bring magnetization to zero and further increase of the field amplitude in this direction will trace the curve back to positive M_S (Figure 2.5 point 2). As shown in Figure 2.5, the magnetization curves for increasing and decreasing magnetic field amplitudes do not coincide and therefore the material demonstrates "hysteresis behaviour" – hysteresis is a Greek word for 'a coming late' – and hysteresis losses are expressed in the form of heat dissipated to the surrounding medium.

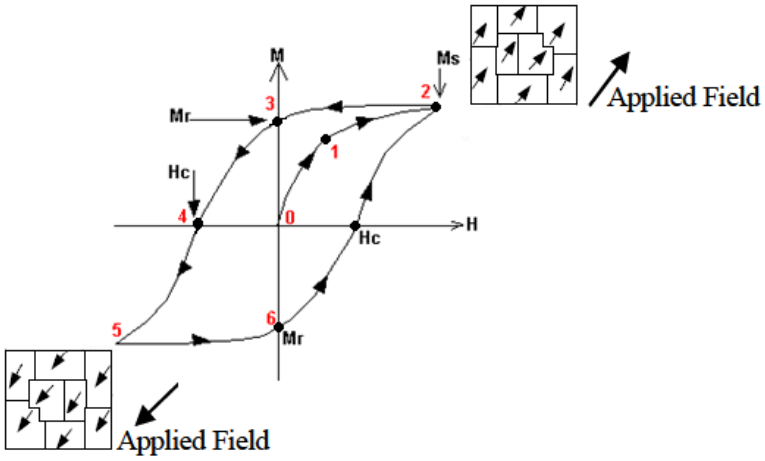

Figure 2.5. Hysteresis curve of a multi-domain particle

In the case of fine ferri- and ferromagnetic single domain particles, such as iron oxide and cobalt respectively, thermal agitations are ignored when the difference between the maximum and the minimum energy per unit volume, set by the anisotropy energy of the particle, is larger than its thermal energy kT, where k is Boltzmann constant. Stoner-Wohlfarth's calculations [64] demonstrate a narrow hysteresis curve for these single domain magnetic particles. When an external magnetic field is applied to magnetize and demagnetize such particles, energy is released in the form of heat. As in multi-domain particles, when the external magnetic field amplitude is larger than the anisotropy field, the anisotropy energy barrier is overcome and the magnetic moments will rotate onto the anisotropy axis closest to the external magnetic field direction. Further increase in the external field will lead to gradual alignment of the net magnetic moment with the external magnetic field direction until saturation. Figure 2.6A demonstrates this phenomenon. In this Figure, dashed lines represent the magnetic moments of the particle and solid lines represent the dominant 'easy axes'. When external field **H** is applied, the magnetic moment follows the field direction. Once the external magnetic field is removed, the magnetic moment takes a certain time to rotate back to its original lower energy 'easy axis. Release of heat is therefore due to the fact that magnetisation here lags the applied external field.

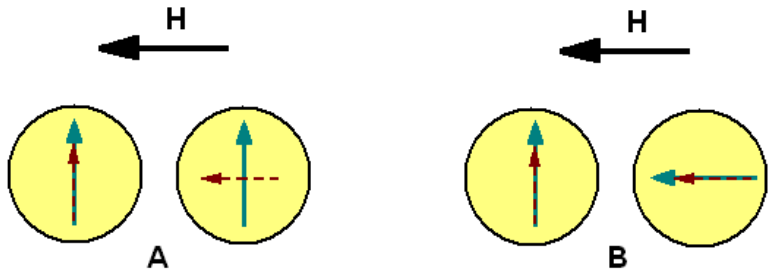

Figure 2.6. Relaxation Mechanisms

Dashed lines represent the magnetic moments of the particle and solid lines represent the dominant 'easy axes'

2.2.3 Superparamagnetic Nanoparticles

In smaller single domain magnetic particles, called superparamagnetic nanoparticles – less than 20 nm in diameter for Iron Oxide Fe_3O_4 (Magnetite) MNP [65] – the difference between the magnetic moment maximum and minimum potential energy per unit volume of the particle is much smaller than its thermal energy kT. The orientation of the magnetic moments of these

particles therefore, continuously changes due to thermal agitation [66]. In other words, thermal energy becomes significant enough to cause magnetic moments to randomly fluctuate in the absence of the energy from an external magnetic field. Due to this behaviour, as shown in Figure 2.7 measured for iron oxide nanoparticles, these particles seem to lack hysteresis losses. However coercive fields H_C do not rest at zero. Therefore an extremely narrow hysteresis loss is formed which contributes into release of heat within superparamagnetic nanoparticles.

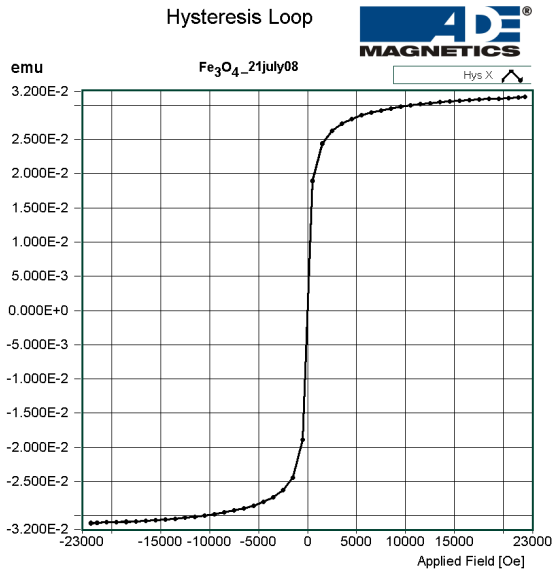

Figure 2.7. Hysteresis curve of a iron oxide superparamagnetic particle

2.2.4 Relaxation Mechanisms

By applying a moderate external magnetic field to superparamagnetic nanoparticles, the energy from the field drives the magnetic moments to rotate and aligns them with the magnetic field direction by overcoming the thermal energy barrier. Once the external magnetic field is removed, magnetic moments do not relax immediately but rather take some time to randomize their orientations. In fact, according to Néel relaxation mechanism, in superparamagnetic particles the alignments and relaxations are responsible for the generation of heat. According to Néel-Arrhenius equation [67], the time τ_N for the magnetic moments to relax and rotate back to their thermal equilibrium orientation is given by

$$\tau_N = \tau_0 \exp\left(\frac{KV}{kT}\right) \tag{2.1}$$

where K is the effective anisotropy constant, V is the volume of the magnetic core, kT is the thermal energy and τ_0 is a constant called 'attempt time' typically of a value equal to about 10^{-9} to 10^{-11} seconds and is slightly field dependent, however this dependency is usually ignored [68].

The third mechanism that may contribute to generation of heat within MNP is Brownian relaxation. This type of relaxation mechanism causes both multi-domain and single domain particles to heat up. In this case, shown in Figure 2.6B, the energy barrier for reorientation of a particle is given by rotational friction due to the rotation of the entire magnetic particle caused by the external magnetic field torque on the magnetic moment of the particle. Here, by applying the external magnetic field **H** the particle itself is able to turn towards the field direction. Brownian relaxation time τ_B, is defined by the rotational mobility of the colloidal magnetic particles and given by [69]

$$\tau_B = \frac{3\eta V_H}{kT} \tag{2.2}$$

where η is the dynamic viscosity of the medium in which the particles are suspended and V_{H} is the hydrodynamic particle volume. This volume, which is the volume of the magnetic core of the particle plus the coating shell around it, represents how the medium perceives the particle. The Brownian relaxation time is related to the applied magnetic field through the complex magnetic susceptibility. The relationship between magnetization **M** and the applied magnetic field ***H*** is expressed below by a parameter called magnetic susceptibility χ

$$\mathbf{M} = \chi\,\mathbf{H} \tag{2.3}$$

This parameter explains how magnetization varies with respect to the applied magnetic field. As described later, susceptibility consists of a complex (imaginary) and a real component. The Brownian relaxation time is accessible from the frequency (f) dependent complex susceptibility through the following equation [69]:

$$\chi(f) = \frac{\chi_0}{1 - i\,2\pi\,f\,\tau_B} \tag{2.4}$$

where χ_0 is the DC susceptibility.

For MNP uniformly suspended in a liquid medium, relaxation times Néel τ_N and Brownian τ_B take place in parallel [70]. Therefore the effective relaxation time τ_{eff} or τ is given by

$$\frac{1}{\tau_{\text{eff}}} = \frac{1}{\tau_{\text{N}}} + \frac{1}{\tau_{\text{B}}} \tag{2.5}$$

By simulating and plotting relaxation times versus particle size in Figure 2.8, (parameters are given in Appendix A.1) for any given radius, it is clear that the shorter time constant dominates the effective relaxation time. It is worth mentioning that in highly viscous media, such as thick gel or tissue, the inverse of Brownian relaxation becomes very small and therefore the effective time becomes dependent on Néel relaxation exclusively. This is further discussed in Section 2.4.

Relaxation times are temperature dependent. However for mild hyperthermia at near 42ºC, relaxation time constants does not alter by much, thus in this investigation the effect of small temperature elevations on time constants are considered negligible.

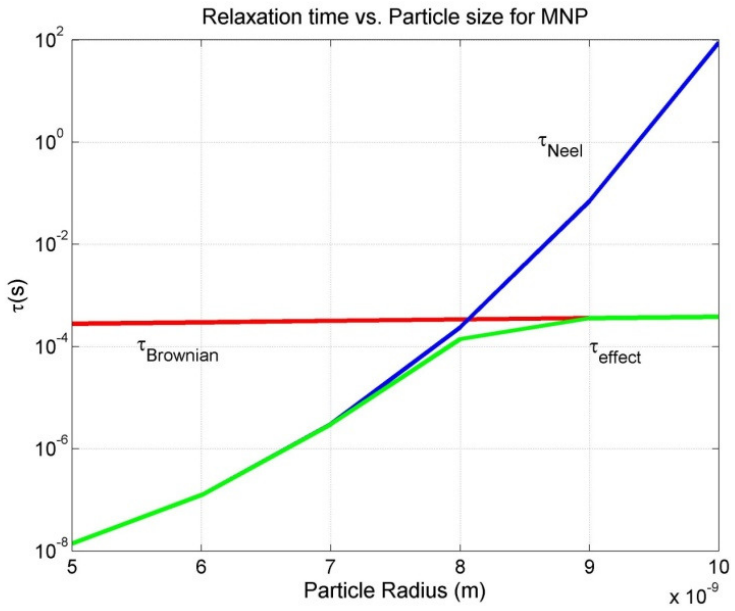

Figure 2.8. Relaxation time vs. Particle size for MNP

2.2.5 Specific Absorption Rate (SAR) and Specific Loss Power (SLP)

In hyperthermia, Specific Absorption Rate (SAR) is a measurement of the magnetic power absorbed per unit mass of the magnetic material (W g^{-1}). SAR is proportional to the time rate of change of the temperature of the magnetic material and given by the following formula [71]:

$$SAR = \frac{c\,V_s}{m}\frac{dT}{dt} \tag{2.6}$$

where c is the specific heat capacity of the sample (4185 J l^{-1} K^{-1} for water), m is the mass of the magnetic particles, V_s is the total volume and $\frac{dT}{dt}$ expressed in ºK s^{-1} is the temperature increment which is experimentally derived from the linear regression of the initial data points seen on in Figure 2.9.

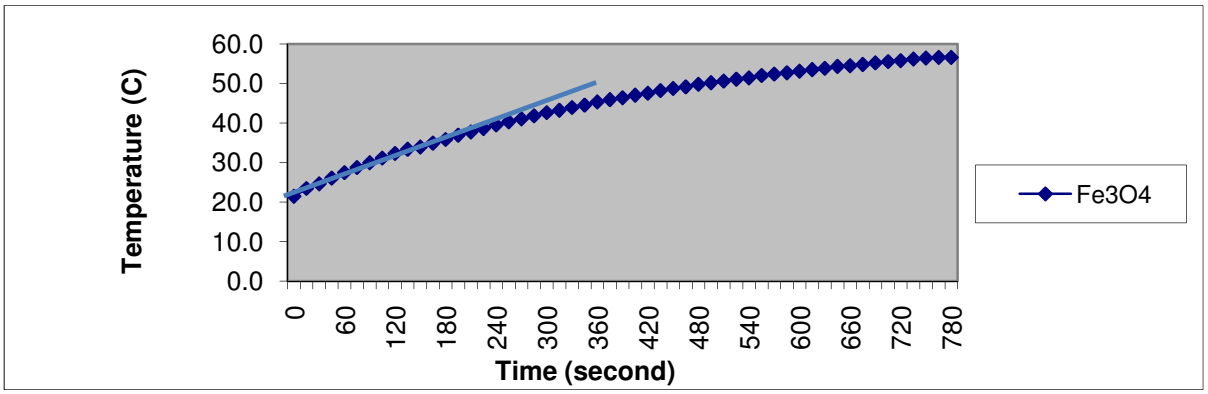

Figure 2.9. Temperature vs. time for superparamagnetic magnetite nanoparticles

Specific loss power SLP is a measurement of the magnetic power loss per unit volume of the magnetic material (W m^{-3}). The loss power is transformed into heat and dissipated to the surrounding medium. SLP is obtained by multiplying SAR by the density ρ (g cm^{-3}) of the magnetic material ($SLP = c\frac{dT}{dt}$).

According to the first law of thermodynamics, change in the internal energy dU of an adiabatic process ($\delta Q = 0$) is equal to the differential of magnetic work energy W on the system

$$dU = \delta Q + \delta W \tag{2.7}$$

$$dU = \delta W = \mathbf{H} \,.\, d\mathbf{B} \tag{2.8}$$

Where W is the magnetic work done per unit volume of the magnetic material [70], **H** is the external magnetic field strength and **B** is the induction flux.

As seen in Figure 2.10 [72], Equation (2.9) suggests that the change of **B** also lags behind that of **H** and just as seen in 2.2.2, this lag can cause the magnetic material to exhibit hysteresis.

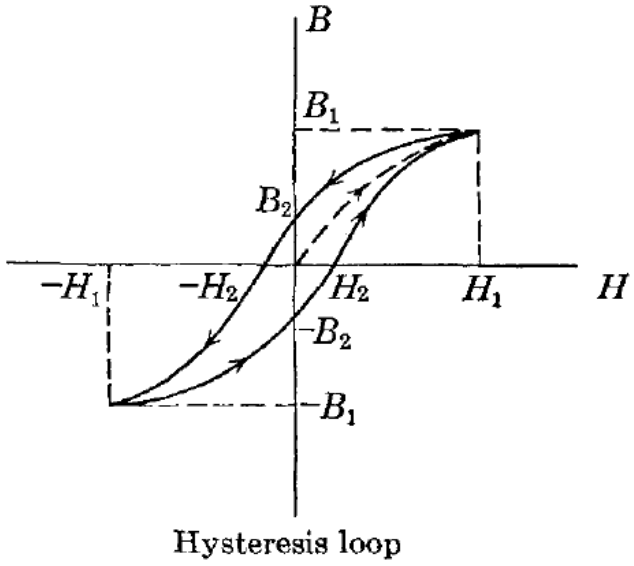

Figure 2.10. Hysteresis of a magnetic material in *B* and *H* axes.

Integration by parts of each segment of the hysteresis curve in respect to dW leads to

$$\begin{aligned} W &= \int_{B_1}^{B_2} \mathbf{H} \,.\, d\mathbf{B}\; dW + \int_{B_2}^{-B_1} \mathbf{H} \,.\, d\mathbf{B}\; dW + \int_{-B_1}^{-B_2} \mathbf{H} \,.\, d\mathbf{B}\; dW + \int_{-B_2}^{B_1} \mathbf{H} \,.\, d\mathbf{B}\; dW \\ &= \left(\mathbf{H} \,.\, d\mathbf{B} \;|_{B_1}^{B_2} - \int_{H_1}^{H_2} \mathbf{B} \,.\, \frac{d\mathbf{H}}{dW} dW \right) + \left(\mathbf{H} \,.\, d\mathbf{B} \;|_{B_2}^{-B_1} - \int_{H_2}^{-H_1} \mathbf{B} \,.\, \frac{d\mathbf{H}}{dW} dW \right) \\ &+ \left(\mathbf{H} \,.\, d\mathbf{B} \;|_{-B_1}^{-B_2} - \int_{-H_1}^{-H_2} \boldsymbol{B} \,.\, \frac{d\mathbf{H}}{dW} dW \right) + \left(\mathbf{H} \,.\, d\mathbf{B} \;|_{-B_2}^{B_1} - \int_{-H_2}^{H_1} \mathbf{B} \,.\, \frac{d\mathbf{H}}{dW} dW \right) \end{aligned} \tag{2.9}$$

$$W = -\oint \mathbf{B} \,.\, d\mathbf{H} \tag{2.10}$$

Due to co-linearity of the fields, the angel between **B** and **H** reduces to zero and therefore the dot product vanishes and B and H become magnitudes [70].

$$W = -\oint B\, dH \tag{2.11}$$

B in Tesla is given by [59]

$$B = \mu_0(H + M) \tag{2.12}$$

where M is the magnetization of the material (A m^{-1}) and μ_0 is the permeability of free space ($4\pi \times 10^{-7}$ T m A^{-1}). Substituting Equation (2.12) into Equation 2.11, magnetic work can be expressed by

$$W = -\mu_0 \oint (H + M)\, dH \tag{2.13}$$

When magnetization lags the field, the integration yields a positive result indicating conversion of magnetic work to internal energy [70], therefore:

$$\Delta U = -\mu_0 \oint M\, dH \tag{2.14}$$

Therefore, the greater the closed area within the hysteresis loop, the greater will be the internal energy.

As described in Section 2.2.3, superparamagnetic nanoparticles do not exhibit hysteresis. However, as described in Section 2.2.4, heat is associated with the energy change through Néel relaxation due to magnetization and demagnetization of the superparamagnetic nanoparticles and rotation of the magnetic moments in an AC magnetic field. Therefore, Néel relaxation can be seen as a form of hysteresis loss for superparamagnetic nanoparticles. For an applied time varying external magnetic field

$$H(t) = Re\left[H_0 e^{i\omega t}\right] = H_0 \cos(\omega t) \tag{2.15}$$

And,

$$\frac{dH}{dt} = -H_0\omega \sin(\omega t) \tag{2.16}$$

Susceptibility on the other hand, consists of both real (Equation 2.18a) and imaginary (Equation 2.18b) components and are given by [70]

$$\chi = \chi' + i\chi'' = \frac{\chi_0}{1 + i\omega\tau} \tag{2.17}$$

$$\chi' = \frac{\chi_0}{1 + (\omega\tau)^2} \tag{2.18a}$$

$$\chi'' = \frac{i\,\omega\tau}{1 + (\omega\tau)^2}\chi_0 \tag{2.18b}$$

which is dependent on DC susceptibility χ_0, angular frequency $\omega = 2\pi f$ and relaxation time τ.

Magnetization as a function of time is therefore given in the following form:

$$M(t) = Re\left[\chi\, H_0 e^{i\omega t}\right] = H_0(\,\chi' \cos(\omega t) + \chi'' \sin(\omega t)) \tag{2.19}$$

Substituting Equation (2.16) and Equation (2.19) into Equation (2.14), the internal energy becomes

$$\Delta U = -\mu_0 \oint H_0(\,\chi' \cos(\omega t) + \chi'' \sin(\omega t))\,(-H_0\omega \sin(\omega t))\; dt$$

$$= \mu_0 H_0^2 \omega \left[\oint \chi' \cos(\omega t)\sin(\omega t) + \oint \chi'' \sin^2(\omega t)\, dt\right] \tag{2.20}$$

Integrating over one period, $1/f$, where f is the frequency and equal to $\omega/2\pi$, the Equation (2.20) leads to

$$\Delta U = \mu_0 H_0^2 \omega \left[\chi' \frac{\sin^2(\omega t)}{2\omega}\,|_0^{2\pi/\omega} + \chi'' \oint \sin^2(\omega t)\, dt\right]$$

$$= \mu_0 H_0^2 \omega \chi'' \int_0^{2\pi/\omega} \sin^2(\omega t)\, dt \tag{2.21}$$

where only the complex susceptibility component survives the integration.

The specific loss power SLP, is equal to the internal energy multiplied by its frequency.

$$\text{SLP} = \frac{SAR}{\rho} = \Delta U\, f = \mu_0 f H_0^2 \omega \chi'' \int_0^{2\pi/\omega} \sin^2(\omega t)\, dt \tag{2.22}$$

where ρ is the magnetic particle density and f is the frequency of the external magnetic field. Solving for the above equation

$$\text{SLP} = \frac{SAR}{\rho} = \mu_0\, f\, H_0^2\, \pi\, \chi'' \tag{2.23}$$

Hysteresis loop for ferromagnetic materials differs from a DC magnetic field to an AC magnetic field. For constant magnetic field amplitude, as the frequency increases, the area of the hysteresis loop increases at first, and eventually decreases [73]. However to avoid complexity, here this factor has not been taken into consideration.

Magnetic nanoparticles prepared with surface stabilizers form magnetic fluids, also known as ferrofluids, are suspended uniformly in a carrier liquid. These materials are single domain and are superparamagnetic. For such particles, relaxation mechanisms are dominant. From Equations (2.23) and (2.18b), SAR is expressed as [70]

$$\text{SAR} = \mu_0\, f\, H_0^2\, \pi\, \chi_0 \frac{2\,\pi\, f\, \tau_{\text{eff}}}{1 + (2\,\pi\, f\, \tau_{\text{eff}})^2}\, \frac{1}{\rho} \tag{2.24}$$

Figure 2.11 (parameters are given in Appendix A.2) plots a simulation of the real and the imaginary components of the susceptibility as given in Equation (2.17). These components meet at the peak value of χ''. In fact, as seen in Equation (2.21), the imaginary component of susceptibility is due to the phase difference between the applied magnetic field and the corresponding magnetization and therefore is responsible for generation of heat. Moreover, χ'' reaches its peak value when $\omega\tau = 1$. In the following sections this will help optimize MNP core diameter for hyperthermia.

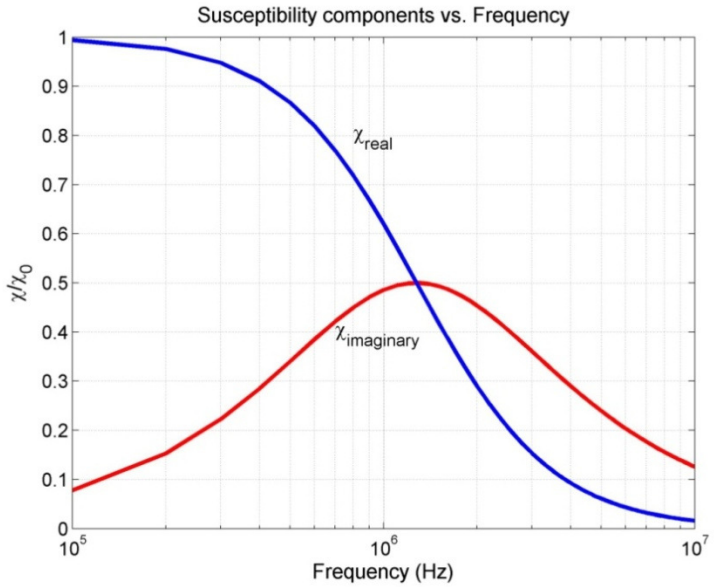

Figure 2.11. Susceptibility components vs. Frequency

2.2.6 Heat Dissipation

There have been many successful attempts to numerically simulate temperature spatial distribution of MNP being excited by an AC magnetic field [74-77]. In each approach, heat transfer equations are used to estimate the thermal behaviour inside and outside of a target volume. In theory, SAR or SLP from the applied AC magnetic field to magnetic particles that are uniformly distributed within a spherical tumour of radius R will dissipate heat to the surrounding tissue until temperature reaches steady state. Figure 2.12 demonstrates this concept, in which r represents the distance from the center of the spherical volume to a point at infinity. Temperature at the surface of the spherical volume is $T_{Initial}$ and reaches minimum temperature T_{Final} (steady state) at distance $r = \infty$. It is assumed that the temperature inside the spherical volume is constant.

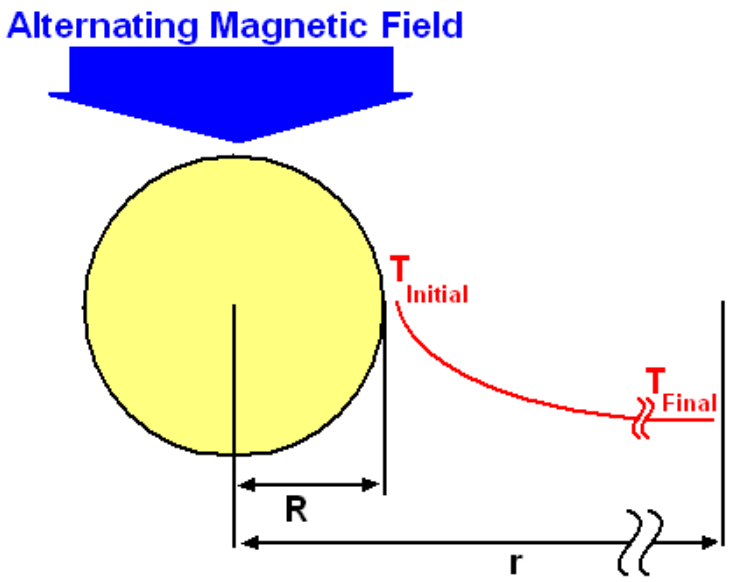

Figure 2.12. Temperature vs. Distance

The tolerable period of exposure of living tissue to an electromagnetic field is limited by physiological constraints and depends on the field parameters. Time dependent thermodynamic heat transfer equations will help optimize the exposure time required to elevate tissue temperature for hyperthermia within the physiological limitations. The following thermodynamic Equations [77] were used to sketch a graphical simulation of ΔT as a function of distance for five arbitrary time values in Figure 2.13 (parameters are given in Appendix A.3):

$$\Delta T_1(r,t) = \frac{PR^2}{6\lambda_1}\left[1 + \frac{q_\lambda}{2}\left(1 - \frac{r^2}{R^2}\right) + \frac{6}{\pi} q_\lambda^{\frac{3}{2}} q^{\frac{1}{2}} \frac{R}{r} \int_0^\infty f(z;r,t) g_1(z;r) dz\right] \qquad \text{for } 0 \le r < R \tag{2.25a}$$

$$\Delta T_2(r,t) = \frac{PR^3}{3\lambda_2 r}\left[1 + \frac{6}{\pi} q_\lambda \int_0^\infty f(z;r,t) g_2(z;r) \frac{dz}{z}\right] \qquad \text{for } r > R \tag{2.25b}$$

With the abbreviations

$$q_\lambda = \frac{\lambda_2}{\lambda_1} \qquad q = \frac{\rho_2 c_2}{\rho_1 c_1} \qquad s(z) = (q_\lambda - 1)\sin z + z\cos z$$

$$f(z;r,t) = z^{-2} \exp\left(-\frac{\lambda_1 t z^2}{\rho_1 c_1 R^2}\right) \times \frac{z\cos z - \sin z}{[s(z)]^2 + q_\lambda q (z \sin z)^2} \qquad g_1(z;r) = \sin\left(\frac{rz}{R}\right)$$

$$g_2(z;r) = \mathrm{s(z)}\,\sin[\,k(z;r)] + (q_\lambda q)^{\frac{1}{2}} z \sin z\ \cos[k(z;r)] \qquad k(z;r) = (\frac{q}{q_\lambda})^{\frac{1}{2}}\, z\left(\frac{r}{R} - 1\right)$$

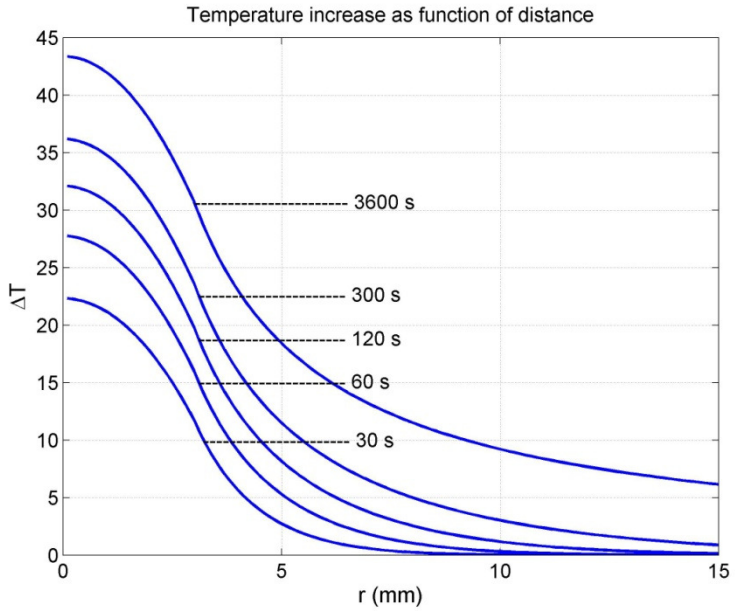

Figure 2.13. Time dependent temperature increase as function of distance

where P is the SLP, λ_1 and λ_2 represent values of heat conductivity for medium 1 (for $0 \leq r < R$) and 2 (for $r > R$) respectively, c_1 and c_2 are heat capacity coefficients and ρ_1 and ρ_2 are mass densities for the medium 1 and 2 respectively. The parameter z is to help integrate from 0 to infinity and does not have a physical meaning. The above graph is plotted using a numerical integration technique. To estimate thermal effect in various tissues, values of $\lambda,\ c,\ \rho$ for different biological tissues can be taken from literature [78]. Each curve in Figure 2.13 represents the thermal dissipation with respect to distance from the center of spherical volume for a given time interval. As expected, the longer the duration of the magnetic induction process, the higher the thermal effect at the center of the spherical volume. Also it can be seen that temperature drops rapidly a few millimetres away from the surface of R. This means that in a hyperthermia application, unnecessary heat can be kept away from healthy surrounding tissue.

The following sections in this chapter are allocated for understanding of properties that would allow for highest SAR value with minimum dosage of MNP.

2.3 Magnetic Properties Suitable For Hyperthermia

Magnetic properties suitable for hyperthermia are not only governed by the magnetic parameters of the MNP but also by the physiological limitations that are set to protect living organisms against high magnetic fields. By optimising these properties, maximum SAR and thermal effect can be reached and therefore fewer MNP are required at the target area. In this section some of the magnetic parameters and limitations are discussed.

2.3.1 MNP Physical Parameters

2.3.1.1 Size

The size of the MNP influences the value of SAR and therefore the thermal effect. As explained before, an area within a wide hysteresis loop leads to dissipation of more heat than does a narrow hysteresis loop. Assuming constant magnetization saturation M_S, coercive field H_C defines width of the hysteresis loop. There is a relationship between particle core size and the coercive field. As shown in Figure 2.14 [59], the H_C is at its largest value for particles that are at the border of between being single and multi-domain. Superparamagnetic nanoparticles show no hysteresis and therefore it is not surprising to see that they do not have any coercive field.

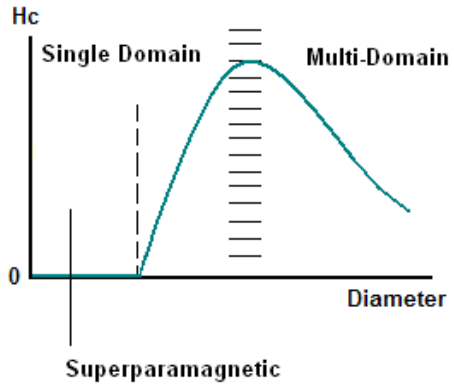

Figure 2.14. Coercive field vs. particle diameter

Figure above suggests that particles resting on the border between single and multi-domain exhibit the highest value of SAR and thus are the best choices for hyperthermia. In a study, Zhang *et al.* [79] showed that due to technical and biocompatibility issues, the applied AC

magnetic field is often much lower in amplitude than the field required to saturate all magnetic moments of MNP. Conceptually, to benefit from heat generation by a complete hysteresis loop, particles have to magnetically saturate to extremely high fields on the order of a few thousand Oersted. Such fields may cause unwanted tissue heating, stimulation of peripheral and skeletal muscles and irreversible biological effects such as cardiac fibrillation [80]. Therefore, adequate magnetic field and frequency necessary to make use of the entire hysteresis loop would be too high to consider for hyperthermia. In addition, because an ensemble of multi-domain MNP align randomly with the magnetic field, practically only 25% of the ideal maximum theoretical power may be dissipated as heat [81].

According to Okawa *et al.* [82], under a moderate and physiologically tolerable AC magnetic field, the single domain MNP of 18 nm in diameter reached target temperature of 43ºC quicker than superparamagnetic and multi-domain MNP. This claim is also in close agreement with the findings of Johannsen *et al.* [83] in which magnetite nanoparticles of 15 nm in diameter were used to elevate tumour temperature *in vivo* tests.

As mentioned at the end of Section 2.2.5, the imaginary component of susceptibility is responsible for the heating of MNP inside an AC magnetic field. It was also shown that this component is at its highest value when $\omega\tau = 1$ where ω is the angular frequency and τ is the effective relaxation time. In highly viscous media such as tissue, the effect of the Brownian relaxation time on the effective relaxation time τ is negligible and Néel relaxation time τ_N is the dominant factor [76]. Using Equation (2.24), Figure 2.15 (parameters and calculations are given in Appendix A.4) simulates how SAR due to Néel relaxation behaves as size of the iron oxide MNP varies. Frequencies of 20 kHz, 200 kHz and 2 MHz were randomly chosen to display the effect of frequency on SAR.

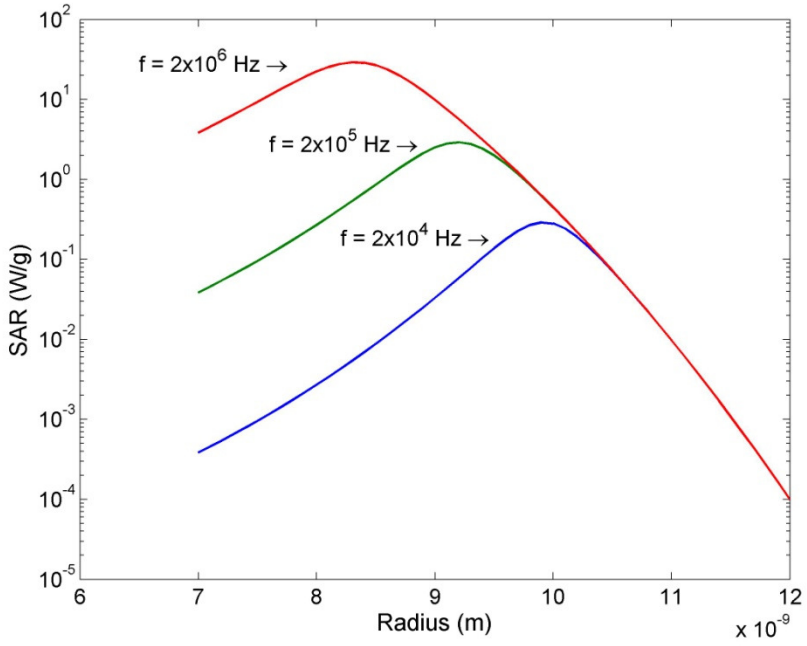

Figure 2.15. Power loss due to Néel relaxation vs. radius of MNP

2.3.1.2 Concentration of MNP

In steady state temperature difference ΔT is given by [84]

$$\Delta T = \mathrm{SAR}\frac{\mathrm{c}\,R^2}{3\lambda} \tag{2.26}$$

where c is the concentration of the MNP (mass of the particles per tissue volume) and λ represents the heat conductivity of a tissue volume with a radius R. From the above equation it is evident that higher concentration of MNP in the tissue leads to higher ΔT.

Earlier in Section 2.2.1 it was mentioned that one of the factors affecting the effective anisotropy constant K is the dipolar magnetic interaction generated by each particle in the external magnetic field on the neighbouring particles. Therefore, when the number of MNP is altered, there will be a change in the dipolar interaction of MNP. As a result, change in the concentration of MNP will lead to a small change of the K value [85]. This alteration however, is considered insignificant in this investigation.

2.3.2 Limitations to Amplitude and Frequency of the AC magnetic field

In order to prevent deleterious physiological responses from time varying magnetic fields, there are guidelines limiting magnetic field parameters. These guidelines are obtained from scientific observations and epidemiological studies. For biomedical purpose, the frequency of the electromagnetic field has to be higher than 50 kHz to avoid neuromuscular electro-stimulation and lower than 10 MHz for appropriate penetration [4]. Available experimental data shows that the resting human body temperature can be elevated up to 1°C if it is exposed to an electromagnetic field that produces a whole-body SAR of between 1 and 4 W kg^{-1} [80]. Eddie current loss produced by closed currents induced by alternating magnetic flux in a conductive tissue of sufficient area are responsible for this type of heating [86]. Harmful levels of tissue heating can be produced by exposure of the tissue to fields at higher SAR values. Atkinson *et al.* [87] therefore, established an upper limit of 4.85 x 10^8 A m^{-1} s^{-1} for the product of field amplitude (H_0) and frequency (f) for a single turn induction coil around the thorax of a normal size patient. For such body exposure, a tissue load threshold of 25 mW ml^{-1} was recommended by Jordan *et al*. [86]. Power density absorbed by the tissue is given by

$$P_{tissue} = \pi^2 \frac{\mu^2 \mu_0^2 \sigma_T}{2} f^2 r^2 \mathrm{H}_0^2 \qquad (\mathrm{W\ m^{-3}}) \qquad (2.27)$$

where μ is the permeability and μ_0 is the permeability of free space, σT is the conductivity of the tissue, f stands for frequency, H_0 is the external field strength and r is the distance from the central axis of the body. Using the above equation and the upper limit to the product of the field amplitude and frequency, the following graph (Figure 2.16) is simulated and plotted (parameters are given in Appendix A.5).

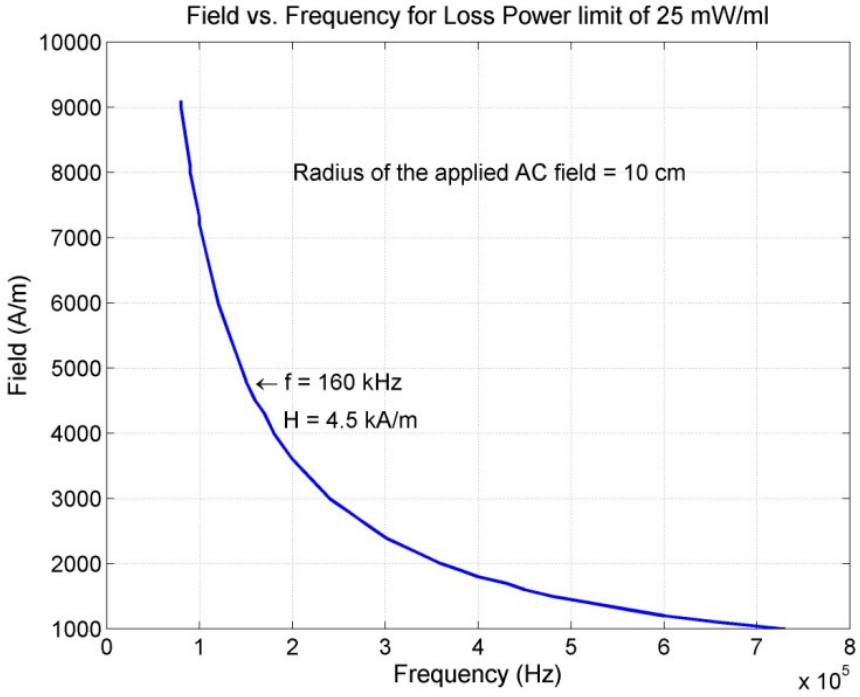

Figure 2.16. Biological limitation to field and frequency

In the above graph, the curve represents the upper limit for H_0 and f that can be used for patients with a body cross section of 10 centimetres in radius at tissue load limit of 25 mW ml^{-1}. This simulation also took into account values for biological tissue conductivity ranging from 0.0144 S m^{-1} to 0.68 S m^{-1} as tabulated in [78] for frequencies in the range of 100 kHz to 1 MHz. Since eddy current power density is proportional to the square of the diameter of the induced current loops, the proposed upper limit can be accordingly larger for smaller body regions under AC magnetic field exposure. For example, a higher limit of $H_0 \times f = 4 \times 10^9$ A m^{-1} s^{-1} has been suggested for treatments of the breast cancer [88].

When an electromagnetic wave passes through the human body, as it heats the tissue it also declines in intensity. This is given by

$$I = I_0 \exp(-2 \propto_E x) \qquad (\mathrm{W\ m^{-2}}) \qquad (2.28)$$

$I_0 < 100$ $(\mathrm{W\ m^{-2}})$ maximum safe incident intensity $\propto_E = \propto_e n_E^{1/2}$

where *I* is the power per unit area transmitted through the tissue, *x* is the penetration depth of the tissue, $\propto_E$ is the total attenuation factor including scattering and absorption. n_E is the incident frequency and $\propto_e$ averages $\sim 5 \times 10^{-3}$ $\sec^{1/2}\text{m}^{-1}$ for soft tissue [89]. According to Equation 2.23, at 1000 MHz (microwave) more than 90% of power is lost in approximately 15 mm depth of the soft tissue; at 30 GHz incident power has lost 99% of its energy in less than 10 µm depth in the tissue. On the other hand, 67% of the energy is passed through a thickness of 10 cm tissue un-scattered and un-absorbed at 160 kHz. This suggests a suitable frequency range (~100 kHz) for proper penetration of the AC magnetic field and excitation of the MNP at a deep target area. To simplify calculations, here the biological load is assumed to be isotropic and homogeneous and its cross section exhibits cylindrical symmetry to the induction coil. Also the magnetic field within the coil and tissue load is assumed to be uniform and field penetration into the dielectric material is complete. Moreover, the tissue under study is far away from any metalic implants that could affect the field in any way. Last but not least, it is assumed that there is no axial electric field within the coil.

In addition to the above, a study involving electromyography recording of human arm [90] showed that a derivative of the AC magnetic flux density $\frac{dB}{dt}$ greater than 10^4 T s^{-1} was required to stimulate the median nerve trunk. As simulated and shown in Figure 2.17, an AC magnetic field of 4500 A m^{-1} at 160 kHz is far from this limit and could not stimulate median nerve trunk.

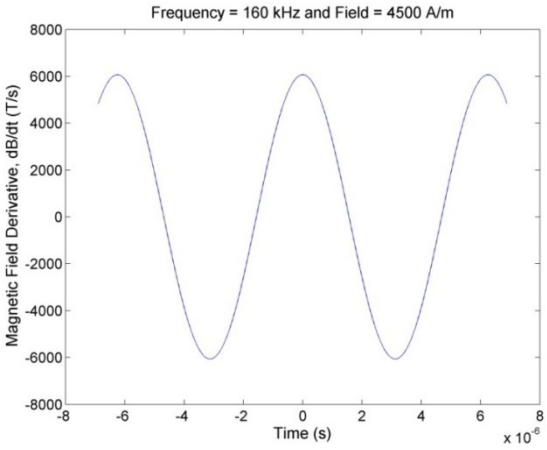

Figure 2.17. dB/dt for Frequency = 160 kHz and Field = 4500 A m^{-1}

2.4 Hydrogel Encapsulated MNP

Hydrogels are polymers that are able to absorb large quantities of water without dissolving or losing their three dimensional structure. They are used in biomedical applications because their physical properties are similar to those of living tissue and they are highly biocompatible. Some hydrogels are known as “smart” gels due to their response to an external stimulus, such as change in temperature, pH, magnetic fields, etc. Thermo-responsive hydrogels are particularly of high interest in which N-isopropylacrylamide (PNIPA) hydrogel is the most familiar type. PNIPA has an inverse response to temperature elevation, that is, it reduces size when heated and swells when cooled down [11]. This discontinuous and reversible mechanism caused by internal structure changes due to the presence of hydrophobic groups occurs at lower critical solution temperature (LCST). At temperatures below LCST (Figure 2.18), hydrogen bonds between hydrophilic groups of the polymer chain are dominant, i.e. dissolution of water has increased. When temperature is increased to LCST (Figure 2.19), hydrogen bonds become weak and hydrophobic interactions become stronger, which results in a change in the internal structure, so water is expelled out of the hydrogel. This phenomenon results in color change (become opaque) and volume change. The LCST of PNIPA hydrogel alone is at 32°C, and can be set above body temperature by copolymerization with hydrophobic monomer like acrylic acid [91, 92]

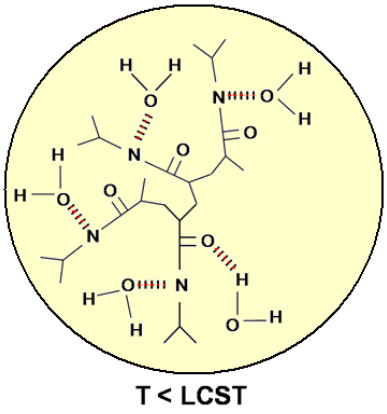

Figure 2.18. PNIPA at Temperature less than LCST

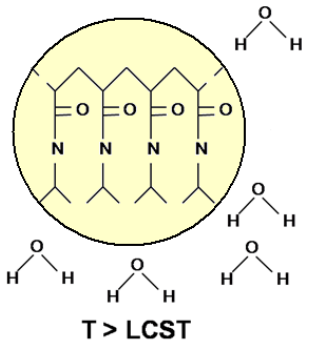

Figure 2.19. PNIPA at Temperature greater than LCST

2.4.1 MNP Embedded in PNIPA Hydrogel for Drug Delivery

As described before, induction of MNP can provide the necessary heat for hydrogel to shrink and reduce its volume. In this case, as illustrated in Figure 2.20, MNP are embedded within the gel and assist in elevation of hydrogel temperature once placed in an AC magnetic field. There, the energy from the magnetic field is transformed into heat and then transferred from the MNP to the hydrogel, thus increasing its temperature. The LCST was determined to be 29°C. The interaction between MNP and/or the polymer coating with the hydrogel may have had an effect on reduction of LCST.

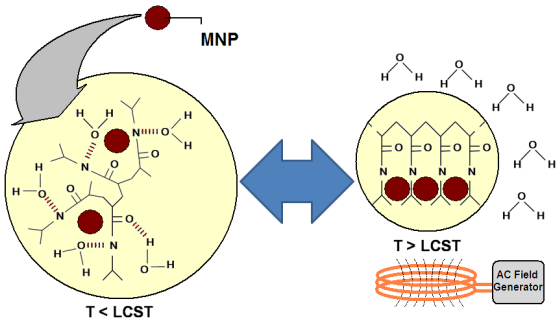

Figure 2.20. MNP embedded in PNIPA hydrogel

The goal here is to integrate MNP with therapeutic agents in micro-carriers made of PNIPA hydrogel that are capable of transiting through the very small diameter blood vessels of the human vasculature. These micro-carriers can be navigated towards a target such as a tumour using a gradient magnetic field of a clinical MRI. As depicted in Figure 2.21a, instead of relying on one large magnetic core to propel and steer such micro-carriers in the vascular network, the proposed hydrogel micro-carriers rely on an agglomeration of the MNP embedded within the hydrogel. As such, the MNP are also used for propulsion through an induction of the magnetic gradients generated by a clinical MRI system. This also allows tracking of the micro-carriers as a local distortion of the magnetic field inside the MRI system, where the confirmation of the homogenous distribution of the micro-carriers within the target volume prior to drug release would be feasible [38]. Once the micro-carriers are immobilized by means of embolization (Figure 2.21b), an AC magnetic field can cause the embedded MNP to heat the PNIPA hydrogel and as such, actuate a drug release sequence. At this time, as a result of a reduction in hydrogel volume, a fraction of the embedded MNP, H_2O, and therapeutic agents can be liberated, allowing

the micro-carrier to move closer to the target area. In addition to the influence of therapeutic agents on target cells, released MNP around the target area can be made to bond with the target tissue surface and cell membranes by means of antibodies. The change of target tissue surface may cause a change in the topography cues of the environment and target cells where it may influence cell cytoskeleton formation and encourage the cells to switch from growth to apoptosis [37].

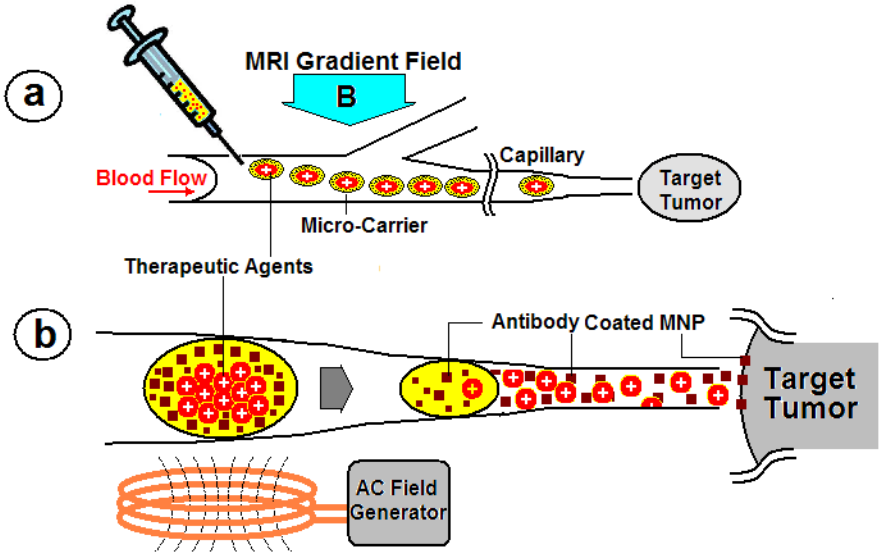

Figure 2.21. PNIPA- MNP as hyperthermic actuator for drug delivery in the vascular network

2.5 MNP and the Gradient Magnetic Field

As seen in the Figure 2.20, the gradient of the magnetic field in MRI steers the micro-carriers to the target tumour. The torque and the force created by an MRI magnet can be calculated from [61]

$$\vec{\tau} = \vec{\mu} \times \vec{\boldsymbol{B}} = \vec{\boldsymbol{M}}\, V \times \vec{\boldsymbol{B}} \tag{2.29}$$

$$\vec{F} = (\vec{\boldsymbol{M}} V . \boldsymbol{\nabla}) \vec{\boldsymbol{B}} \tag{2.30}$$

In the above equations, τ is the magnetic torque (N.m), F is the magnetic force (N), $\vec{\boldsymbol{M}}$ is the magnetization of the material (A m^{-1}), V is the volume of the magnetic material (m^3), $\vec{\boldsymbol{B}}$ is the magnetic induction (T) and $\boldsymbol{\nabla B}^{\rightarrow}$ is the gradient (spatial variation) of the magnetic induction (T m^{-1}). It is seen from Equation (2.30), that the magnetic force required to steer micro-carriers in Figure 2.21 is not dependent on the size of the individual nanoparticle but the volume of an ensemble of the MNP within the micro-carriers. Size of the MNP however, has direct impact on change of temperature upon exposure to the AC magnetic field. Therefore, there are no size related constrains for propulsion of an ensemble of MNP encapsulated inside micro-carriers that are functionalized for moderate hyperthermia.

Rigid objects such as micro-carriers face a drag force by the moving fluid in a rigid cylindrical tube such as the blood vessels. This force is dependent on the fluid density, velocity of the object, frontal area and the ratio of the object diameter to the cylinder diameter. Micro-carriers can be propelled by the gradient field force if this force is stronger than the drag force of the blood flow on the micro-carriers. In this regard, a 1.5 mm ferromagnetic bead was navigated through the carotid artery of a living swine by the gradient of a 1.5T clinical MRI [93]. This important realization opens new doors to a navigable hyperthermic based drug release mechanism.

CHAPTER 3 EXPERIMENTAL METHODS

In this chapter, experimental methods are presented to validate and support the theoretical explanations as well as the mathematical simulations shown in the previous chapters.

3.1 Induction Heating Machine

To obtain a sinusoidal AC magnetic field on the order of a few tens of amperes per meter at hundreds of kilohertz, a 1.5 kW induction heating machine was allocated from Norax Canada Inc. This machine, shown in Figure 3.1, is originally engineered to induce eddy currents on the metal surface and heat it near to the melting point. The eddy current is generated by tens of amps at relatively high frequencies through a cylindrical copper tube coil surrounding the metal. The device is cooled down by cold water.

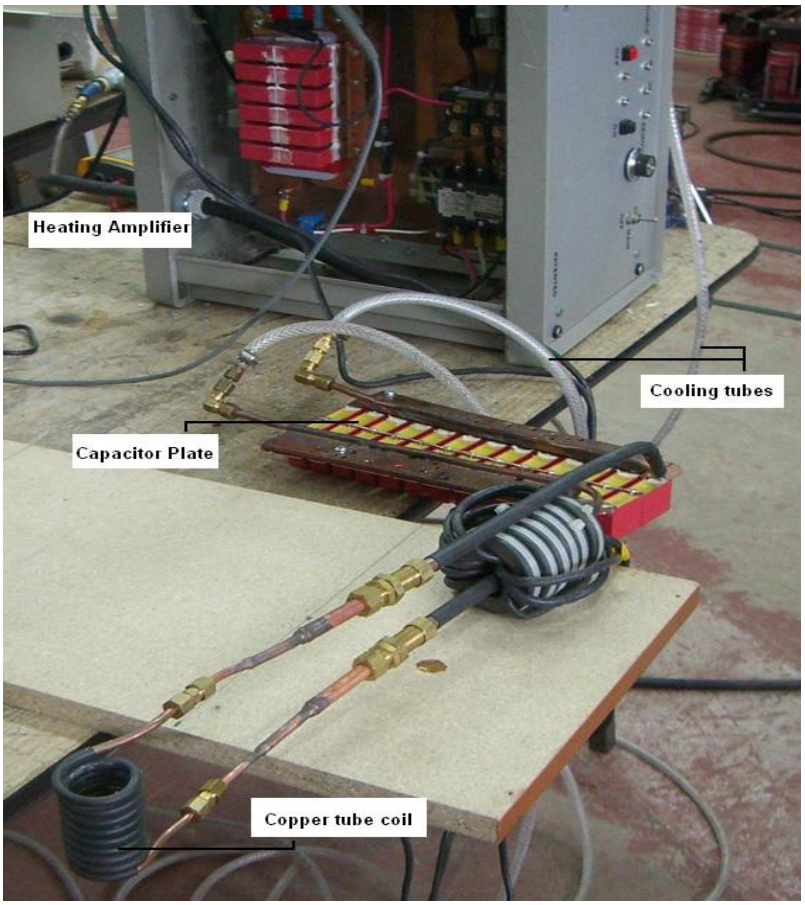

Figure 3.1. Norax Canada Inc. induction heating machine

Following the convincing results from preliminary tests with the device shown in the Figure 3.1, a more sophisticated induction heating machine was purchased from Ameritherm Inc™. This device, shown in Figure 3.2, consists of a 2 kW amplifier, a heat station and an induction copper tube coil. The coil is attached to the heat station and the entire device is cooled by a water-to-air cooling system (not shown in the Figure below).

Figure 3.2. Ameritherm Inc™ HotShot 2kW induction heating

The amplifier is able to run a few hundred amps into the coil through the heat station and generate large magnetic fields at a theoretical frequency range of 150 to 400 kHz. The exact frequency depends on the inductance of the coil and the matching capacitance inside the heat station. This device was selected because of its comparatively low frequency range. As mentioned before in Section 2.3.2, at hundreds of kilohertz the penetration of the magnetic field in the biological tissue is the largest and suitable for moderate hyperthermia. Necessary calculations were done to match the coil dimensions and its inductance with the capacitance of the heat station for the minimum available frequency of 150 kHz. A three turn copper tube coil was constructed with a diameter of 67 mm and allowed a frequency of 160 kHz. As depicted in Figure 3.3, for this frequency, the SAR due to Néel relaxation is at its maximum for magnetite nanoparticles of approximately 20 nm in diameter.

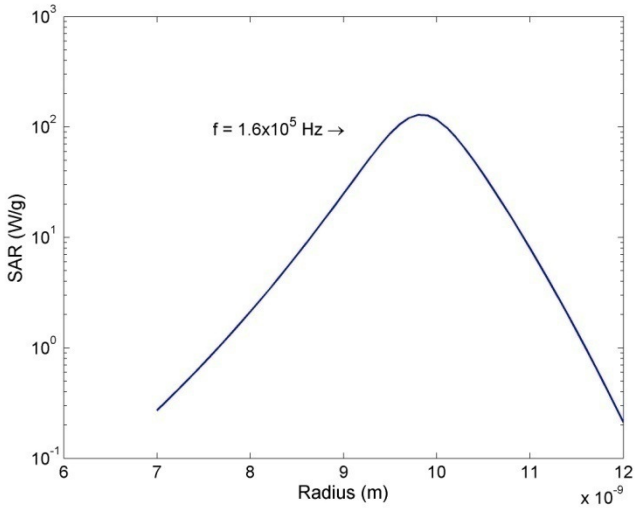

Figure 3.3. Loss power due to Néel versus radius of MNP at 160 kHz

Once the frequency is selected, the upper limit of the magnetic field strength can be obtained from the mathematically simulated biological limitation curve illustrated in Figure 2.16. This upper limit is set to be 4500 A m^{-1}.

3.2 Experimental Trials

Commercially available 20 nm magnetite nanoparticles suspended in water were purchased from two different companies: micromod and chemicell GmbH. The magnetic properties as well as core diameter of these particles were then verified by vibrating sample magnetometer (VSM: EV5, Magnetics) and transmission electron microscopy (TEM: Jeol JEM-2100 operated at 200 kV). Unfortunately, it quickly became evident that the advertised magnetic core size of these particles was larger than reality. The images from TEM showed that the nanoparticles consisted of sub-particles of much smaller core size. This had major effect on the expected thermal behaviour of the nanoparticles and the SAR value never reached its maximum potential.

3.2.1 Magnetic Fluid

Magnetic fluid magnetite nanoparticles purchased from micromod (Product number: 79-00-201, Rostock-Warnemuende, Germany) were observed by TEM to confirm their crystal structure (Fe_3O_4) and their size distribution. These particles were uniformly suspended in aqueous solution and contained 50% dextran polymer as their coating to prevent large dipole-dipole interactions

between the MNP. This was verified by the atomic absorption spectrometry (AAS: Thermo Scientific S Series). Figure 3.4 demonstrates TEM images from agglomeration of these MNP.

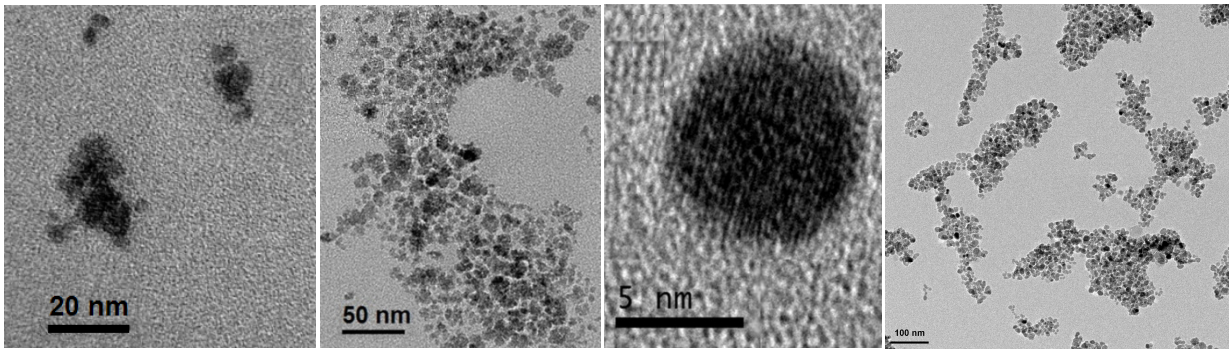

Figure 3.4. Magnetite nanoparticles purchased from micromod

The images of Figure 3.4 show that the core diameters of the particles vary in a narrow size distribution range between 7 to 10 nm. Figure 3.5 illustrates the crystal diffraction patterns corresponding to magnetite (Fe_3O_4) as chemical composition of the particles.

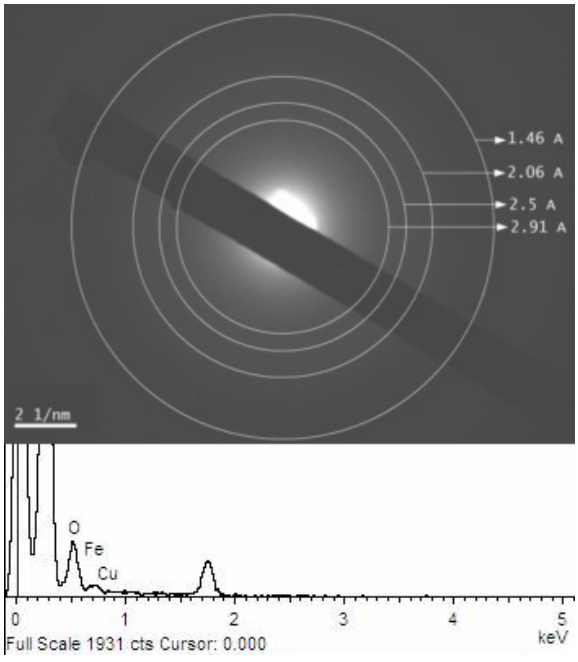

Figure 3.5. Confirmation of magnetite nanoparticles composition

The VSM reported a magnetization saturation M_S value near 43 emu g^{-1} for these nanoparticles. This is almost half of the values found in the literature for bulk magnetite. Other than what was

explained in Section 2.2.2, this can be due to the large amount of dextran coating that was confirmed earlier by AAS measurements. Coercive field H_C was measured to be relatively small at 0.88 Oersted (Oe), which is an implication of the superparamagnetic behaviour.

Magnetic fluid magnetite nanoparticles purchased from chemicell GmbH (Berlin, Germany) were also promised to be 20 nm in diameter. These particles came in eight different coatings; Starch, Oleic acid, Polyacrylic acid, Poly (maleic acid-co-olefin), Polyvinyl alcohol, SiMAG Carboxyl and two types of uncoated MNP: anionic and cationic charge. The images provided by TEM are presented below in Figure 3.6 and show that some nanoparticles have different shapes and core size distribution.

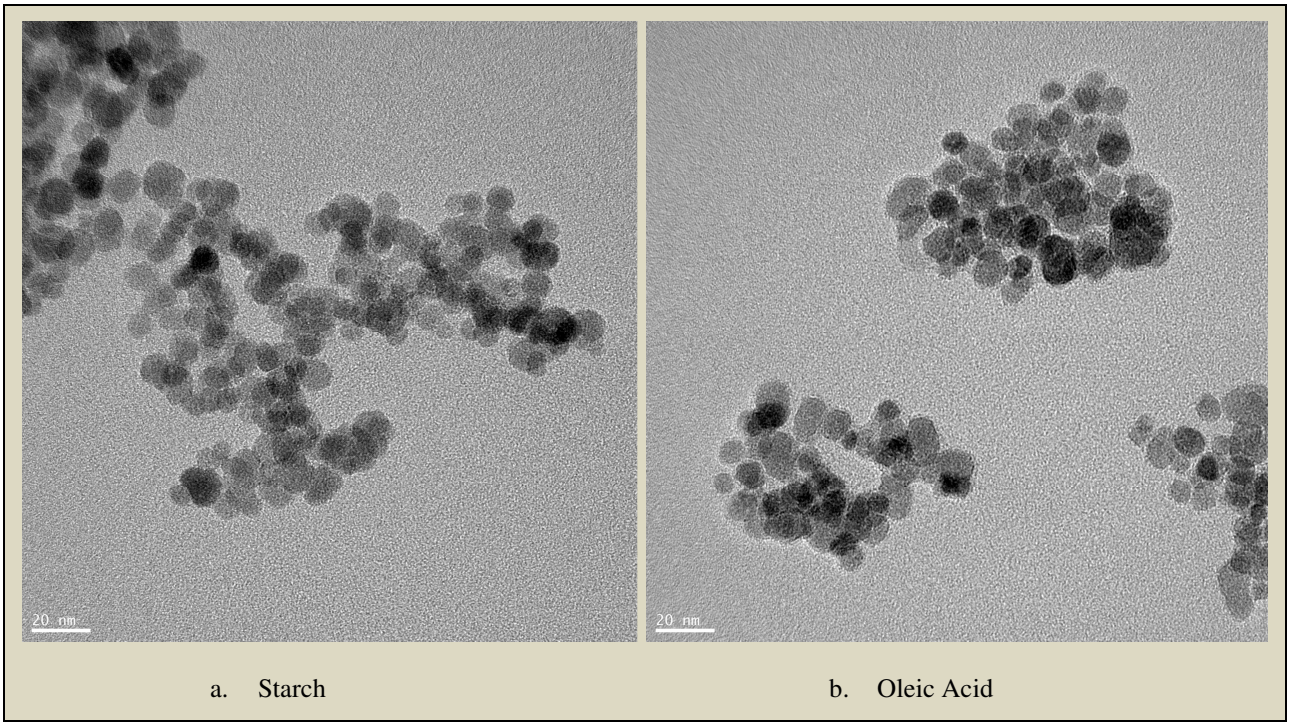

a. Starch

b. Oleic Acid

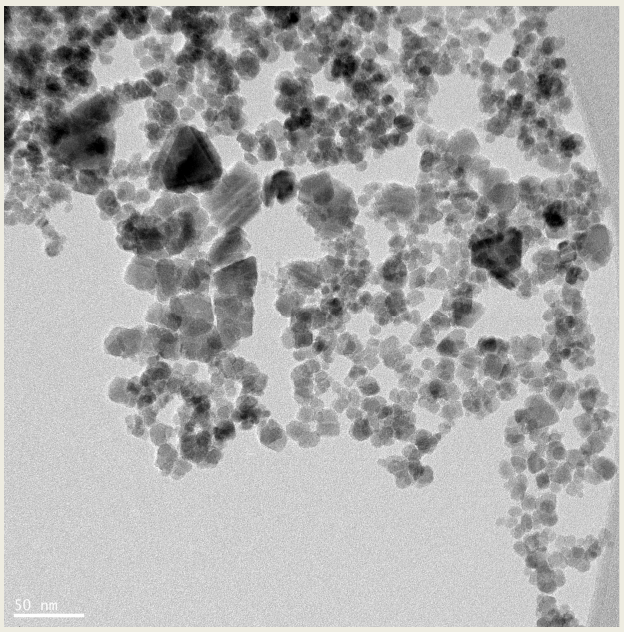

c. Polyacrylamide

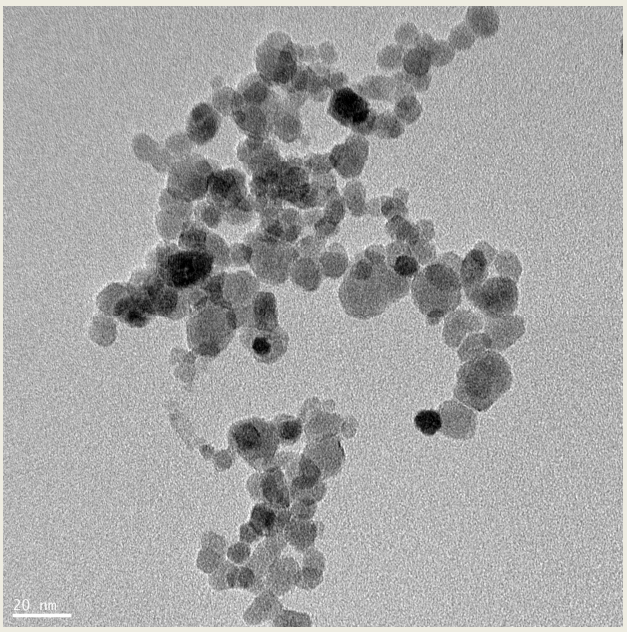

d. Poly(maleic acid-co-olefin)

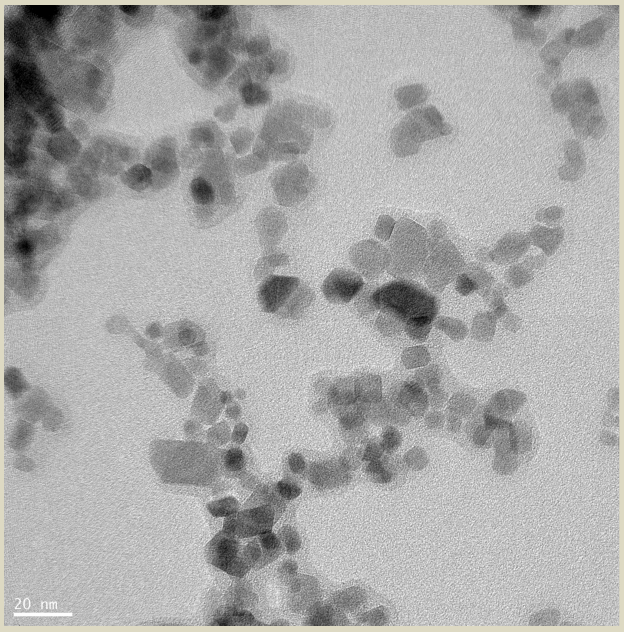

e. Polyvinyl alcohol

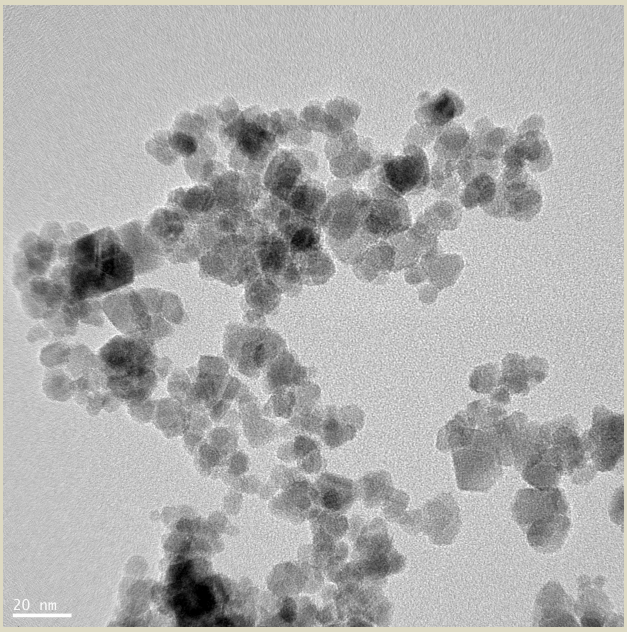

f. SiMAG, Carboxyl

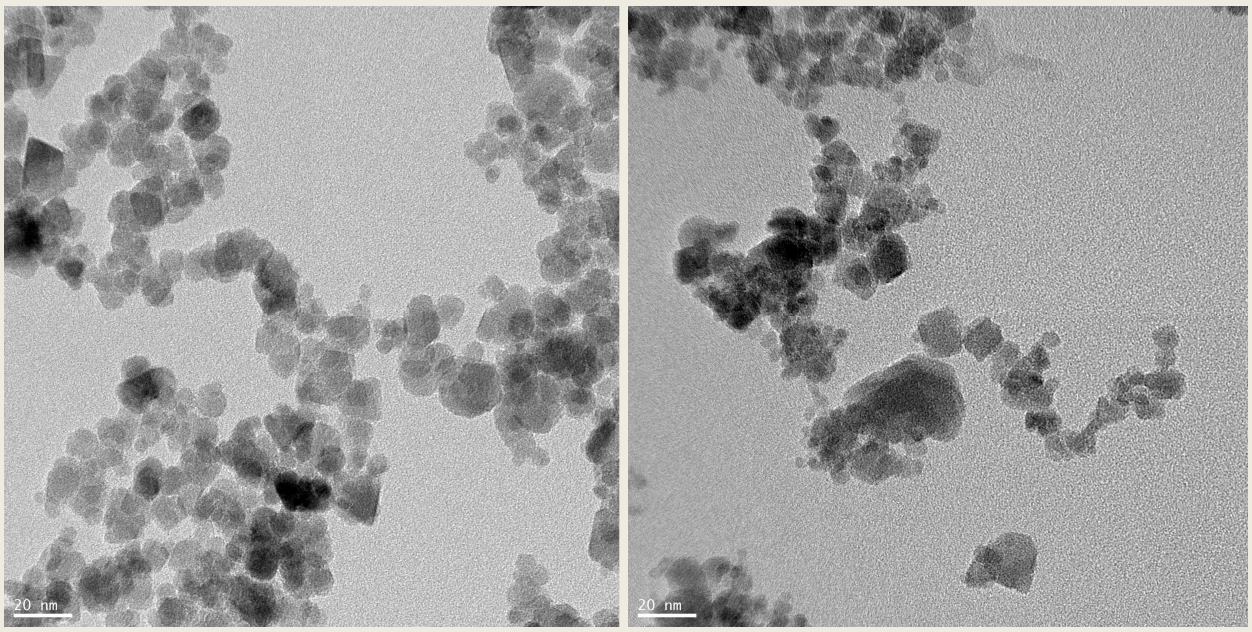

g. Uncoated Anionic h. Uncoated Cationic

Figure 3.6. TEM images from chemicell GmbH magnetite MNP

For these MNP, the crystal diffraction patterns corresponded to magnetite Fe_3O_4 composition. The *M-H* curves provided by VSM show very narrow hysteresis losses and in some cases a complete lack of hysteresis losses is evident. These curves are depicted below in Figure 3.7.

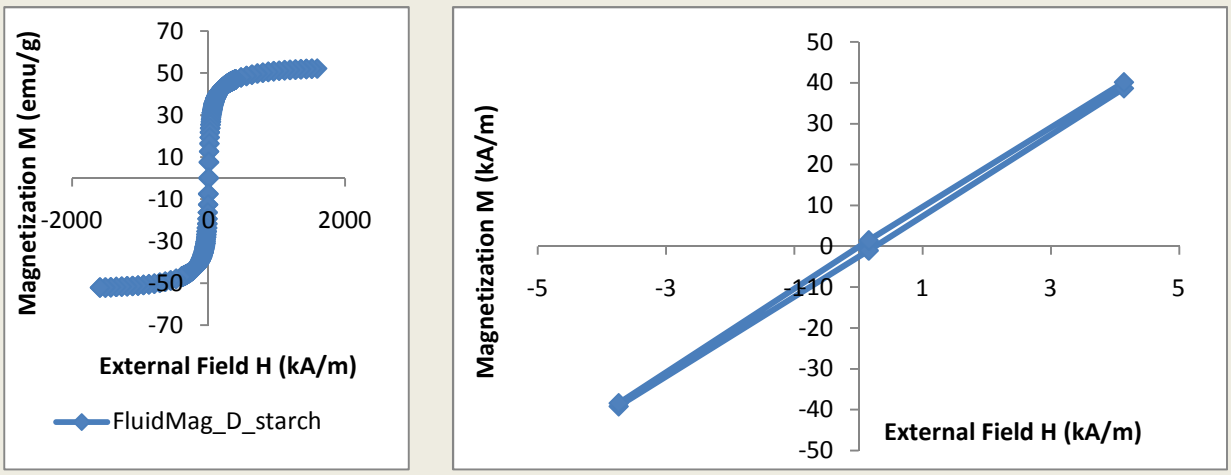

fluidMAG-D: Starch

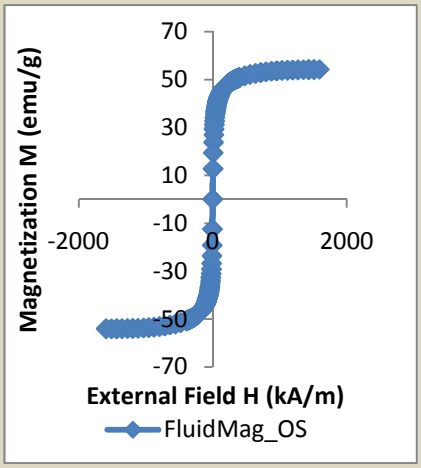

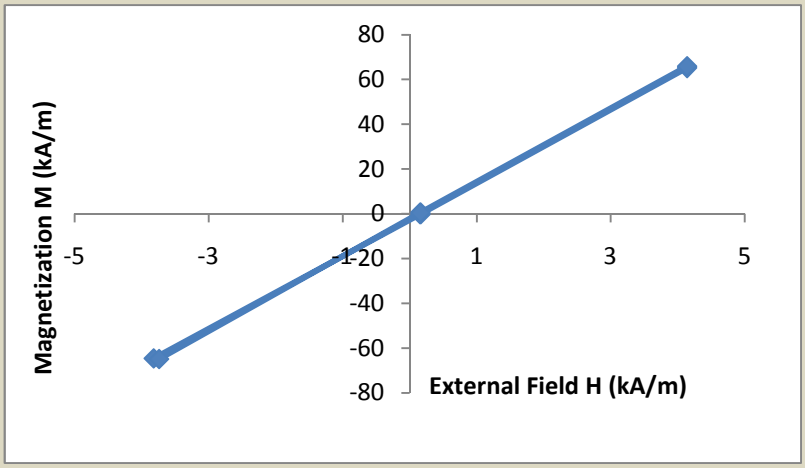

fluidMAG-OS: Oleic Acid

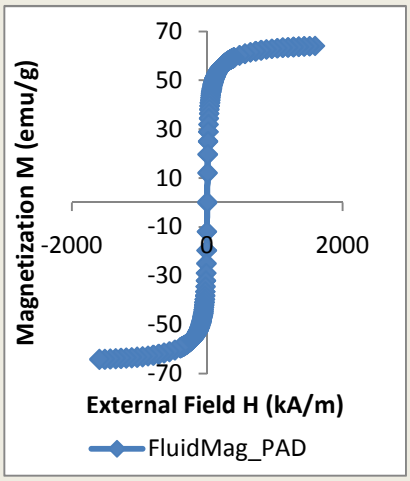

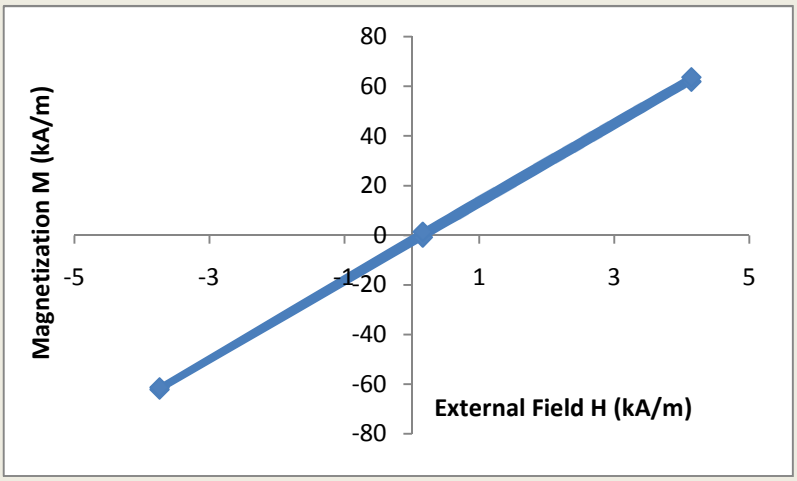

fluidMAG-PAD Polyacrylamide

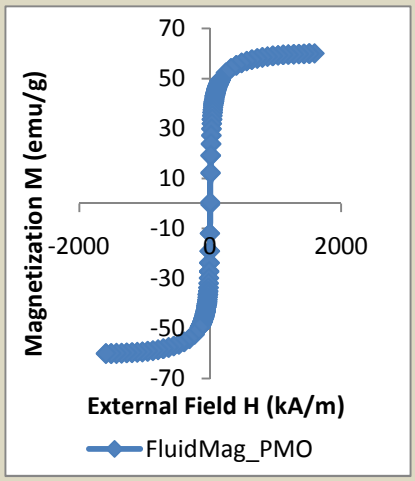

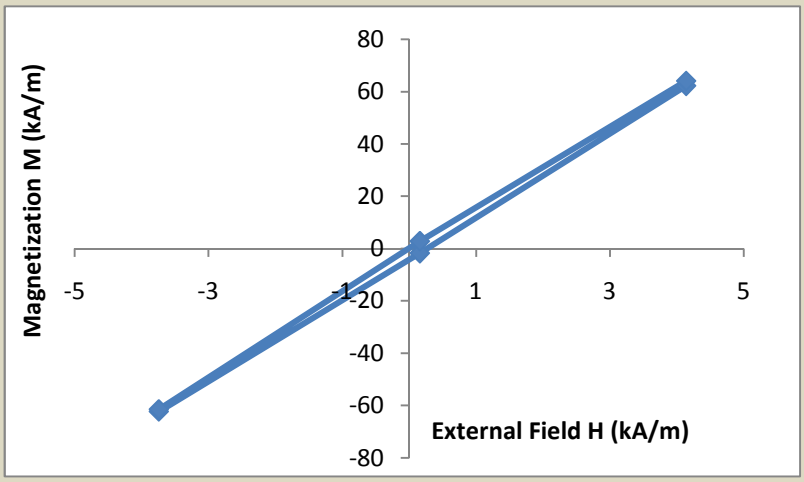

fluidMAG-PMO: Poly(maleic acid-co-olefin)

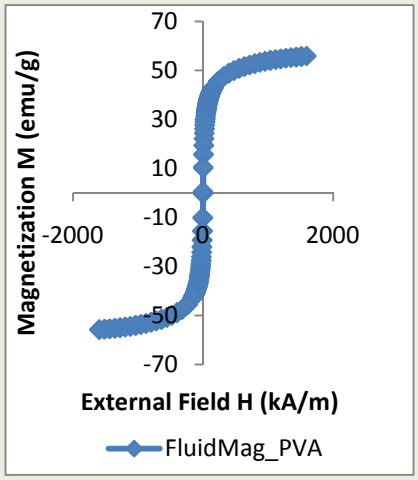

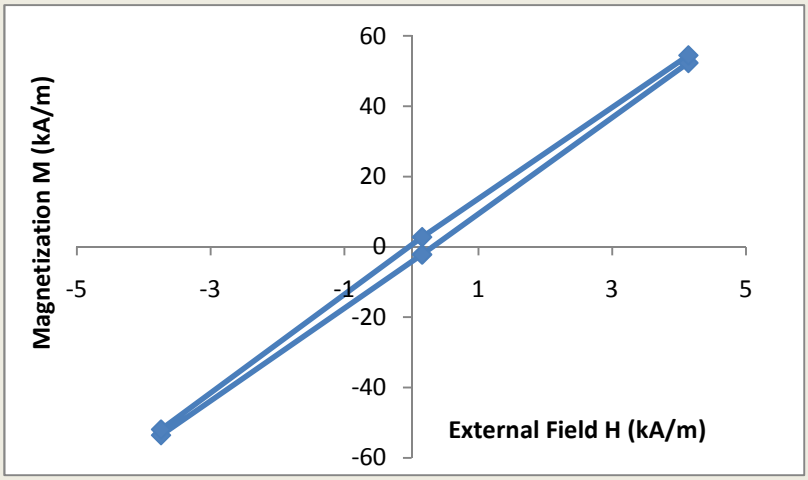

fluidMAG-PVA: Polyvinyl alcohol

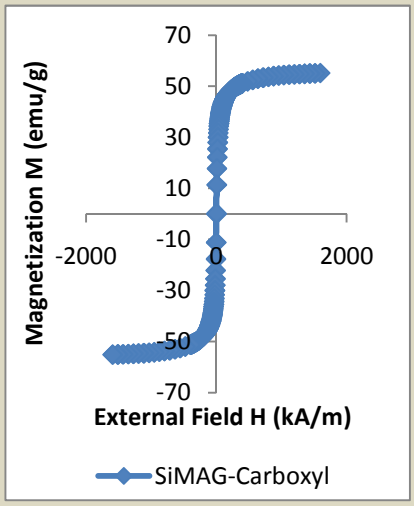

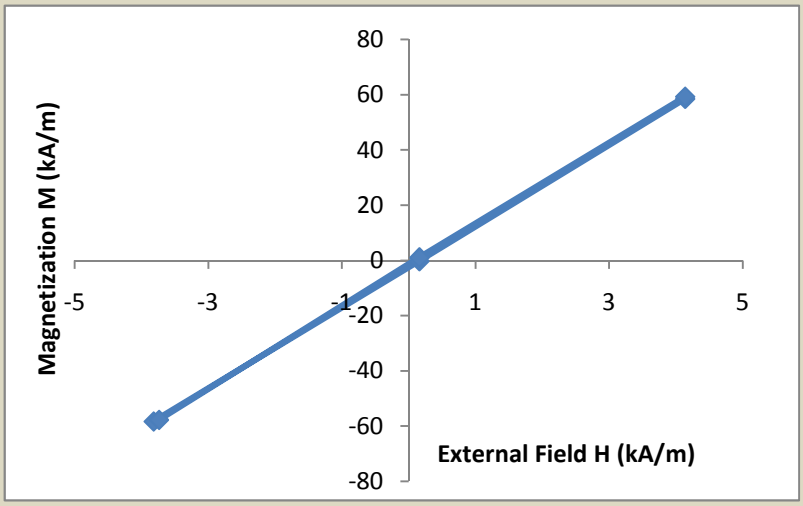

SiMAG-Carboxyl: Silica, non-porous

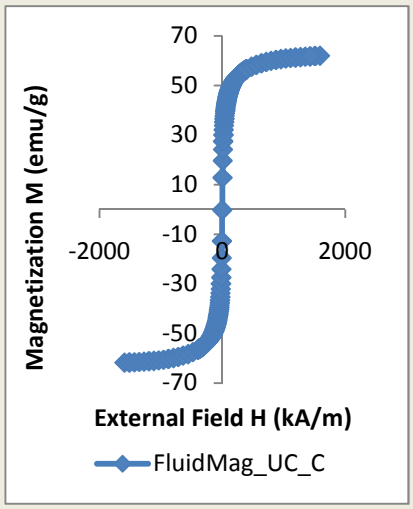

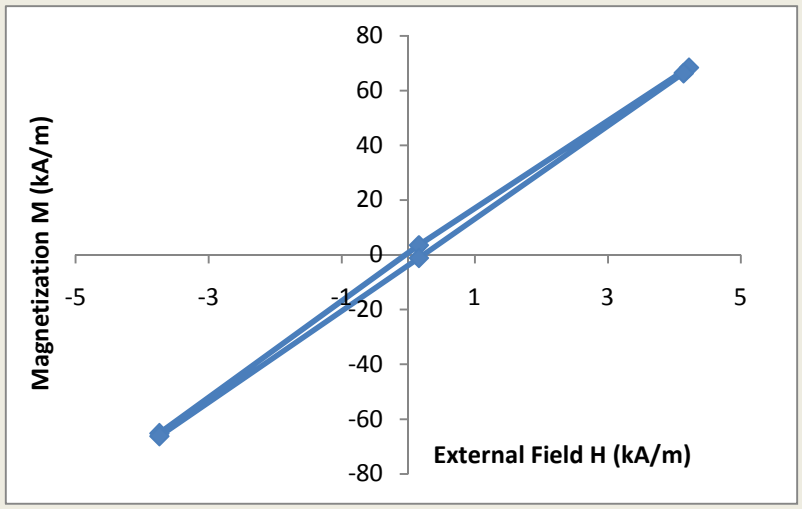

fluidMAG-UC/C: Uncoated Cationic

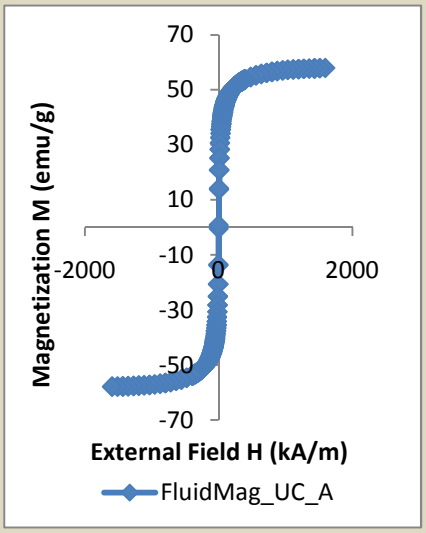

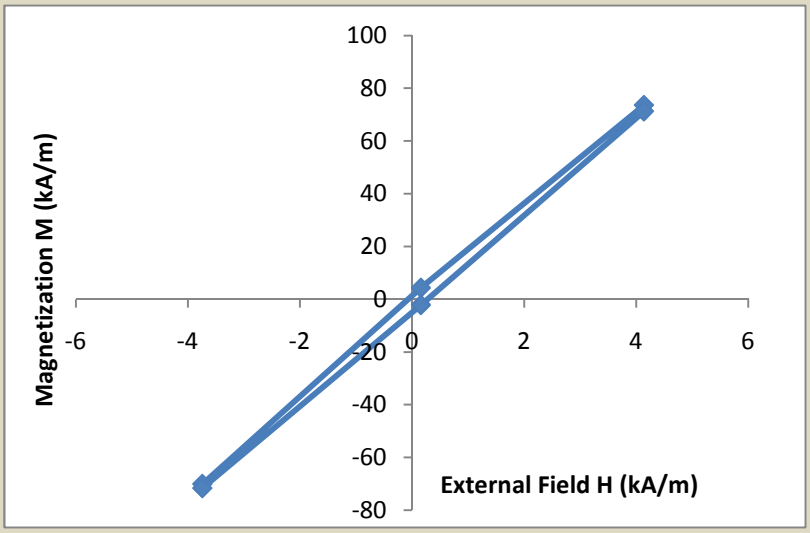

fluidMAG-UC/A: Uncoated Anionic

Figure 3.7. Hysteresis curves of MNP

A brief summary of the coercive field H_C, magnetization saturation M_S and the initial susceptibility are presented below in Table 3.1. The initial susceptibility is the slope of a linear portion of the hysteresis curve. The low H_C values suggest superparamagnetic behaviour for these particles.

Table 3.1. VSM measurements for chemicell GmbH MNP

Sample Name	*Sample Coating*	*Lot ID*	H_c (*Oe*)	M_s (*emu/g*)*	Initial Susceptibility M/H
fluidMAG-D	Starch	0104/09	1.517	55.867	9.921
fluidMAG-OS	Oleic Acid, Sodium Salt	0204/09	0.2.67	54.133	16.449
fluidMAG-PAD	Polyacrylamide	0504/09	0.882	64.172	15.810
fluidMAG-PMO	Poly(maleic acid-co-olefin)	0304/09	1.769	60.27	15.865
fluidMAG-PVA	Polyvinyl alcohol	0404/09	2.251	55.867	13.480
SiMAG-Carboxyl	Silica, non-porous	0604/09	0.5.33	55.147	14.762
fluidMAG-UC/A	Uncoated Anionic charge	0704/09	2.164	57.947	16.796
fluidMAG-UC/C	Uncoated Cationic charge	0804/09	1.667	61.920	18.185

* emu/ gram of dried ferrofluid sample

The chemical structure of each coating is provided by chemicell GmbH and depicted in Figure 3.8. As seen in this Figure, the length and the chemical components of each coating vary. It has been suggested that such variety affects magnetic properties of the MNP [60] and therefore has an impact on the thermal behaviour. This will be investigated in the following section.

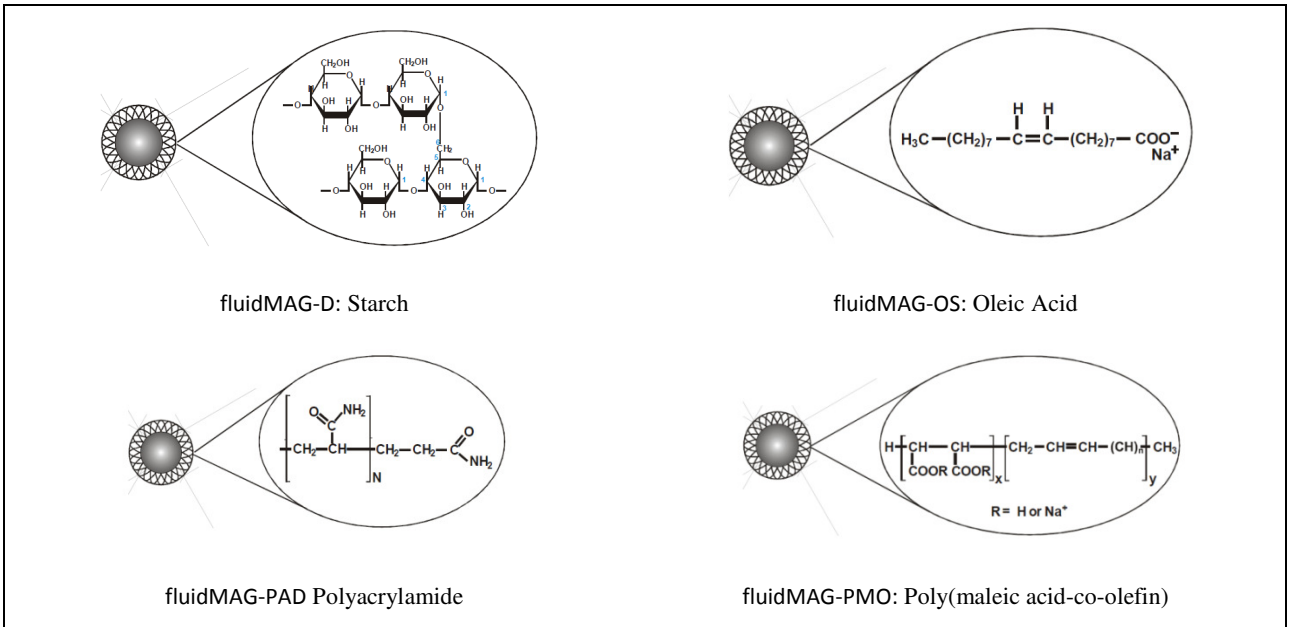

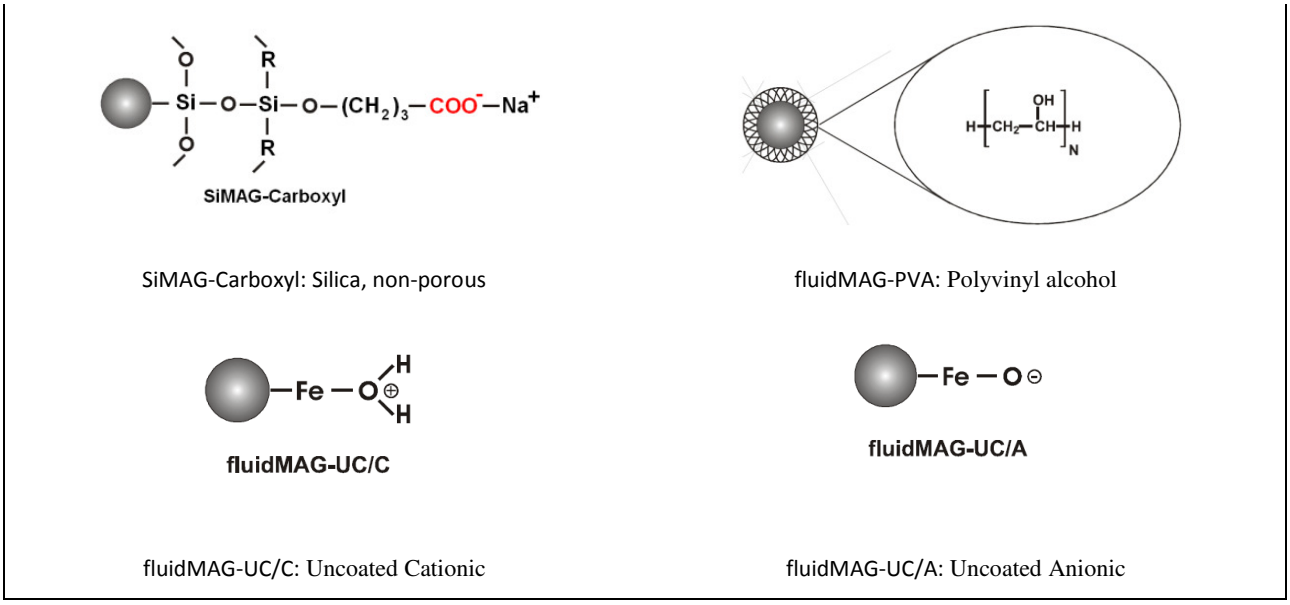

Figure 3.8. Chemical composition of MNP coatings [www.chemicell.com]

A third set of MNP were specially ordered and custom made by chemicell GmbH from fluidMAG-PMO-2 series (Lot ID: 2906/09). The company claimed that these particles have larger diameters than previously provided fluidMAG-PMO. Figure 3.9 shows the crystal diffraction pattern obtained from TEM and suggests magnetite Fe_3O_4 as chemical composition of these particles.

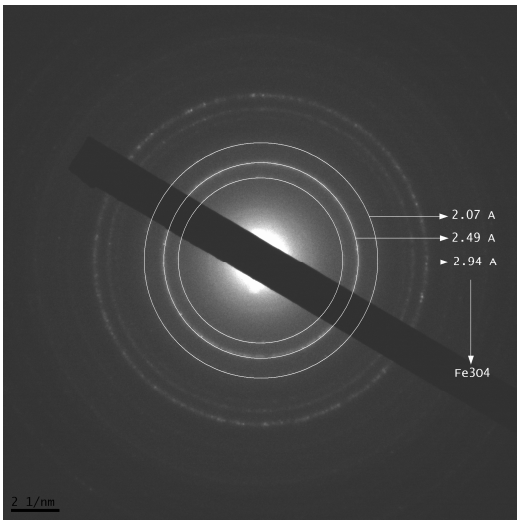

Figure 3.9. TEM image and diffraction patterns of fluidMAG-PMO-2

From the images of TEM, the diameters of more than 630 single particles were measured and recorded. The results are depicted in Figure 3.10 and show a relatively wide size distribution ranging approximately from 3 – 18 nm in diameter, peaking at 11 and 13 nm.

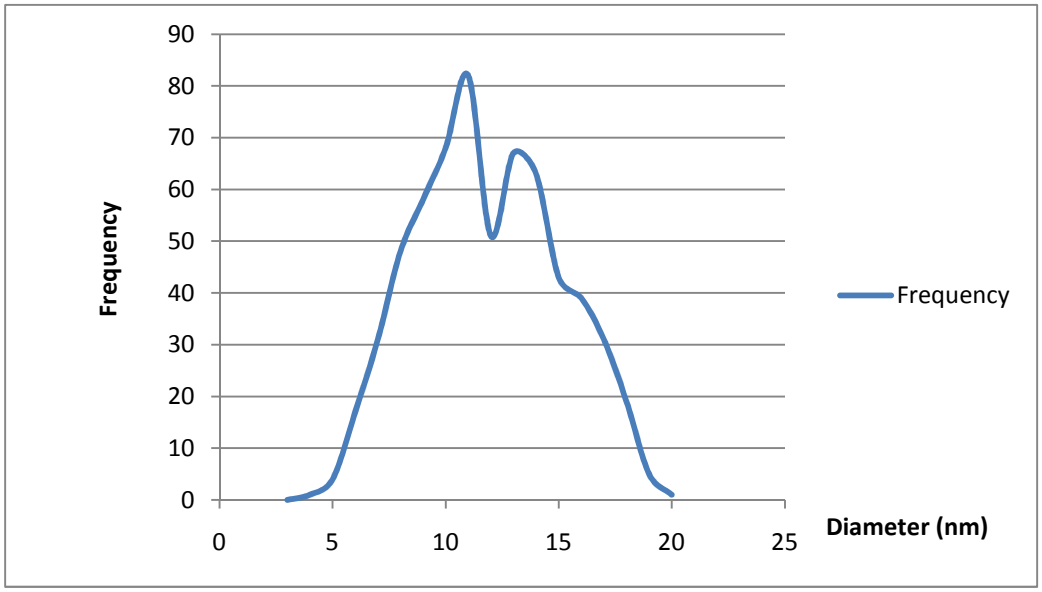

Figure 3.10. Size distribution of magnetite nanoparticles

The VSM measurement shown in Figure 3.11 suggests a value equal to 78.3 emu g^{-1} for M_s and 0.14 Oe for H_c. The low coercive field and lack of hysteresis represent the superparamagnetic nature of these nanoparticles.

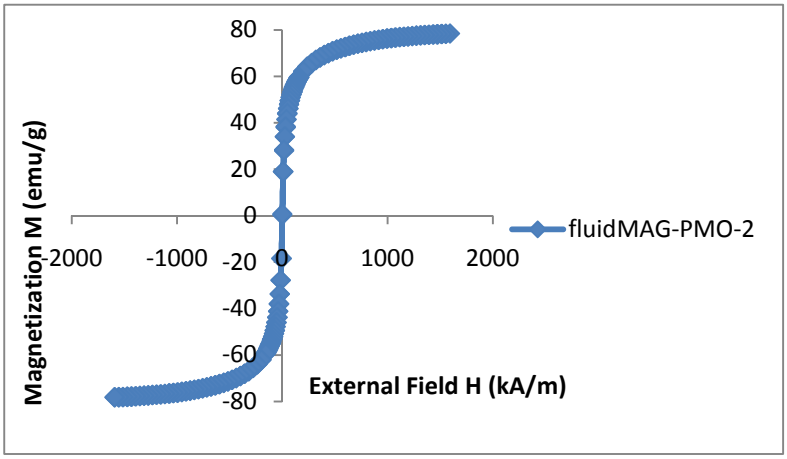

Figure 3.11. VSM for fluidMAG-PMO-2

3.2.2 Effect of Concentration on Heat Generation

The purchased superparamagnetic magnetite nanoparticles from micromod were divided into three concentration groups of 10, 25 and 50 mg magnetic particles (MNP plus the coating polymer) per ml of suspension fluid by means of distillation. Two 1ml samples of each concentration were collected in plastic containers (eppendorfs). Each eppendorf was placed in custom made isolation foam (Styrofoam) fitted for the inside of a 15 mm diameter, 8 turn copper tube induction coil. The 1.5 kW induction machine shown in Figure 3.1, provided a magnetic field near 80 kA m^{-1} (~1000 Oe) at a frequency of 150 kHz inside the coil. Temperature changes were monitored and recorded at every 15 seconds for a period of 900 seconds (15 minutes) by two thermocouples (T-Type, Omega HH506R). A thermocouple measured the temperature of the sample and the other measured the temperature of the Styrofoam as shown in Figure 3.12.

Figure 3.12. Experimental setup concentration effect on heat

Prior to any test, 1ml of deionised water was placed inside the coil to measure the effect of the AC magnetic field on the suspension media, the thermocouples, the eppendorf and the Styrofoam. Such effect was measured to be negligible for this experiment. The tests were carried out twice for each sample and the results are averaged and presented in Chapter 4.

3.2.3 Effect of MNP Coating on Heat Generation

In this experiment magnetite nanoparticles purchased from chemicell GmbH with eight different coatings were placed in a 2 kW induction heating machine shown in Figure 3.2. The primary purpose of this experiment was to see how various coatings would influence the temperature rise of the MNP. Considering that only a handful of coatings were examined and as seen in Figure 3.6 the core diameters of the MNP were not always consistent, the results were not entirely

conclusive. The idea here however, was to find what type of coating among available samples would allow for maximum generation of heat. Therefore, 0.5 ml MNP samples of the various coatings with a concentration of 25 mg/ml were prepared in separate eppendorfs. Each sample was placed in a custom made isolation foam (Styrofoam) fitted for an inside of the copper tube coil seen in Figure 3.2. This coil was designed to generate a magnetic field strength of 2 kA m^{-1} at 160 kHz. Fibre optic temperature sensors (Reflex, SN: T18 217A, Neoptix© Inc, QC, Canada) recorded temperatures of the sample as well as a distance of 1 and 2 centimetres away from the center of the eppendorf every 15 seconds for a total time of 3000 seconds. The results were also used to validate thermodynamic theory of the time dependent change of temperature as a function of distance presented in Section 2.2.6 and shown in Figure 2.13. A control sample containing deionised water was placed inside the coil to measure the effect of the AC magnetic field on the thermocouples, the eppendorf and the isolation foam. This effect was found to be negligible.

3.2.4 Magnetic Fluid and Heat Generation

Results from previous experiment led to the purchase of magnetite nanoparticles fluidMAG-PMO-2 (Lot ID: 2906/09). As described in Section 3.2.1, these particles were larger than the former fluidMAG-PMO (Lot ID: 0304/09). For this experiment, as shown in Figure 3.13 and Figure 3.14, 1ml sample of fluidMAG-PMO-2 with concentration of 25 mg/ml was placed in a Cryogenic vial.

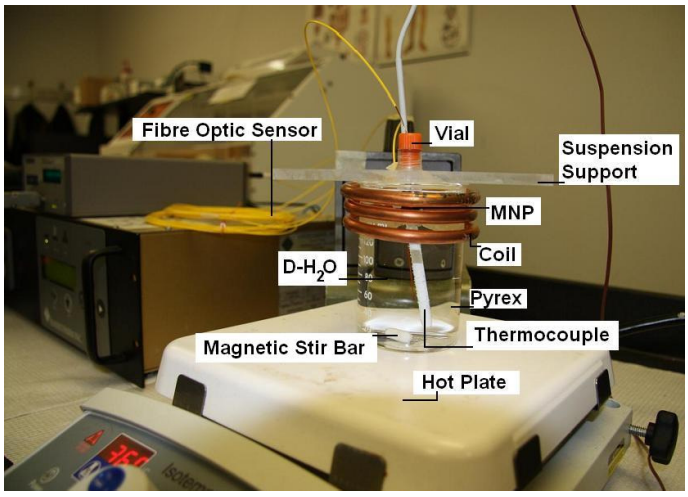

Figure 3.13. Heating of fluidMAG-PMO-2 on hot plate at 37ºC

The vial was then suspended in the middle of the copper coil and inside a Pyrex® beaker that contained 170 ml of deionised water via a plastic suspension support. The beaker was placed on a hot plate with a magnetic stirrer device (Isotemp®, Fisher Scientific, Iowa, USA) and the temperature was set to 37ºC to imitate the environment of a human body. Water temperature was kept constant at 37ºC via a thermocouple connected directly to the hot plate and was monitored continuously via a third party fibre optic sensor. To imitate a moderate blood flow, a small cylindrical magnetic stir bar 6 x 6 x 15 mm was dropped to the bottom of the beaker and set to spin at 50 rpm. This speed was artificially chosen to create constant flow.

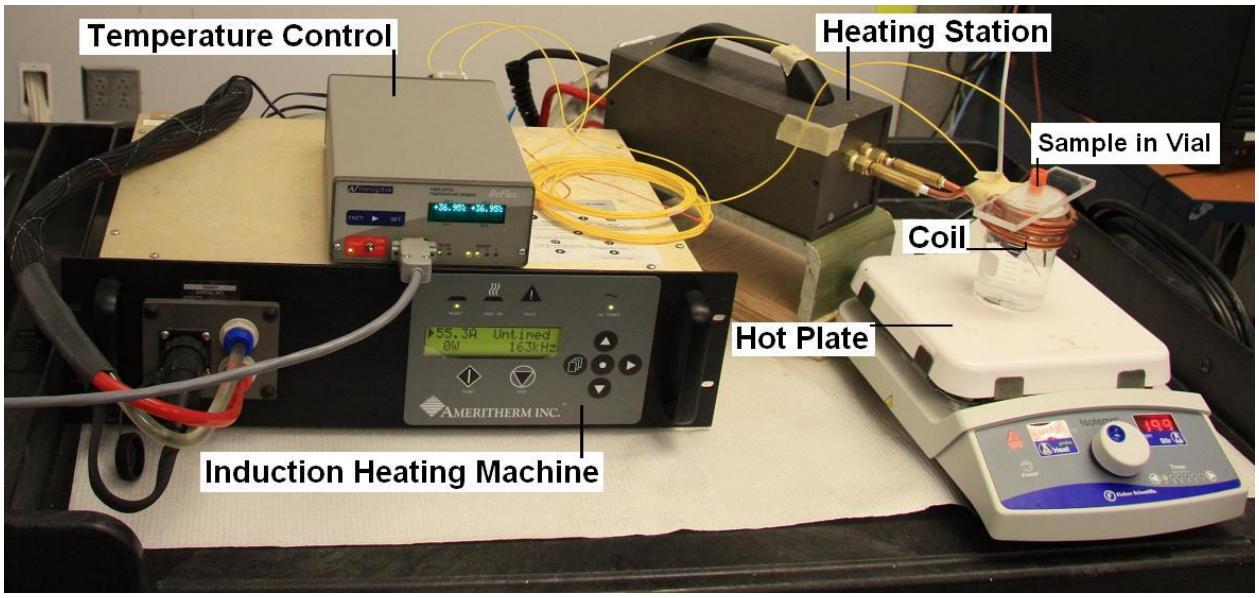

Figure 3.14. Induction heating setup for fluidMAG-PMO at 37 ºC

The coil was powered by an induction heating machine via a heat station and it was designed to generate a field equivalent to 4.5 kA m^{-1} at 160 kHz. This is in agreement with tissue limitations that can be seen in Figure 2.16. Room temperature and temperature of the sample were measured every 10 seconds for a period of 1080 seconds (18 minutes), with the help of fibre optic sensors (Reflex, SN: T18 217A, Neoptix© Inc, QC, Canada). A control sample containing deionised water was also placed inside the coil to measure the effect of the field on thermocouples, vial, plastic suspension support and the beaker. This effect was found to be negligible. The experiment was repeated 3 times and the results are explained in the following chapter.

3.2.5 Hydrogel Encapsulated MNP

For this experiment, temperature response of PPNIPA hydrogel embedded MNP (PPNIPA-MNP) inside an AC magnetic field was tested. To avoid a rapid dissipation of heat to the surrounding area, the test subjects were placed first in a 5% w/v agar gel, and second in a thermal insulation Styrofoam.

To create agar gel, 10 grams of agar powder (Agar, Technical) was added to 200 ml deionised water. The solution was stirred and heated to 80°C and then left to cool to room temperature for an hour. The final gel was cut to fit inside an induction coil seen in Figure 3.15. A hole was then made in the middle of the agar to fit the shape of the eppendorf. The PPNIPA-MNP samples were synthesized using a method described in [94]. Two sets of PNIPA-MNP samples were prepared from two concentrations of 5 and 10 mg magnetite/ml ferrofluids of dextran coated MNP purchased from micromod (Section 3.2.1). Samples were placed in the eppendorfs with 7.0 mm internal diameter and 40.3 mm in height. Each eppendorf contained 0.5 ml PNIPA-MNP. A set of PNIPA hydrogel without any MNP was also synthesised to see the effect of the AC magnetic field on the polymer alone. Eppendorfs were carefully placed in the center and inside of the agar gel so that the samples could be buried below the agar top surface. For this experiment the agar gel was put in the middle and inside a 3 turn custom made copper tube coil with a diameter of 67 mm. The coil was powered by an induction machine (Amertitherm Inc.™) shown in Figure 3.15 to generate a magnetic field of 9.2 kA m^{-1} (~116 Oe) at 145 kHz. The magnetic parameters fall below the $\boldsymbol{H_0} \times f$ limit range (4×10^9 A m^{-1} s^{-1}) suggested for treatments of the breast cancer and explained in Section 2.4.2.

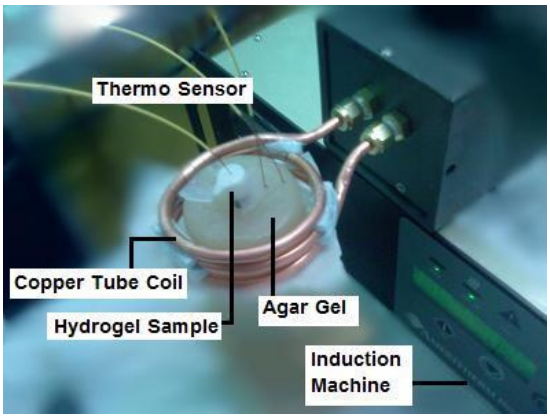

Figure 3.15. Induction of hydrogel sample in agar gel

Temperatures of the hydrogel samples and the agar gel at a distance of 1 centimetre away from the center of the eppendorf were recorded every 10 seconds by fibre optic temperature sensors (Reflex, SN: T18 217A, Neoptix Inc, QC, Canada). The induction machine was turned on 10 seconds after starting time for temperature recording and turned off after 30 minute for each sample.

In the second part of this experiment (Figure 3.16), Styrofoam was used. Styrofoam minimizes the effect of possible external temperature fluctuations due to coil or variation of room temperature by thermally insulating the sample. As such, each eppendorf was placed in the cylindrical Styrofoam with 27 mm in diameter and 45 mm in height such that the eppendorf was completely insulated by the Styrofoam. The Styrofoam was then placed at the center of the copper tube coil. Variations of temperature inside the eppendorf as well as the Styrofoam at a distance of 1 centimetre away from the center of the eppendorf were recorded every 10 seconds for 30 minutes via fibre optic temperature sensors.

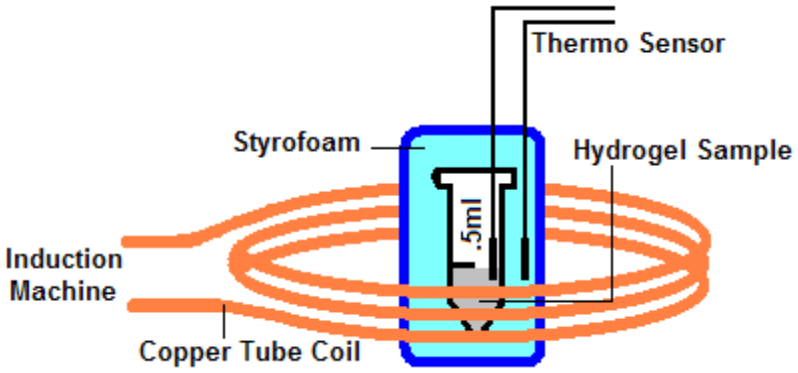

Figure 3.16. Schematics of the induction of the hydrogel sample in a Styrofoam insulation.

Finally, to visualize volume change of PNIPA hydrogel samples, a 20 mm^3 PNIPA hydrogel containing 10 mg magnetite/ml of PNIPA hydrogel with lower critical solution temperature (LCST) of near 29°C was placed inside a channel fabricated on Poly(methyl methacrylate) or PMMA and seen in Figure 3.17. The PNIPA hydrogel was then heated on a hot plate to 29°C. Temperature readings were taken by an infrared thermometer (Oakton, TempTestr IR) and change of volume was observed by a microscope. Results are provided in the next chapter.

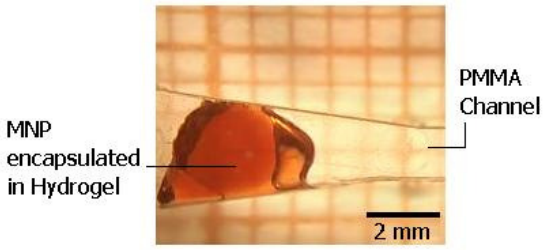

Figure 3.17. Hydrogel encapsulated MNP inside PMMA channel

3.2.6 Spherical Hydrogel Encapsulated MNP

The hydrogel encapsulated MNP (PNIPA-MNP) are synthesized using a method similar to the one described in [94]. For this experiment, as illustrated in Figure 3.18, the PNIPA-MNP are made into small spherical shapes of about 1 mm in diameter that contain 2 wt% magnetite nanoparticles. The fluidMAG-PMO-2 (Lot ID: 2906/09) are used as the MNP embedded within the hydrogels. Nearly 100 of these hydrogels were placed in a 2.0 ml Cryogenic vial. The vial was then filled with deionised water until the total volume was 0.5 ml. The vial was placed at the center of a Styrofoam fitted for inside of the copper coil similar to the one shown in Figure 3.15. The PNIPA-MNP were excited by an AC magnetic field strength of 4 kA m^{-1} at 160 kHz. The magnetic parameters respect physiological field limitations shown in Figure 2.16. Fibre optic temperature sensors (Reflex, SN: T18 217A, Neoptix© Inc, QC, Canada) were used to measure the temperature change for a period of 1500 seconds (25 minutes). The experiment was carried out 5 times and the results are discussed in the following chapter.

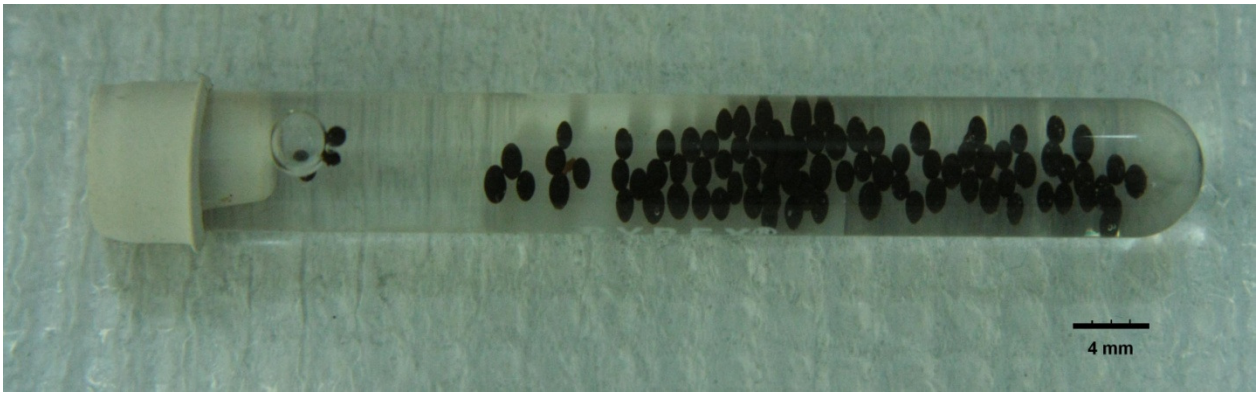

Figure 3.18. Spherical hydrogel encapsulated MNP

CHAPTER 4 RESULTS

4.1 Effect of Concentration on Heat Generation

As described in Section 3.2.2, three concentration groups of 10, 25 and 50 mg magnetic particles (MNP plus the coating polymer) were placed inside a coil providing a magnetic field of near 80 kA m^{-1} at a frequency of 150 kHz. Temperature increments as a function of time are depicted in Figure 4.1.

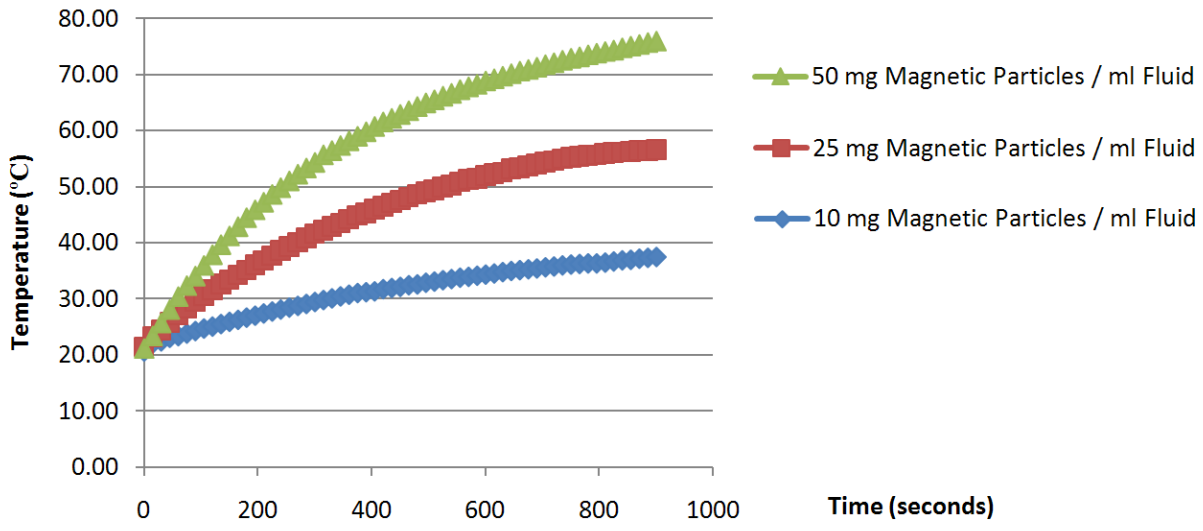

Figure 4.1. Concentration effect of MNP on temperature change

It was observed that for these concentration groups, under the condition where AC magnetic field parameters were constant, temperature rose more rapidly as concentration of MNP were increased. This was not far from the expectation. Each MNP is thought of as a heat source when placed inside the AC magnetic field. By increasing the concentration of MNP, the number of these heat sources in the sample is therefore increased and thus higher temperatures are obtained. Figure 4.1 shows that the temperature rises following a sub-linear trend initially, then after some time the thermal equilibrium between the sample and the surrounding area leads it to plateau. Such behaviour is seen in each curve. At every second, energy is absorbed due to the excitation of MNP by the AC magnetic field given in J s g^{-1}. As previously seen in Section 2.2.5, via Equation (2.6) SAR (W g^{-1} or J s g^{-1}) can be calculated by multiplying the temperature increment, which is experimentally derived from the linear regression of the initial data points $\frac{dT}{dt}$, to the

specific heat capacity of water, given by 4185 J kg^{-1} K at room temperature, and the mass of magnetite nanoparticles. Table 4.1 tabulates SAR estimated from the graph of the temperature rise as function of time (graphical SAR) using this method.

Table 4.1. SAR graphical measurement

Concentration: mg (Fe_3O_4 MNP +50% Coating) per ml Fluid	50	25	10
mass: mg magnetite per ml Fluid	25	12.5	5
$\frac{dT}{dt}$ *(°C/s)*	0.15	0.08	0.03
Ratio: $\frac{dT}{dt}$ [10 mg/ml] : $\frac{dT}{dt}$ [MNP]	5:1	2.7:1	1:1
SAR (W/g)	25.67	26.78	25.67

As seen in Table 4.1, $\frac{dT}{dt}$ is steeper for higher mass of magnetite per ml of the sample fluid. Theoretically, SAR value is independent of the concentration of the MNP and should be equal for all samples. The difference in SAR that is seen above however, could be explained by possible experimental errors due to unintentional small changes in the magnetic field or frequency as well as slight changes in the room temperature. The value of SAR obtained from this experiment is in good agreement with the theoretical predictions seen in Section 2.3.1.1 for particles in range of 7-10 nm in diameter under an AC magnetic field near 80 kA m^{-1} at 150 kHz. This is shown below in Figure 4.2.

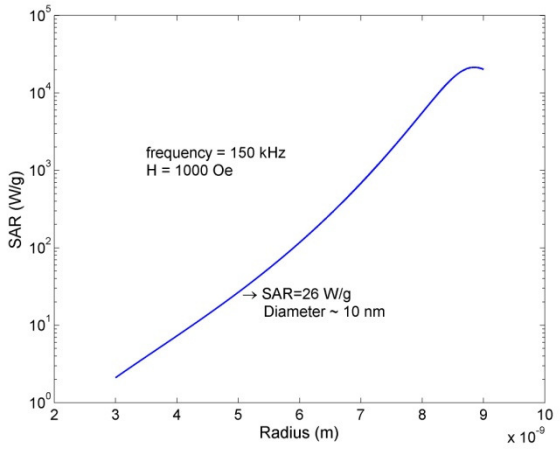

Figure 4.2. SAR due to Néel Relaxation vs. Radius of MNP

Using the graphical SAR shown in Table 4.1, ΔT can also be mathematically approximated for 1 ml spherical tissue volume with a radius R of 6.2 mm using the Equation (2.26) in Section 2.3.1.2. For this calculation, heat conductivity of the tissue λ is assumed 0.146 (W K^{-1} m^{-1}). The results are tabulated in Table 4.2.

Table 4.2. Theoretical and experimental estimations for ΔT

Concentration (coating + MNP) mg/ml	Concentration of magnetite mg/ml	Theoretical ΔT	Experimental ΔT
10	5	11.11	14.15
25	12.5	27.78	35.4
50	25	55.56	54.7

Theoretical and experimental ΔT seem to follow the same incrementing trend line and the values are in close agreement.

Temperature increments as a function of time for this experiment can also be normalized to fit second order polynomial equations plotted in Figure 4.3.

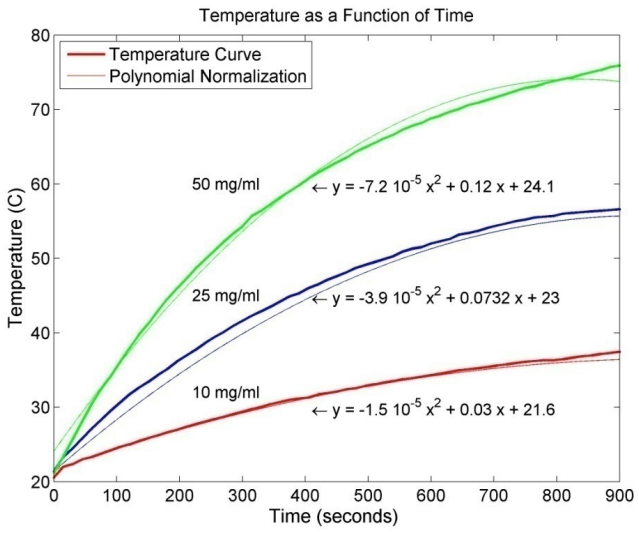

Figure 4.3. Second order polynomial normalization of magnetite

It is important to mention that the $\frac{dT}{dt}$ ratios given in Table 4.2 show a linear trend with the concentration of magnetite samples. This trend is seen again in normalized second order

polymers. In Table 4.3, the concentration ratio referenced at 10 mg of magnetite per ml seem to follow throughout the coefficients of the polynomial equations given in the form of $y = a\,x^2 + b\,x + c$, where a and b are the coefficients and c represents initial temperature of the sample respectively. The small difference may be due to the experimental errors discussed above.

Table 4.3. Second Order Polynomial Normalization of MNP

MNP Concentration	Ratio 10 mg/ml : [MNP]	Second Order Polynomial	x^2 a [10 mg/ml]: a [MNP]	x b [10 mg/ml]: b [MNP]
10	1:1	$y = -1.5 \times 10^{-5}\,x^2 + 0.03\,x + 21.6$	1:1	1:1
25	1:2.5	$y = -3.9 \times 10^{-5}\,x^2 + 0.0732\,x + 23$	1:2.6	1:2.4
50	1:5	$y = -7.2 \times 10^{-5}\,x^2 + 0.12\,x + 24.1$	1:4.8	1:4

In fact, the linear trend seen here may help formation of a systematic relationship between concentration of MNP and the final induced temperature for a given time interval. For instance, at 37ºC, under the same AC magnetic field parameters, the second order polynomial equation could be approximated as $y = -0.75 \times 10^{-5}\,x^2 + 0.015\,x + 37$ for 1ml sample of the same magnetite nanoparticles with a concentration of 5 mg/ml. Figure 4.4 shows that in 900 seconds, such approximated trace reaches 44.4ºC.

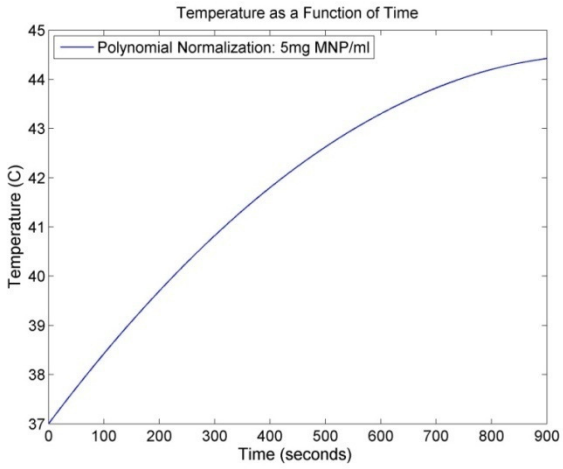

Figure 4.4. Simulation of temperature as a function of time for 5 mg magnetite /ml fluid

This is interesting because theoretically temperature falls in the range of temperatures well defined for moderate hyperthermia. However physiological limitations to the AC magnetic field parameters are not respected in this setup. These limitations are considered for the following experimental observations.

4.2 Effect of MNP Coating on Heat Generation

In this experiment, MNP with eight different coatings were excited by the AC magnetic field described in Section 3.2.3. Temperature increments as a function of time for all samples are depicted in Figure 4.5. Change in temperatures ΔT at distances of 1 and 2 centimetres away from the center of the eppendorf containing the magnetite nanoparticles were also recorded. These results are given in Table 4.4.

Table 4.4. Change in temperature at 0, 1 and 2 cm from the center of magnetite sample

Sample Name	ΔT @ 0 cm	ΔT @ 1 cm	ΔT @ 2 cm
fluidMAG-PVA	1.66	0.88	0.55
fluidMAG-D	2.09	1.45	0.83
SiMAG-Carboxyl	3.12	1.61	1.06
fluidMAG-OS	3.69	1.86	0.31
fluidMAG-PAD	3.72	1.47	0.88
fluidMAG-UC/A	4.43	1.86	1.00
fluidMAG-UC/C	5.92	2.95	1.56
fluidMAG-PMO	6.71	3.03	1.45

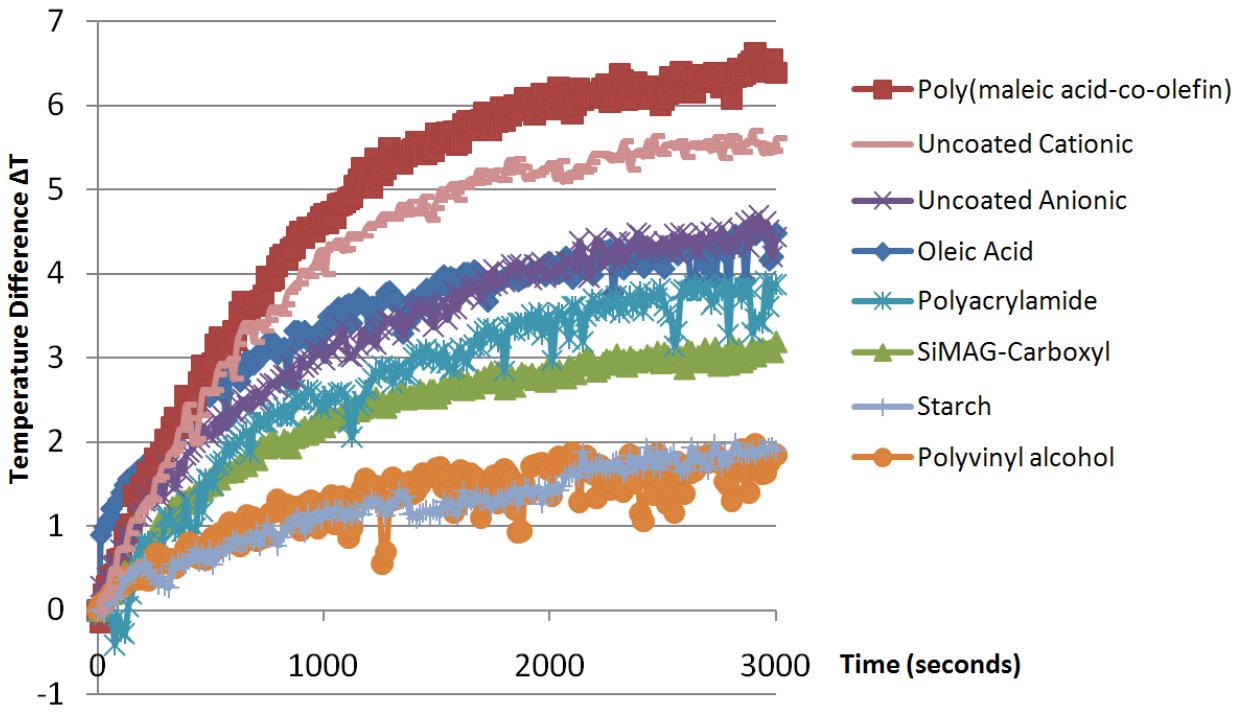

Figure 4.5. Effect of coating of magnetite on heat

As seen above, magnetite nanoparticles with Poly (maleic acid-co-olefin) coating showed highest thermal effect and magnetite nanoparticles with Polyvinyl alcohol coating presented the lowest effect. Theoretically speaking, MNP with higher magnetization saturation M_s and initial susceptibility χ_0 should produce more heat inside an AC magnetic field than MNP with lower values of M_s and χ_0. High susceptibility means that the magnetic moments within the MNP align faster with the field direction and reach M_s at lower applied external field. Assuming narrow MNP size distribution for all samples in this experiment, Table 3.1 of Section 3.2.1 suggests that magnetite nanoparticles with Polyacrylamide (PAD) coating should introduce highest ΔT. However, Figure 4.5 illustrates otherwise. To better understand this, the graphical SAR (W g^{-1}) for each sample is calculated and presented in Table 4.5. The area of the hysteresis loops for the external field amplitudes between -2 and 2 kA m^{-1} were also calculated and given in this table. From the hysteresis plots in Figure 3.7, magnetisation of the samples at an external field of 2 kA m^{-1} are also estimated and presented in Table 4.5.

Table 4.5. MNP Coating effect: results and theoretical calculation

Name	fluidMAG-D	fluidMAG-OS	fluidMAG-PAD	fluidMAG-PMO	fluidMAG-PVA	SiMAG-Carboxyl	fluidMAG-UC/A	fluidMAG-UC/C
Coating Polymer	Starch	Oleic Acid, Sodium Salt	Polyacrylamide	Poly(maleic acid-co-olefin)	Polyvinyl alcohol	Silica, non-porous	Uncoated Anionic charge	Uncoated Cationic charge
Magnetisation M @ H=2 kA/m (emu/g)	3.4993	5.9203	5.715	5.7469	4.7825	5.1956	6.5126	5.9409
Susceptibility	9.921	16.449	15.810	15.865	13.480	14.762	16.796	18.185
Temperature (°C) @ t=0 s	23.68	23.98	24.77	24.40	24.66	24.58	24.61	24.51
Temperature (°C) @ t=3000 s	25.77	27.68	28.49	31.11	26.32	27.70	29.04	30.43
$\Delta T = (T_{t=3000} - T_{t=0})$	2.09	3.70	3.72	6.71	1.66	3.12	4.43	5.92
Area of Hysteresis loop $(A/m)^2 \times 10^4$	929.41	198.72	716.76	2000.60	1779.50	316.64	2289.30	1750.84
Hysteresis SAR (W/g)	0.3608	0.0771	0.2782	0.7765	0.6907	0.1229	0.8886	0.6796
Graphical SAR (W/g)	0.335	0.670	0.763	1.228	0.290	0.558	0.893	1.150
Δ SAR	-0.026	0.593	0.484	0.451	-0.401	0.435	-0.063	0.470
% Hysteresis	108	11	36	63	*	22	107	59
% Relaxation	0	89	64	37	*	78	0	41

The close area within the hysteresis loop (A m^{-1})^2 is placed in the Equation (2.14) to calculate SAR (W g^{-1}) due to hysteresis losses. For this calculation, frequency was 160 kHz and the AC magnetic field amplitude was 2 kA m^{-1}. In the above table, Δ SAR represents the difference between SAR due to the hysteresis losses and the graphical SAR found from Figure 4.5.

Assuming that loss mechanisms are due to hysteresis for those particles that exhibit hysteresis losses shown in Figure 3.7, and/or relaxation losses for those lacking hysteresis in the that figure, the contribution of each mechanism to the thermal outcome can be estimated by comparing the graphical losses to the calculated hysteresis losses. Needless to say, that hysteresis curve is different when measured in a DC field than in the AC field. This suggests that the different values of SAR due to graphical estimations and hysteresis curves can indeed be related to the frequency of the magnetic field. For example, as see in Table 4.5, magnetite nanoparticles with starch coating (fluidMAG-D) produce a ΔT of 2.09 ºC that could have been originated entirely from the area of its hysteresis curve. Uncoated anionic charged magnetite nanoparticles (fluidMAG-UC/A) follow the same pattern, only in this case the area of the hysteresis loop is larger than that of the fluidMAG-D nanoparticles and therefore ΔT is larger.

In the case of oleic acid coated magnetite nanoparticles (fluidMAG-OS), relaxation losses contribute nearly 90% of the graphical SAR. Alternatively, uncoated anionic charge magnetite nanoparticles (fluidMAG-UC/A) cover nearly 100% of the graphical SAR by hysteresis losses. It appears that for samples that hysteresis losses contribute to at least 50% of the graphical SAR, ΔT is at its maximum. This is seen specifically for fluidMAG-UC/C (ΔT = 5.92 ºC) and fluidMAG-PMO (ΔT = 6.71 ºC) nanoparticles. This indicates that relaxation and hysteresis losses work hand to hand and one complements the other.

It is also interesting to see that polyvinyl alcohol coated magnetite nanoparticles showed the lowest ΔT. This may be surprising since the area within the hysteresis loop for this sample is among the highest and relatively similar to that of the uncoated cationic charge magnetite nanoparticles. A possible explanation may rest in the TEM image provided in Figure 3.6e. In this figure, magnetite nanoparticles are surrounded by nearly 5 nm thick polyvinyl alcohol coating. This thick layer is not seen in any other images from the TEM. This protective coating may be acting as a thermal isolator and prevent thermal conduction.

To validate thermodynamic theory presented in Section 2.2.6, it was assumed that all samples were contained within a spherical volume of 0.5 ml. Using Equations (2.25a) and (2.25b), theoretical estimation of dissipation of heat from the spherical MNP sample through the Styrofoam is plotted in Figure 4.6. The constants required to plot these graphs are given in Table 4.6. Experimental data points at distances of 0, 1 and 2 centimetres away from the center of the spherical volume given in Table 4.4 are also shown in Figure 4.6 in red solid triangles.

Table 4.6. Constants for the plot of time and distance dependent thermal equations

Particle mass (g)	12.5×10^{-3}
Sample volume (m^3)	0.5×10^{-6}
Radius of the spherical volume (m)	4.924×10^{-3}
Power ($W\ m^{-3}$)	$\frac{\text{SAR} \times \text{Particle mass}}{\text{Sample volume}}$
Heat conductivity of magnetite ($W\ K^{-1}\ m^{-1}$)	0.778
Heat conductivity of Styrofoam ($W\ K^{-1}\ m^{-1}$)	0.033
Density of magnetite ($g\ m^{-3}$)	1.23×10^{6}
Density of Styrofoam ($g\ m^{-3}$)	100×10^{3}
Heat capacity of magnetite ($J\ g^{-1}\ K^{-1}$)	2.54
Heat capacity of Styrofoam ($J\ g^{-1}\ K^{-1}$)	1.3

For the plots seen below in Figure 4.6, it is assumed that heat did not escape from the top part of the eppendorf where temperature sensors were connected. It is also assumed that heat is entirely and uniformly transferred to the surrounding Styrofoam, and room temperature does not vary. These graphs are plotted without considering the air pockets within the Styrofoam. Last but not least, the heat resistance between MNP, water, the plastic wall of the eppendorf and Styrofoam are assumed to be negligible.

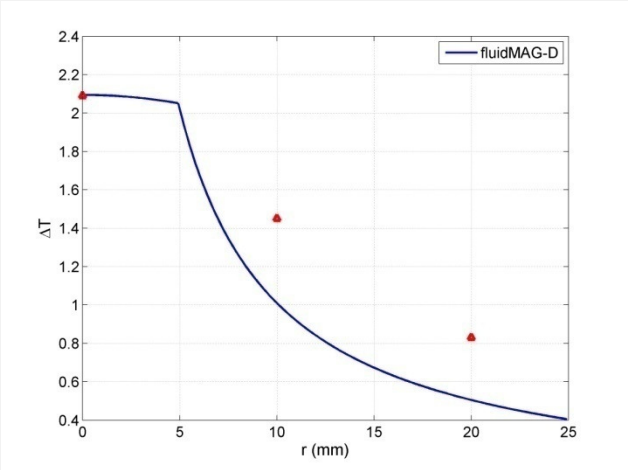

fluidMAG-D: Starch

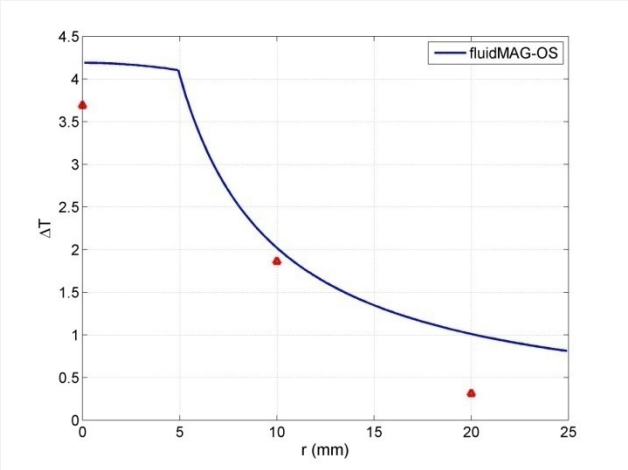

fluidMAG-OS: Oleic Acid

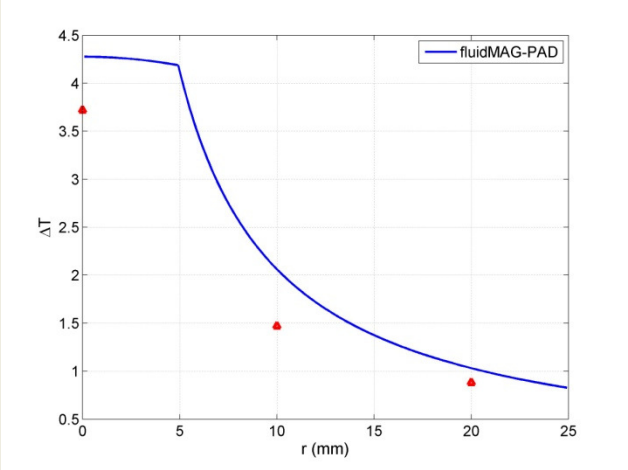

fluidMAG-PAD Polyacrylamide

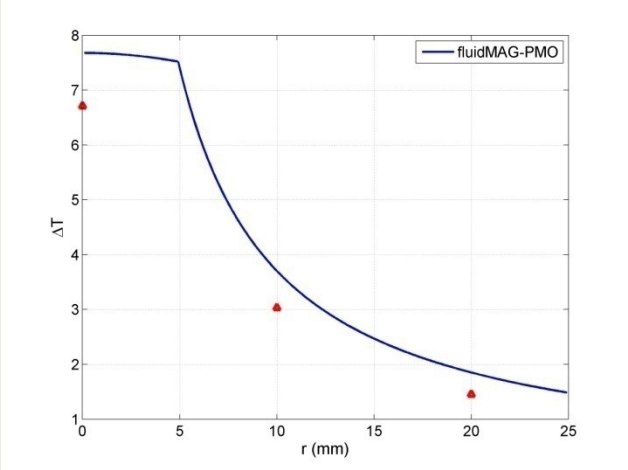

fluidMAG-PMO: Poly(maleic acid-co-olefin)

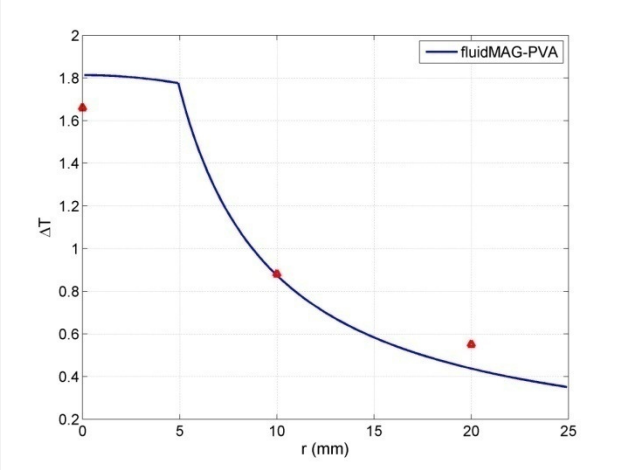

fluidMAG-PVA: Polyvinyl alcohol

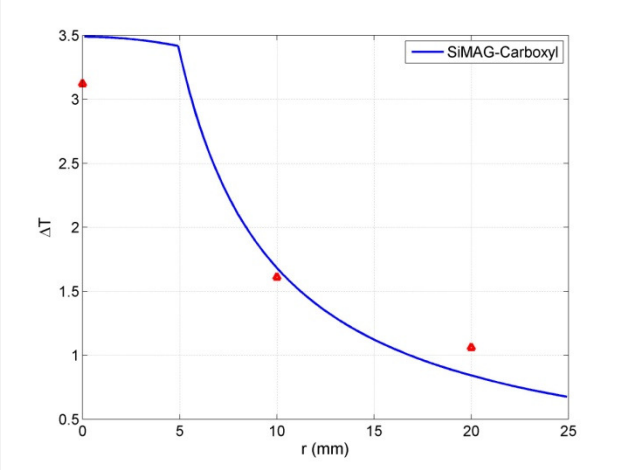

SiMAG-Carboxyl: Silica, non-porous

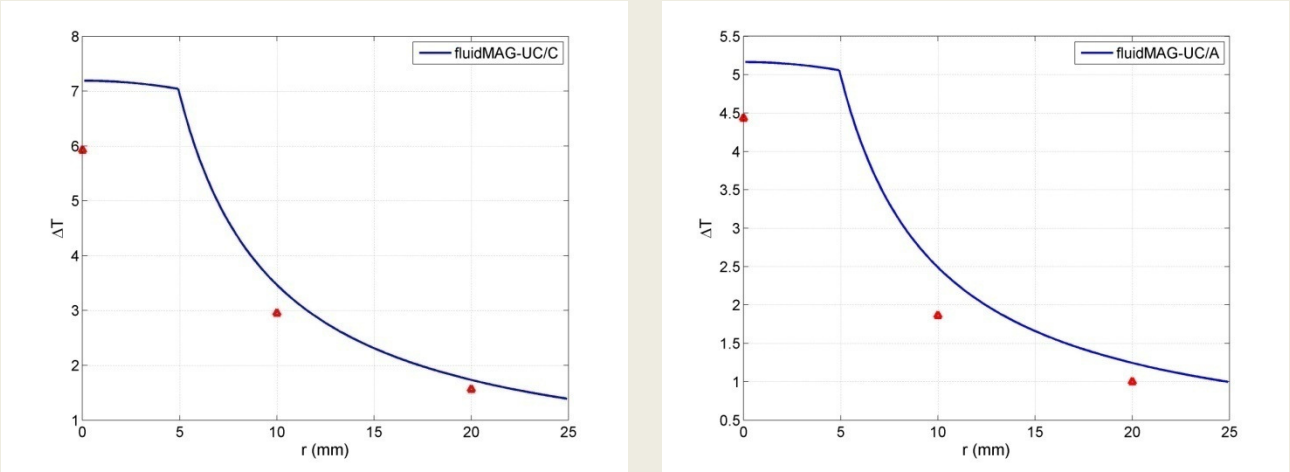

fluidMAG-UC/C: Uncoated Cationic

fluidMAG-UC/A: Uncoated Anionic

Figure 4.6. Theoretical estimation of time and distance dependent thermal effect versus experimental

Despite of the assumptions and the experimental errors such as sudden variation of the room temperature, the experimental data was not very far from the theoretical estimations. It is apparent that these points would be closer to their corresponding estimated values in a better temperature controlled environment with a better knowledge of the magnetic properties of the MNP.

4.3 Magnetic Fluid and Heat Generation

Poly (maleic acid-co-olefin) coated magnetite nanoparticles used in this experiment are larger than those used in the previous experiment. This experiment was set up to examine the thermal behaviour of these particles inside a temperature elevated environment such as inside of a human body. Temperature increments as a function of time for this experiment are depicted in Figure 4.7.

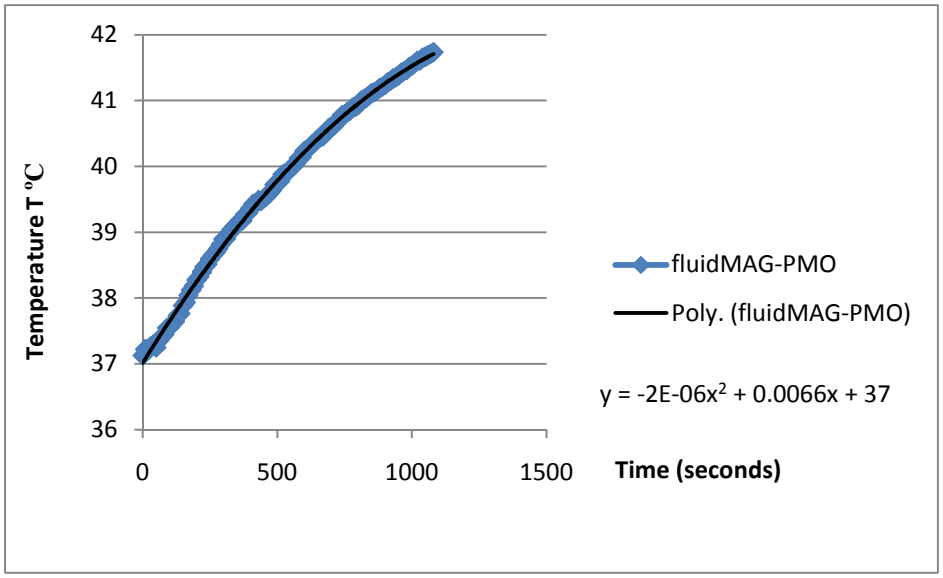

Figure 4.7. Poly (maleic acid-co-olefin) coated magnetite nanoparticles at 37ºC environment

The above Figure leads to a graphical SAR (W g^{-1}) value of 0.967 W g^{-1}. This value falls in the expected theoretical SAR value shown in Figure 4.8 for magnetite nanoparticles of 3 – 18 nm in diameter (see Figure 3.10) in an AC magnetic field of 4.5 kA m^{-1} at 160 kHz. This value is measured to be lower than the previously calculated value of the graphical SAR for Poly (maleic acid-co-olefin) coated magnetite nanoparticles given in Table 4.5. The reason for that may lie within the complex thermodynamic processes that have affected the dissipation of heat to the surrounding areas. For instance, the stirring of the water at 37ºC yielded a constant motion of the medium surrounding the outer surface of the vial. Therefore stirring have indeed cooled down some of the heat by thermal convection before it could be detected by the temperature sensors.

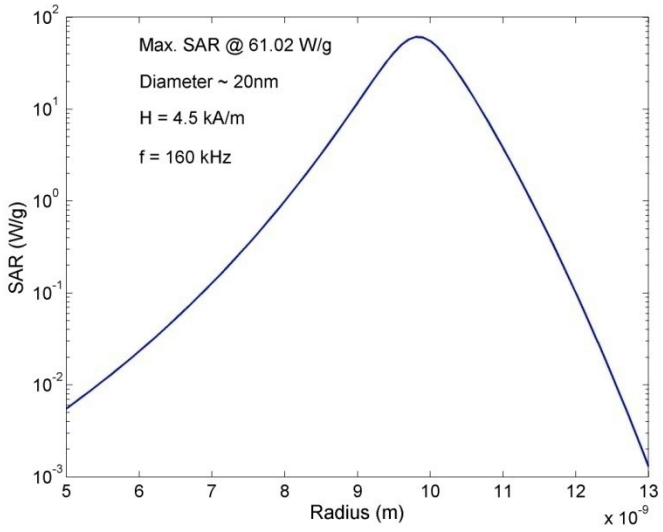

Figure 4.8. Theoretical SAR versus particle size

In this experiment it was shown that in 18 minutes, 25 mg/ml Poly (maleic acid-co-olefin) coated magnetite nanoparticles in a slowly moving fluid could raise body temperature from 37ºC to near 42ºC. As described in Section 1.2, such elevation of temperature is considered best for moderate hyperthermia. Using the method described in Section 4.1.1, the elevation of temperature can be mathematically traced with a second order polynomial equation similar to the one shown in Figure 4.2. Therefore, by modifying the coefficients of this equation, it is possible to simulate thermal behaviour for various concentrations of the same magnetite nanoparticles. This is presented below in Table 4.7 and plotted in Figure 4.9 for a time period equal to 1680 seconds (= 28 minutes).

Table 4.7. Mathematical simulation of concentration effect on thermal behavour of fluidMAG-PMO-2

Concentration (mg/ml) [FluidMAG-PMO-2]	$y = ax^2 + bx + c$			Temperature ºC @ t = 1680 (s)
	a	b	c	
25	-2E-06	0.0066	37	42.44
27.5 (10% increase)	-2.2E-06	0.0073	37	42.99
32.5 (30% increase)	-2.6E-06	0.0086	37	44.08

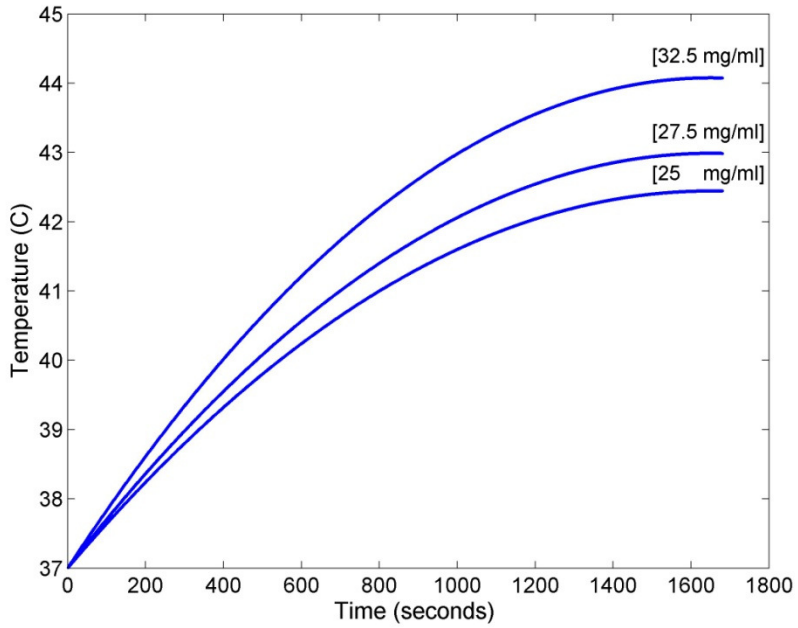

Figure 4.9. Mathematical simulation of concentration effect on thermal behavour of fluidMAG-PMO-2

Therefore 30% increase in the concentration of these MNP, at the present experimental setup, would lead to a temperature change over 44ºC in about 30 minutes.

4.4 Hydrogel Encapsulated MNP

As described in Section 2.4, thermo-sensitive hydrogels called PNIPA are able to reduce their volume by releasing water molecules once they are heated above their lower critical solution temperature (LCST). PNIPA hydrogel encapsulated MNP (PNIPA-MNP) are able to reach their LCST once they are placed inside an AC magnetic field. Therefore, PNIPA-MNP embedded drugs can be seen as actuators in hyperthermic drug release mechanism. In this experiment, LCST was by default at 29ºC. This value can be adjusted chemically at the time of PNIPA synthesis.

Results in agar gel and Styrofoam are tabulated in Tables 4.9 and 4.10 respectively.

Table 4.8. Temperature changes for samples inside agar gel

AGAR	T 1 (°C) t = 0 s	T 2 (°C) t = 1800 s	ΔT T2-T1
PNIPA Hydrogel	17.1	18.5	1.4
Surrounding (1 cm away)	17.1	18.8	1.7
5 mg magnetite/ml PNIPA	18.1	21	2.9
Surrounding (1 cm away)	17.8	20	2.2
10 mg magnetite/ml PNIPA	18.5	21.8	3.3
Surrounding (1 cm away)	18.3	20.9	2.6

Table 4.9. Temperature changes for samples inside Styrofoam insulation

STYROFOAM	T 1 (°C) t = 0 s	T 2 (°C) t = 1800 s	*ΔT* T2-T1
PNIPA Hydrogel	25.6	25.8	0.2
Surrounding (1 cm away)	25.8	26.2	0.4
5 mg magnetite/ml PNIPA	25.6	27.7	2.1
Surrounding (1 cm away)	25.6	27.1	1.5
10 mg magnetite/ml PNIPA	24.7	29.1	4.4
Surrounding (1 cm away)	25.3	27.8	2.5

Previously in 4.1.1, it was observed that higher concentration of MNP led to higher temperatures. As expected, 10 mg of magnetite per 1 ml of PNIPA hydrogel led to a higher ΔT than 5 mg of

magnetite per 1 ml of PNIPA hydrogel. As seen in Table 9, the temperature of the agar gel was always a few degrees Celsius below the room temperature (23°C). This may be due to constant liquid evaporation of the agar material at room temperature causing it to be colder.

The above Tables show that in Styrofoam, the AC magnetic field had little effect on PNIPA hydrogel samples with no embedded MNP, whereas inside the agar gel, this effect was seen as elevation of the temperature by 1.4°C. Table 9 also shows that temperature of the agar gel (surrounding 1 cm away), while PNIPA hydrogel samples with no embedded MNP were undergone the AC magnetic field, measured to be 1.7°C. Here, eddy currents generated in the agar gel by the induction coil may be responsible for elevations of temperature. The heat may then travel to the center of the agar gel and PNIPA hydrogel sample by conduction and raises its temperature. A more detailed view of the results for the agar gel and Styrofoam are shown in Figure 4.10 and Figure 4.11 respectively.

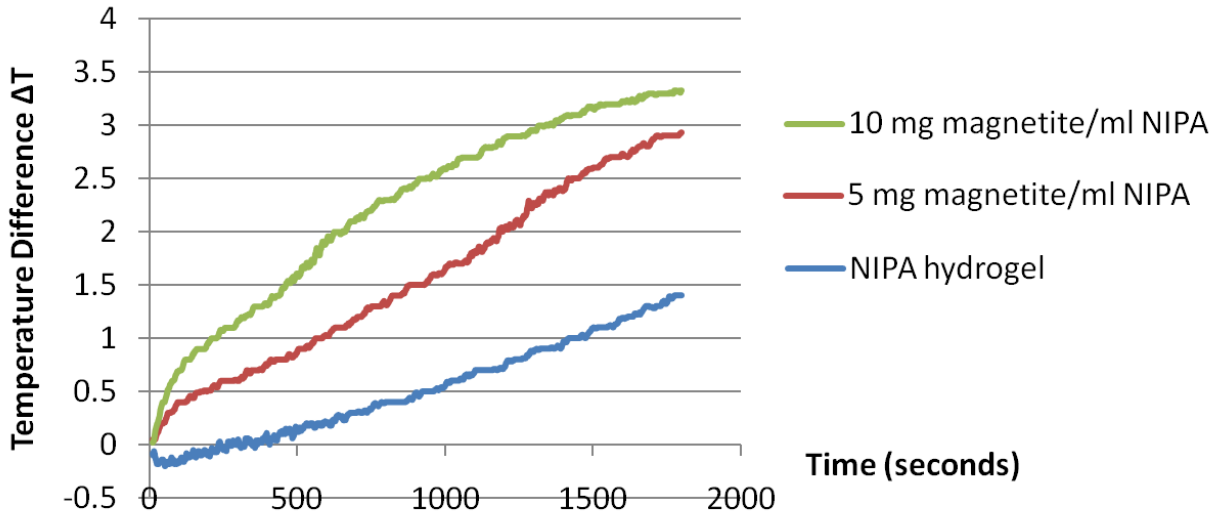

Figure 4.10. Temperature change versus time for samples inside agar gel

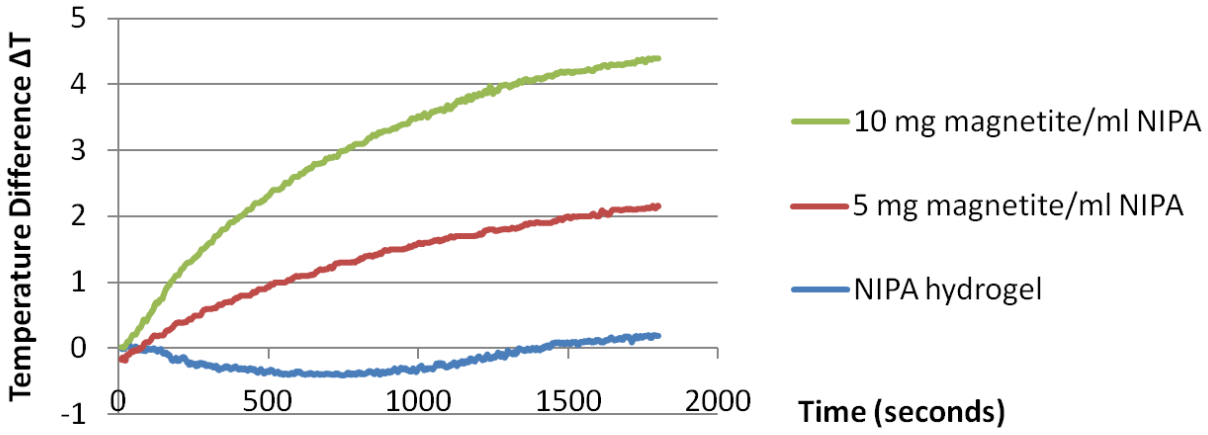

Figure 4.11. Temperature change versus time for samples inside Styrofoam

Once elevation of temperature for the PNIPA-MNP samples was confirmed to be due the presence of MNP, change in volume of PNIPA-MNP was tested. At 29ºC, a remarkable change of volume in the 10 mg magnetite/ml PNIPA-MNP sample at was observed. For these samples the dark red color of PNIPA-MNP (Figure 4.12a) turned grey (Figure 4.12d) and the volume decreased substantially to less than 12 mm^3 (60% reduction of volume). While cooling, the sample regained most of its original volume and was ready to be re-heated.

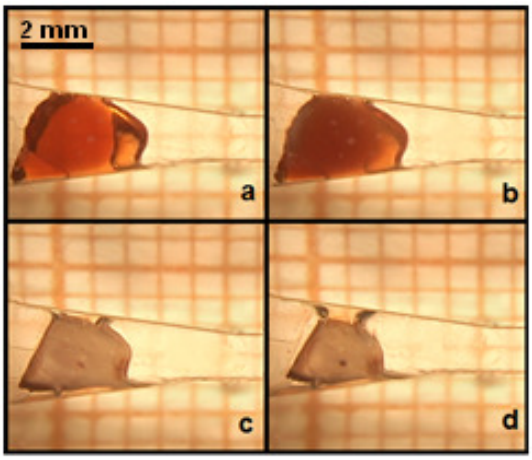

Figure 4.12. 60% Volume reduction (a-d) of 20 mm^3 PNIPA-MNP to less than 12 mm^3 when heated to 29°C

From results of this experiment it may be concluded that the PNIPA-MNP are indeed excellent candidates as hyperthermic drug release actuators. These particles could enter the blood stream

and locally release drug molecules when heated by an AC magnetic field. They are also able to prevent tumour from receiving nutrition supplies by means of embolization. The cooperation between MNP, AC magnetic field and thermo-sensitive hydrogels opens new doors to tumour therapy.

4.5 Spherical Hydrogel Encapsulated MNP

In this experiment, spherical PNIPA-MNP were heated by induction of an AC magnetic field with parameters in accordance with the physiological limitations shown in Figure 2.16.

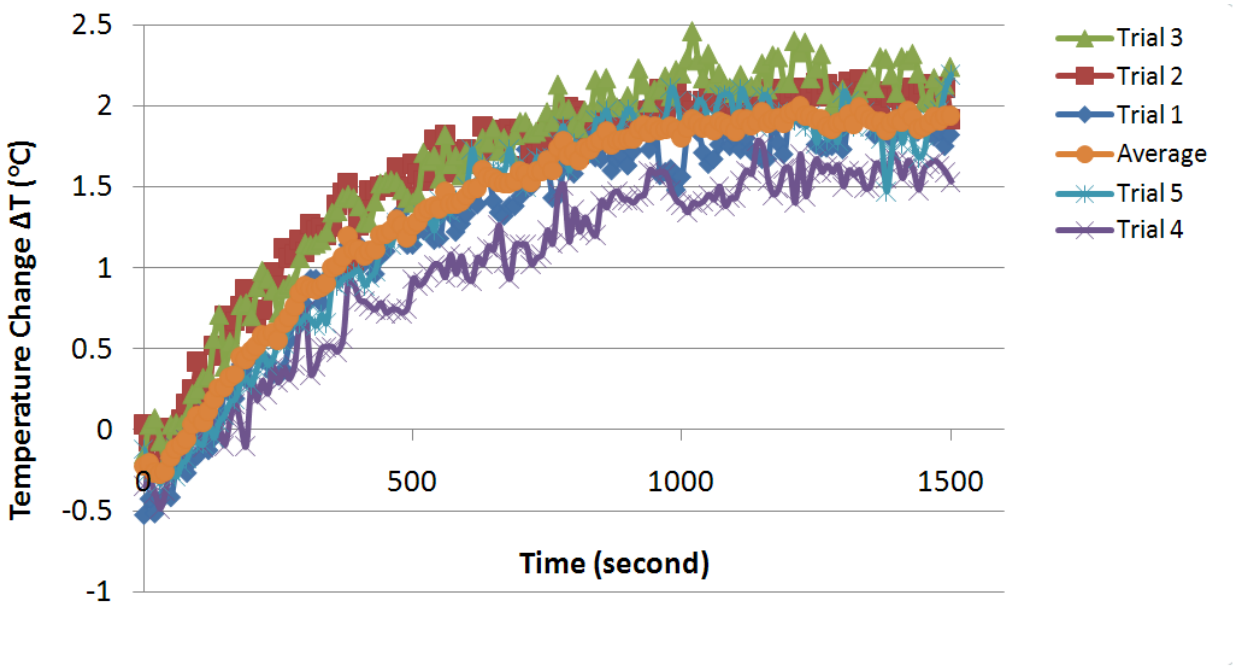

Figure 4.13. 2 wt% hydrogel encapsulated magnetire excited by an AC magnetic field

As seen in Figure 4.13, the average temperature change ΔT was approximately 2°C in 1500 seconds. Assuming that the LCST of spherical PNIPA-MNP drug carrying hydrogel is at 39°C, the AC magnetic field is able to provide sufficient heat to actuate a drug release sequence anywhere inside the human body. This is a step closer to the vision seen in Figure 2.21 in which PNIPA-MNP spheres are used for targeted release of therapeutic agents upon exposure to inductive heating by AC magnetic field.

CHAPTER 5 DISCUSSION

The motivation behind this thesis was to realize an actuation method for a miniaturised robotic system. Such robots navigate in the vascular network to a target tissue such as a tumour and actuate therapeutic sequence by heat and/or drug release. In the miniaturization of robots navigable inside human body, it is very important to reduce the number of components. This reduction can be achieved by increasing the functionality of each component to its maximum. A micro-carrier in the human body requires propulsion, tracking and actuation.

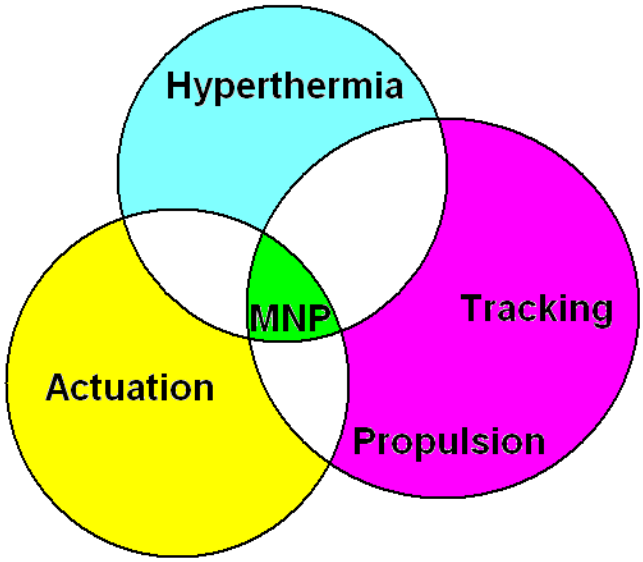

Figure 5.1. MNP as navigable and traceable hyperthermic actuator

The spatial variation (gradient) of the magnetic field is able to apply a force on a magnetic material and steer it through the vascular network. According to the Equation 2.25, this magnetic force is not dependent on the size of the magnetic material but rather on its volume. Therefore, an agglomeration of MNP can also be propelled using the same method. In addition to steering, MNP can distort the local magnetic field of an MRI and alter the relaxation times of the water protons in the surrounding water molecules and therefore produce a negative MR contrast agent [45]. Finally, hyperthermia of MNP inside an AC magnetic field can be used as an actuation mechanism and provide a synergistic thermal affect combined with chemo and radiation cancer therapies. As an important component of miniaturised robot systems, MNP possess increased functionality since they allow propulsion, tracking and actuation as shown in Figure 5.1.

Previously in our lab, a 1.5 mm ferromagnetic bead was propelled by the gradient field of a clinical MRI [93]. The bead was also tracked through distortions of the image of the MRI [93]. In this thesis, hyperthermia of MNP under AC magnetic field as an actuation mechanism for the proposed miniaturised robots was investigated. In contrast to other hyperthermia methods, hyperthermia via MNP in an AC magnetic field provides advanced control and can be highly localized. The experimental results given in Section 4.1, 4.2 and 4.3 and the theoretical explanation in Section 2.3 illustrate that by varying the concentration, the coating, the size and chemical composition of MNP, thermal behaviour of the particles can be controlled. It was observed that temperature rose more rapidly as concentrations of MNP were increased. Also, among several types of MNP thermal release was highest when relaxation mechanism and hysteresis losses coexisted. Although hysteresis losses were not theoretically expected from superparamagnetic nanoparticles, it is suspected that the coating thickness had an influence on the width of the hysteresis loops. To validate such conclusion however, further investigations beyond the scope of this project are required. For all experiments, it is reasonable to assume uniformity of the AC magnetic field due to the small size distribution of the MNP compared to the coil dimensions. Also, the samples were positioned in the middle of the field where the field is most uniform. Therefore, the variation of the magnetic field is expected to be minimal.

Thermo sensitive gels called hydrogels were examined in Section 4.4 as potential carriers for the next generation of targeted drug delivery. These carriers are able to shrink and release their contained liquid with therapeutic agents upon elevation of temperature. Such elevation of temperature can be obtained from hyperthermia of the encapsulated MNP within the hydrogels by an AC magnetic field. Due to some biocompatibility uncertainties to MNP as well as lack of space in miniaturised robots, there are limitations to concentration of MNP. However via experiments such as these, for a given target temperature to trigger the release of drugs integrated in the micro-carriers, one can predict what concentration of MNP is needed and the time required for that temperature to be reached. This further emphasises the candidacy of hyperthermia of MNP as an actuation mechanism for the realized robotic systems. The advantage of using MNP is that we can adjust the parameters such as the diameter, concentration, coating and the magnetic properties such as magnetization saturation.

As seen in Figure 4.8, SAR reaches a maximum value of 61.02 W g^{-1} for 20 nm poly (maleic acid-co-olefin) coated magnetite nanoparticles inside an AC magnetic field of 4.5 kA m^{-1} at 160

kHz. Suppose that these nanoparticles are embedded within drug containing micro-carriers of 50 µm in diameter and are immobilized in a target volume of 30 mm in diameter by means of embolization. To propel the micro-carriers through small veins by the gradient field of the MRI, an agglomeration of magnetite nanoparticles occupies 40% of the volume of the micro-carrier. Water, hydrogel polymer chains and therapeutic agents count for the remaining 60%. Figure 5.2 demonstrates this hypothetical situation.

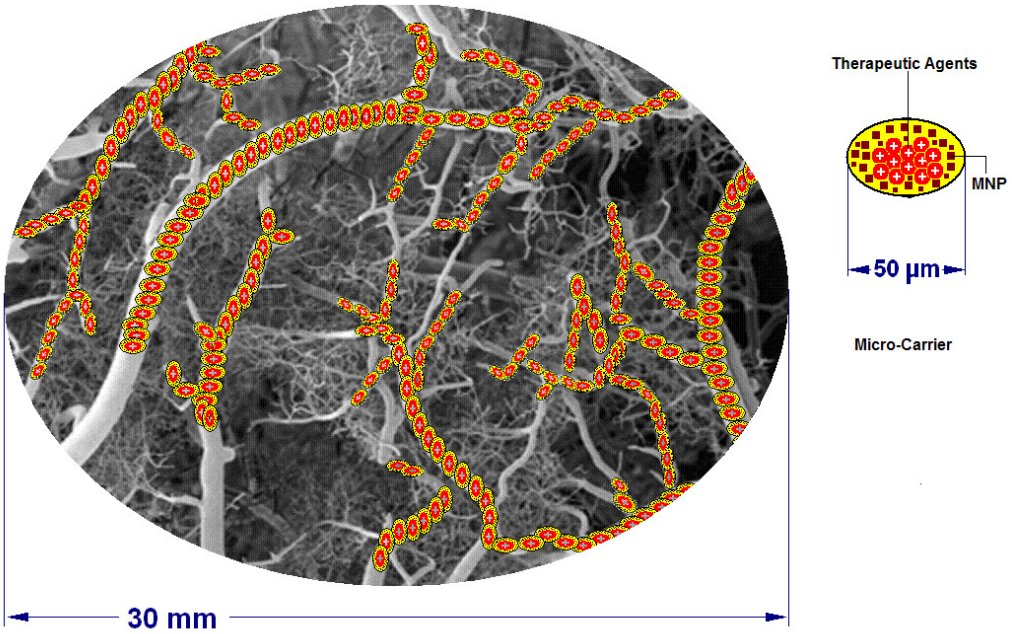

Figure 5.2. Embolization of micro-carriers in the target area

A computer simulation predicts that after 700 seconds, temperature at the center of the target area that contains 110,000 of the proposed micro-carriers would elevate by 3 degrees. Such elevation of temperature is sufficient for an actuation sequence to release the therapeutic agents within the micro-carriers. After 800 more seconds, the elevation of temperature would be nearly 5 degrees which is enough for moderate hyperthermia of the target area. A graphical presentation of this simulation is shown in Figure 5.3 (parameters are given in Appendix A.6). As seen in this figure, the elevation of temperature decays rapidly as the distance from the center of the target area increases. This means that in a hyperthermia application, unnecessary heat can be kept away from healthy surrounding tissue.

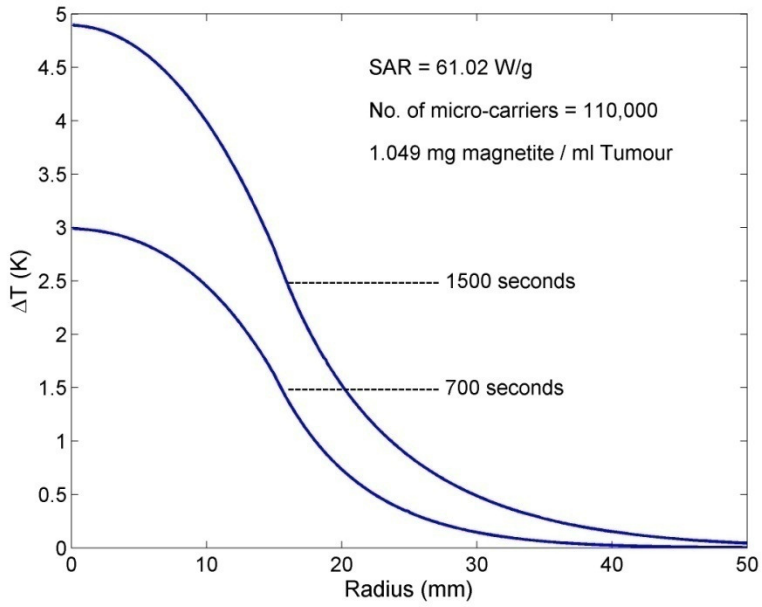

Figure 5.3. Time dependent temperature increase as function of distance

With the current technology and findings of our investigations, hydrogel encapsulated MNP with embedded therapeutic agents are proposed as navigable micro-carriers inside human body. The micro-carriers rely on the gradient field of the MRI to be propelled in the vascular network. They are also tracked by the distortions they create on the local magnetic field of the MRI. Once they have reached the target tissue, hyperthermia of embedded MNP in the AC magnetic field actuates a release of the therapeutic agents. By further advancing in MRI imaging, synthesis of hydrogel encapsulated MNP, enhancement of the gradient magnetic field of MRI and propulsion techniques and functionalising MNP size, coating and magnetic properties, the anticipated robots can be traced and navigated in smaller blood vessels and deliver drugs and produce thermal targeted therapy.

5.1 Disadvantages

Heating is generated by an AC magnetic field whose frequency and strength are limited by the physiological human body response to high frequency magnetic fields. These responses are stimulations of peripheral and skeletal muscles, possible cardiac stimulation and arrhythmia and non-specific inductive heating of tissue. Development of relatively high frequency magnetic field for clinical purposes is an extremely complicated task. Hyperthermia requires a precise

delivery of well controlled thermal dose into a complex biological system that is equipped with its own thermoregulatory system. Also, toxicity of the particles needs to be carefully studied so there would be no toxic residue accumulation in the body after thermal treatment.

The AC magnetic field does not contribute to the thermal effect of the MNP close to the local magnetic field of a clinical MRI. This is because the AC magnetic field is negligible when vector sum of the MRI field magnitudes higher than 1 Tesla and the AC field amplitude of a few miliTesla are combined. Therefore, after micro-carriers have reached the desired target tissue by the gradient of the magnetic field of an MRI, the patient has to be displaced far from the MRI field where AC magnetic field could be effective.

CONCLUSION

This *evaluation* started with a brief introduction to cancer, hyperthermia and several methods of hyperthermia as well as advantages of MNP and AC magnetic field. These advantages are not limited to heat, tracking and propulsion capabilities of MNP. MNP can be functionalized to target specific biological entities by means of antibody coatings and their colloidal ability. Also, biological and industrial limitations that lead to a set of magnetic parameters for MNP hyperthermia were explained. The effect of the concentration and various coatings of MNP were experimentally evaluated on elevation of temperature. Spherical hydrogel encapsulated MNP (MNP-PNIPA) were synthesised and heated with induction of an AC magnetic field with parameters within the physiological limitations. Propulsion of an agglomeration of MNP by the gradient magnetic field of an MRI was previously investigated in our lab. Also, the agglomeration of MNP was also tracked by the MR imaging process. Therefore, MNP-PNIPA drug carrying hydrogels can also be propelled by the MRI gradient magnetic field to a desired target location and be tracked by the MR imaging process. The AC magnetic field is able to provide sufficient heat to the embedded MNP to reduce the volume of the hydrogels and actuate a local drug release sequence. This is a step closer to hyperthermic targeted release of therapeutic agents upon exposure of MNP to inductive heating by AC magnetic field.

REFERENCE

[1] G. Karp, *Cell and Molecular Biology: Concepts and Experiemnts*, 4th ed. NJ: John Wiley, 2005.

[2] A. C. Society. (2007, *Cancer Facts & Figures*. Available: www.cancer.gov

[3] R. L. Horner MJ, Krapcho M, Neyman N, Aminou R, Howlader N, Altekruse SF, Feuer EJ, Huang L, Mariotto A, Miller BA, Lewis DR, Eisner MP, Stinchcomb DG, Edwards BK, "SEER Cancer Statistics Review, 1975-2006," *National Cancer Institute, Bethesda, MD,* 2009.

[4] W. E. N. Y. M.-H. Prentice, *Arnheim's Principles of Athletic Training: a Competency-Based Approach*. Boston, MA: McGraw-Hill, 2006.

[5] R. Cavaliere*, et al.*, "Selective heat sensitivity of cancer cells. Biochemical and clinical studies," *Cancer,* vol. 20, pp. 1351-1381, 1967.

[6] B. Hildebrandt*, et al.*, "The cellular and molecular basis of hyperthermia," *Critical Reviews in Oncology/Hematology,* vol. 43, pp. 33-56, 2002.

[7] J. Overgaard, "The current and potential role of hyperthermia in radiotherapy," *Int J Radiat Oncol Biol Phys,* vol. 16, Mar, pp. 535-549, 1989.

[8] RL. Anderson and D. Kapp, "Hyperthermia in cancer therapy: current status," *Med J Aust.,* vol. 152, p. 310, 1990.

[9] R. Engelhardt, "Hyperthermia and drugs," *Recent Results Cancer Res.,* vol. 104, pp. 136-203, 1987.

[10] P. Wust*, et al.*, "Hyperthermia in combined treatment of cancer," *The Lancet Oncology,* vol. 3, pp. 487-497, 2002.

[11] K. L. Ang*, et al.*, "Magnetic PNIPA hydrogels for hyperthermia applications in cancer therapy," *Materials Science and Engineering: C,* vol. 27, pp. 347-351, April 2007.

[12] A. Dieing*, et al.*, "The effect of induced hyperthermia on the immune system," in *Progress in Brain Research*. vol. Volume 162, ed: Elsevier, 2007, pp. 137-152.

[13] S. Purushotham*, et al.*, "Thermoresponsive core-shell magnetic nanoparticles for combined modalities of cancer therapy," *Nanotechnology,* vol. 20, 2009.

[14] J. Zhang and R. D. K. Misra, "Magnetic drug-targeting carrier encapsulated with thermosensitive smart polymer: Core-shell nanoparticle carrier and drug release response," *Acta Biomaterialia,* vol. 3, pp. 838-850, 2007.

[15] S. A. Meenach*, et al.*, "Poly(ethylene glycol)-based magnetic hydrogel nanocomposites for hyperthermia cancer therapy," *Acta Biomaterialia,* vol. In Press, Uncorrected Proof.

[16] R. T. Pettigrew*, et al.*, "Clinical Effects Of Whole-Body Hyperthermia In Advanced Malignancy," *The British Medical Journal,* vol. 4, pp. 679-682, 1974.

[17] P. Jiegang*, et al.*, "A Novel Whole-Body Perfusion System for Hyperthermia in Oncology," in *Bioinformatics and Biomedical Engineering, 2007. ICBBE 2007. The 1st International Conference on*, 2007, pp. 1080-1083.

[18] E. A. S. Clare M. C. Tempany, Nathan McDannold, Bradley J. Quade, Ferenc A. Jolesz, Kullervo Hynynen, "MR Imaging–guided Focused Ultrasound Surgery of Uterine Leiomyomas: A Feasibility Study," ed: Radiology, Vol 226, 2003.

[19] W. G. Bradley Jr, "MR-Guided Focused Ultrasound: A Potentially Disruptive Technology," *Journal of the American College of Radiology,* vol. 6, pp. 510-513, 2009.

[20] C. J. Diederich and K. Hynynen, "Ultrasound technology for hyperthermia," *Ultrasound in Medicine & Biology,* vol. 25, pp. 871-887, 1999.

[21] A. Y. Cheung, "Microwave and radiofrequency techniques for clinical hyperthermia," *British Journal of Cancer Suppl.,* vol. 5 Mar, pp. 16-24, 1982.

[22] Y. Tange*, et al.*, "Heating Characteristics of a RF Hyperthermia for Deep-Seated Regions," in *Engineering in Medicine and Biology Society, 2005. IEEE-EMBS 2005. 27th Annual International Conference of the*, 2005, pp. 6770-6776.

[23] T. S. H. Takahashi, H. Motoyama, T. Uzuka, S. Takahashi, K. Morita, K. Kakinuma, R. Tanaka, "Radiofrequency interstitial hyperthermia of malignant brain tumors: development of heating system," *Experimental Oncology,* vol. 22, pp. 186-190, April 20, 2000 2000.

[24] G. Carrafiello*, et al.*, "Microwave tumors ablation: Principles, clinical applications and review of preliminary experiences," *International Journal of Surgery,* vol. 6, pp. S65-S69, 2008.

[25] S. Banik*, et al.*, "Bioeffects of microwave--a brief review," *Bioresource Technology,* vol. 87, pp. 155-159, 2003.

[26] M. M. Paulides*, et al.*, "Electromagnetic Head-And-Neck Hyperthermia Applicator: Experimental Phantom Verification and FDTD Model," *International Journal of Radiation Oncology Biology Physics,* vol. 68, pp. 612-620, 2007.

[27] K. Engin, "Biological rationale and clinical experience with hyperthermia," *Controlled Clinical Trials,* vol. 17, pp. 316-342, 1996.

[28] P. R. Stauffer, "Evolving technology for thermal therapy of cancer," *International Journal of Hyperthermia,* vol. 21, pp. 731 - 744, 2005.

[29] J. C. Lantis Ii*, et al.*, "Microwave applications in clinical medicine," *Surgical Endoscopy,* vol. 12, pp. 170-176, 1998.

[30] O. A. Arabe*, et al.*, "A 400 MHz Hyperthermia System using Rotating Spiral Antennas for Uniform Treatment of Large Superficial and Sub-Surface Tumors," in *Microwave Symposium, 2007. IEEE/MTT-S International*, 2007, pp. 1333-1336.

[31] M. Urano and E. Douple, *Hyperthermia and oncology: Interstitial hyperthermia: physics, biology and clinical aspects* vol. 3, page 1. Tokyo Japan, 1992.

[32] A. S. Wright*, et al.*, "Radiofrequency versus Microwave Ablation in a Hepatic Porcine Model," *Radiology,* vol. 236, pp. 132-139, July 1, 2005 2005.

[33] Byeong-Ho Park*, et al.*, "The Induction of Hyperthermia in Rabbit Liver by means of duplex Stainless Steel Thermoseeds," *Korean Journal of Radiology,* vol. 3, pp. 98-104, 2002.

[34] H. Iida, *et al.*, "Synthesis of Fe3O4 nanoparticles with various sizes and magnetic properties by controlled hydrolysis," *Journal of Colloid and Interface Science,* vol. 314, pp. 274-280, 2007.

[35] Q. Pankhurst, "Nanomagnetic medical sensors and treatment methodologies," *BT Technology Journal,* vol. 24, pp. 33-38, 2006.

[36] T. Neuberger, *et al.*, "Superparamagnetic nanoparticles for biomedical applications: Possibilities and limitations of a new drug delivery system," *Journal of Magnetism and Magnetic Materials,* vol. 293, pp. 483-496, 2005.

[37] C. C. Berry and A. S. G. Curtis, "Functionalisation of magnetic nanoparticles for applications in biomedicine," *Journal of Physics D: Applied Physics,* vol. 36, pp. 198-206, 2003.

[38] Ste´phane Mornet, *et al.*, "Magnetic nanoparticle design for medical diagnosis and therapy," *Materials Chemistry,* vol. 14, pp. 2161-2175, Jul 21 2004.

[39] S. Martel, *et al.*, "Fundamental design rules for the conception of microdevices to be propelled in the blood circulatory system through magnetic gradients generated by a clinical MRI system," in *Microtechnology in Medicine and Biology, 2005. 3rd IEEE/EMBS Special Topic Conference on*, 2005, pp. 253-256.

[40] A. Jordan, *et al.*, "Magnetic fluid hyperthermia (MFH)," in *Proceedings of an international conference on Scientific and Clinical Applications of Magnetic Carriers*, U. Hafeli, *et al.*, Eds., ed. Rostock, Germany: Plenum Press, New York, 1997.

[41] O. V. Melnikov, *et al.*, "Ag-doped manganite nanoparticles: New materials for temperature-controlled medical hyperthermia," *Journal of Biomedical Materials Research Part A,* vol. 91A, pp. 1048-1055, 2009.

[42] F. Bertsch, *et al.*, "Non-invasive temperature mapping using MRI: comparison of two methods based on chemical shift and T1-relaxation," *Magnetic Resonance Imaging,* vol. 16, pp. 393-403, 1998.

[43] T. Pradell, *et al.*, "Technology of Islamic lustre," *Journal of Cultural Heritage,* vol. 9, pp. e123-e128, 2008.

[44] M. C. Roco, "Nanotechnology: convergence with modern biology and medicine," *Current Opinion in Biotechnology,* vol. 14, pp. 337-346, 2003.

[45] M. Corti, *et al.*, "Magnetic properties of novel superparamagnetic MRI contrast agents based on colloidal nanocrystals," *Journal of Magnetism and Magnetic Materials,* vol. 320, pp. e320-e323, 2008.

[46] E. S. Kawasaki and A. Player, "Nanotechnology, nanomedicine, and the development of new, effective therapies for cancer," *Nanomedicine: Nanotechnology, Biology and Medicine,* vol. 1, pp. 101-109, 2005.

[47] S. K. Sahoo, *et al.*, "The present and future of nanotechnology in human health care," *Nanomedicine: Nanotechnology, Biology and Medicine,* vol. 3, pp. 20-31, 2007.

[48] L. T. Terry B Huff, Yan Zhao, Matthew N Hansen, Ji-Xin Cheng, Alexander Wei, "Hyperthermic effects of gold nanorods on tumor cells," *nanomedicine,* vol. 2 (1), pp. 125-132, 2007.

[49] A. Wijaya*, et al.*, "Magnetic field heating study of Fe-doped Au nanoparticles," *Journal of Magnetism and Magnetic Materials,* vol. 309, pp. 15-19, 2007.

[50] D. P. O'Neal*, et al.*, "Photo-thermal tumor ablation in mice using near infrared-absorbing nanoparticles," *Cancer Letters,* vol. 209, pp. 171-176, 2004.

[51] S. N. Kale*, et al.*, "Cerium doping and stoichiometry control for biomedical use of La0.7Sr0.3MnO3 nanoparticles: microwave absorption and cytotoxicity study," *Nanomedicine: Nanotechnology, Biology and Medicine,* vol. 2, pp. 217-221, 2006.

[52] W. H. Suh*, et al.*, "Nanotechnology, nanotoxicology, and neuroscience," *Progress in Neurobiology,* vol. 87, pp. 133-170, 2009.

[53] Gilchrist R. K.*, et al.*, "Selective Inductive Heating of Lymph Nodes," *Annals of Surgery,* vol. 146, pp. 596-606, 1957.

[54] M. Zeisberger*, et al.*, "Metallic cobalt nanoparticles for heating applications," *Journal of Magnetism and Magnetic Materials,* vol. 311, pp. 224-227, 2007.

[55] D.-H. Kim*, et al.*, "Heat generation of aqueously dispersed CoFe2O4 nanoparticles as heating agents for magnetically activated drug delivery and hyperthermia," *Journal of Magnetism and Magnetic Materials,* vol. 320, pp. 2390-2396, 2008.

[56] J. Chatterjee*, et al.*, "Synthesis and characterization of polymer encapsulated Cu-Ni magnetic nanoparticles for hyperthermia applications," *Journal of Magnetism and Magnetic Materials,* vol. 293, pp. 303-309, 2005.

[57] T. N. Brusentsova*, et al.*, "Synthesis and investigation of magnetic properties of Gd-substituted Mn-Zn ferrite nanoparticles as a potential low-TC agent for magnetic fluid hyperthermia," *Journal of Magnetism and Magnetic Materials,* vol. 293, pp. 298-302, 2005.

[58] Q.-s. Tang*, et al.*, "Using thermal energy produced by irradiation of Mn-Zn ferrite magnetic nanoparticles (MZF-NPs) for heat-inducible gene expression," *Biomaterials,* vol. 29, pp. 2673-2679, 2008.

[59] B. D. Cullity and C. D. Graham, *Introduction to magnetic materials*. New York: Addison-Wesley, 1972.

[60] L. A. Harris, "Polymer Stabilized Magnetite Nanoparticles and Poly(propylene oxide) Modified Styrene-Dimethacrylate Networks," DOCTOR of PHILOSOPHY, CHEMISTRY, Virginia Polytechnic Institute and State University, Blacksburg, Virginia, 2002.

[61] D. Jiles, *Introduction to magnetism and magnetic materials*, 1st ed. New York: Chapman and Hall, 1990.

[62] E. Duguet*, et al.*, "Towards a versatile platform based on magnetic nanoparticles for in vivo applications," *Bulletin of Materials Science,* vol. 29, pp. 581-6, 2006.

[63] C.-R. Lin*, et al.*, "Magnetic properties of monodisperse iron oxide nanoparticles," in *50th Annual Conference on Magnetism and Magnetic Materials*, San Jose, California (USA), 2006, pp. 08N710-3.

[64] E. C. Stoner and E. P. Wohlfarth, "A mechanism of magnetic hysteresis in heterogeneous alloys," *Magnetics, IEEE Transactions on,* vol. 27, pp. 3475-3518, 1991.

[65] Mi Kyong Yoo*, et al.*, "Superparamagnetic Iron Oxide Nanoparticles Coated with Galactose-Carrying Polymer for Hepatocyte Targeting," *Journal of Biomedicine and Biotechnology,* vol. 2007, April 2007 2007.

[66] Brown and W. Fuller, "Thermal Fluctuations of a Single-Domain Particle," *Physical Review,* vol. 130, p. 1677, 1963.

[67] W. F. Brown, "Thermal Fluctuations of a Single-Domain Particle," *Physical Review,* vol. 130, p. 1677, 1963.

[68] D. Weller and A. Moser, "Thermal effect limits in ultrahigh density magnetic recording," *IEEE Transactions on Magnetics,* vol. 35, pp. 4423-4439, November 1999.

[69] B. Fischer*, et al.*, "Brownian relaxation of magnetic colloids," *Journal of Magnetism and Magnetic Materials,* vol. 289, pp. 74-77, 2005.

[70] R. E. Rosensweig, "Heating magnetic fluid with alternating magnetic field," *Journal of Magnetism and Magnetic Materials,* vol. 252, pp. 370-374, 2002.

[71] L. v. Michael and et al., "Magnetically induced hyperthermia: size-dependent heating power of Î³-Fe 2 O 3 nanoparticles," *Journal of Physics: Condensed Matter,* vol. 20, p. 204133, 2008.

[72] J. A. Stratton, *Electromagnetic Theory*. New York: McGraw-Hill, 1941.

[73] T. A. Moore and J. A. C. Bland, "Mesofrequency dynamic hysteresis in thin ferromagnetic films," *Journal of Physics: Condensed Matter,* vol. 16, p. R1369, 2004.

[74] M. Suto*, et al.*, "Heat diffusion characteristics of magnetite nanoparticles dispersed hydro-gel in alternating magnetic field," *Journal of Magnetism and Magnetic Materials,* vol. 321, pp. 3483-3487, 2009.

[75] C. A. Sawyer*, et al.*, "Modeling of temperature profile during magnetic thermotherapy for cancer treatment," *Journal of Applied Physics,* vol. 105, pp. 07B320-07B320-3, 2009.

[76] R. Hergt*, et al.*, "Physical limits of hyperthermia using magnetite fine particles," *Magnetics, IEEE Transactions on,* vol. 34, pp. 3745-3754, 1998.

[77] W. Andra*, et al.*, "Temperature distribution as function of time around a small spherical heat source of local magnetic hyperthermia," *Journal of Magnetism and Magnetic Materials,* vol. 194, pp. 197-203, 1999.

[78] E. P. Charles Polk, *Handbook of Biological Effects of Electromagnetic Fields*, 2nd ed.: CRC, December 21, 1995.

[79] L.-Y. Zhang*, et al.*, "Magnetite ferrofluid with high specific absorption rate for application in hyperthermia," *Journal of Magnetism and Magnetic Materials,* vol. 311, pp. 228-233, 2007.

[80] ICNIRP, "Guidelines for limiting exposure to time-varying electric, magnetic, and electromagnetic fields (up to 300 gHz)," *Health Physics,* vol. 74, pp. 494-522, April 1998 1998.

[81] Q. A. Pankhurst, *et al.*, "Applications of magnetic nanoparticles in biomedicine," *Journal of Physics D: Applied Physics,* vol. 36, pp. R167-R181, 2003.

[82] K. Okawa, *et al.*, "Heating ability of magnetite nanobeads with various sizes for magnetic hyperthermia at 120 kHz, a noninvasive frequency," *Journal of Applied Physics,* vol. 99, p. 08H102, 2006.

[83] M. Johannsen, *et al.*, "Clinical hyperthermia of prostate cancer using magnetic nanoparticles: Presentation of a new interstitial technique," *International Journal of Hyperthermia,* vol. 21, pp. 637 - 647, 2005.

[84] R. Hergt and S. Dutz, "Magnetic particle hyperthermia--biophysical limitations of a visionary tumour therapy," *Journal of Magnetism and Magnetic Materials,* vol. 311, pp. 187-192, 2007.

[85] C. N. Marin, *et al.*, "The dependence of the effective anisotropy constant on particle concentration within ferrofluids, measured by magnetic resonance," *Journal of Physics D: Applied Physics,* vol. 34, pp. 1466-1469, 2001.

[86] A. Jordan, *et al.*, "Inductive heating of ferrimagnetic particles and magnetic fluids: Physical evaluation of their potential for hyperthermia," *International Journal of Hyperthermia,* vol. 9, pp. 51 - 68, 1993.

[87] W. J. Atkinson, *et al.*, "Usable Frequencies in Hyperthermia with Thermal Seeds," *IEEE Transactions on Biomedical Engineering,* vol. BME-31, pp. 70-75, 1984.

[88] S. Dutz, *et al.*, "Hysteresis losses of magnetic nanoparticle powders in the single domain size range," *Journal of Magnetism and Magnetic Materials,* vol. 308, pp. 305-312, 2007.

[89] R. A. J. Freitas, *Nanomedicine* vol. Basic Capabilities. Georgetown, TX: Landes Bioscience, 1999.

[90] M. Polson, *et al.*, "Stimulation of nerve trunks with time-varying magnetic fields," *Medical and Biological Engineering and Computing,* vol. 20, pp. 243-244, 1982.

[91] K. S. CS Satish, HG Shivakumar, "Hydrogels as controlled drug delivery systems: Synthesis, crosslinking, water and drug transport mechanism," *Indian J Pharm Sci,* vol. 68, pp. 133-140, 2006.

[92] E. S. Gil and S. M. Hudson, "Stimuli-reponsive polymers and their bioconjugates," *Progress in Polymer Science,* vol. 29, pp. 1173-1222, 2004.

[93] S. Martel, *et al.*, "Automatic navigation of an untethered device in the artery of a living animal using a conventional clinical magnetic resonance imaging system," *Applied Physics Letters,* vol. 90, p. 114105, 2007.

[94] Tabatabaei N., *et al.*, "Magnetic nanoparticles encapsulated in hydrogel as hyperthermic actuators for microrobots designed to operate in the vascular network," presented at the The 2009 IEEE/RSJ International Conference on Intelligent Robots and Systems (IROS), St. Louis, USA, Oct 11-15 2009.

APPENDIX – MATLAB® SIMULATION CODES

A.1 Figure 2.8: Relaxation time vs. Particle size for MNP

```
u_0=pi*4e-7;                            % volts.second/amp/meter
Anisotropy = 2.64e4;                    %J m^-3 for magnetite
Temperature = 297;                      %Kelvin room temperature
Viscosity=1e-3;                         %Pa.s (kg/m/s);
t_0=1e-9;
k=1.38e-23;                             % J/K (Boltzman Constant)(J=w.s)
Density = 5.18;                         %g/cm^3 for Magnetite
Ms_VSM =60;                             %emu/g
Ms = Ms_VSM * Density * 1e3;            %A/m
Coating = 40e-9;                        %meter
Radius = 5e-9:1e-9:10e-9;               %nm

for r=1:length(Radius)

      volume(r) = Volume(Radius(r));

      %%% t_Neel

      GAMMA(r) = Anisotropy * volume(r) / k / Temperature;

      t_Neel(r) = (sqrt(pi) / 2) * t_0 * exp(GAMMA(r))/((GAMMA(r))^(1/2));

      %%%% Brownian relaxation

      volume_hydro(r) = volume(r) * (1 + Coating/Radius(r))^3 ;

      t_Brownian(r) = 3 * Viscosity * volume_hydro(r)/k/Temperature;

      %%% t_effect

      t_effect(r) = t_Neel(r) * t_Brownian(r) /(t_Neel(r) + t_Brownian(r));

end

semilogy (Radius, t_Brownian,'r','Linewidth',3)
hold on
semilogy (Radius, t_Neel,'b','Linewidth',3)
hold on
semilogy (Radius, t_effect,'g','Linewidth',3)

title('Relaxation time vs. Particle size for MNP', 'FontSize',15)
ylabel('\tau(s)','FontSize',15);
xlabel('Particle Radius (m)','FontSize',15);
text(8.6e-9, 1, '\tau_N_e_e_l', 'FontSize',15)
text(5.5e-9, 1e-4, '\tau_B_r_o_w_n_i_a_n', 'FontSize',15)
text(9e-9, 9e-5, '\tau_e_f_f_e_c_t', 'FontSize',15)
```

```
set(gca,'FontSize',14);
grid on
```

A.2 Figure 2.11: Susceptibility components vs. Frequency

```
%%% Stoner-Wohlfarth Losses for small particles

u_0=pi*4e-7;                          % volts.second/amp/meter

Aisotropy = 2.64e4;                   %J m^-3 for magnetite
Temperature = 297;                    %Kelvin room temperature
Viscosity=1e-3;                       %Pa.s (kg/m/s) for ferrofluids
volume_fraction=0.071;                %volume fraction solid
Density = 5.18;                       %g/cm^3 for Magnetite
Ms_VSM =60;                           %emu/g
Ms = Ms_VSM * Density * 1e3           %A/m
Radius = 6e-9;                        %meter
Md = Ms / volume_fraction

volume = Volume(Radius);
Field = 10e3;                         %A/m
Coating = 40e-9;                      %meter
frequency = 0:1e5:1e7;                %Hz


%Hydrodynamic diameter = shell thickness + core diameter + shell thickness =
20 nm + 10 nm + 20 nm = 50 nm


t_Neel = t_Neel(u_0, Anisotropy, Ms,volume,Temperature)
t_Brownian = t_Brownian(Viscosity, volume, Radius, Temperature, Coating)
t_effect = t_effect(t_Neel, t_Brownian);

for f=1:length(frequency)

      Phi(f) = t_effect * 2 * pi * frequency(f);          %dimentionless
      Initial_Susc = Initial_Susceptibility (Ms,volume,volume_fraction,
      Temperature);                                       %dimensionless
      DC_Susc = DC_Susceptibility (Initial_Susc, Field, volume_fraction, Ms ,
      volume,Temperature);
      Susc(f) = Susceptibility (DC_Susc,Phi(f));
      sus_real(f) = DC_Susc / (1+(Phi(f))^2);
      sus_img(f) = Phi(f)* DC_Susc / (1+(Phi(f))^2);

end

semilogx (frequency, sus_img/DC_Susc,'r','Linewidth',3)
hold on
semilogx (frequency, real(sus_real/DC_Susc),'b','Linewidth',3)
title('Susceptibility components vs. Frequency', 'FontSize',15)
ylabel('\chi/\chi_0','FontSize',15);
xlabel('Frequency (Hz)','FontSize',15);
text(7e5, 0.4, '\chi_i_m_a_g_i_n_a_r_y', 'FontSize',15)
text(8e5, 0.8, '\chi_r_e_a_l', 'FontSize',15)
```

```
set(gca,'FontSize',14);
grid on;
```

A.3 Figure 2.13: Time dependent temperature increase as a function of distance

```
%%% Theoretical Estimation for Temperature distribution

% r1 must be >= to t1

clear all
close all

R = 3e-3;                                % meter radius of the spherical volume
P = 6.57*1e6;                            % W/m^3 power

lamda1 = 0.778;                          % W/(K m) heat conductivity medium 1
lamda2 = 0.642;                          % W/(K m) heat conductivity medium 2
q_lamda = lamda2/lamda1;

rho1 = 1.66e6;                           % g/m^3 density medium 1
rho2 = 1e6;                              % g/m^3 density medium 2

c1 = 2.54;                               % J/(g K) heat capacity medium 1
c2 = 3.72;                               % J/(g K) heat capacity medium 2
q = (rho2*c2)/(rho1*c1);

%% detla T1

delta_T1={};

index1 = 1;
vec1 = [];
for t=[30, 60, 120, 300, 3600];

    for r1=1e-4:1e-4:R;

f = @(z) (z^(-2))*exp(((-lamda1)*t*z^2)/(rho1*c1*R^2))*((z*cos(z))-sin(z))/(((
((q_lamda-1)*sin(z))+ (z*cos(z)) )^2)+q_lamda*q*(z*sin(z))^2);
g1 = @(z) sin(r1*z/R);
fXg1=@(z) f(z)*g1(z);
fg1=@(z) arrayfun(fXg1,z);
intfg1 = quad(fg1,0,10);
delta_T1{index1} = (P * R^2 / 3 / lamda2)*(1 + ((q_lamda / 2) *( 1 - r1^ 2 /
R^ 2))  + ( 6 /pi)*q_lamda^(3/2)*q^(1/2)*(R/r1)*intfg1);

        index1 = index1 +1;
    end

    for i=1:index1-1
```

```
        vec1 = [vec1 delta_T1{i}];
    end
    index1 = 1;
end

r1=1e-1:1e-1:3;

plot(r1,vec1(1:30),'Linewidth',2)
hold on;

plot(r1,vec1(31:60),'Linewidth',2)
hold on;

plot(r1,vec1(61:90),'Linewidth',2)
hold on;

plot(r1,vec1(91:120),'Linewidth',2)
hold on;

plot(r1,vec1(121:150),'Linewidth',2)
hold on;

%% delta T2

delta_T2={};

index2 = 1;
vec2 = [];
for t=[30, 60, 120, 300, 3600]

    for r2=R:1e-4:15e-3;

f = @(z) (z^(-2))*exp(((-lamda1)*t*z^2)/(rho1*c1*R^2))*((z*cos(z))-sin(z))/(((
((q_lamda-1)*sin(z))+ (z*cos(z)) )^2)+q_lamda*q*(z*sin(z))^2);
g2 = @(z) ((((q_lamda-1)*sin(z))+ (z*cos(z)))*sin((q/q_lamda)^(1/2)*z*((r2/R)-
1)))+((q_lamda*q)^(1/2)*z*sin(z)*cos((q/q_lamda)^(1/2)*z*((r2/R)-1)));
fXg2=@(z) f(z)*g2(z)/z;
fg2=@(z) arrayfun(fXg2,z);
intfg2 = quad(fg2,0,10);
delta_T2{index2} = (P * R^3 / 3 / lamda2/r2)*(1 + ((6*q_lamda / pi)*intfg2));

        index2 = index2 +1;
    end
    for i=1:index2-1
        vec2 = [vec2 delta_T2{i}];
    end
    index2 = 1;
end

r2=3:1e-1:15;

plot(r2,vec2(1:121),'Linewidth',2)
hold on;
```

```
plot(r2,vec2(122:242),'Linewidth',2)
hold on;

plot(r2,vec2(243:363),'Linewidth',2)
hold on;

plot(r2,vec2(364:484),'Linewidth',2)
hold on;

plot(r2,vec2(485:605),'Linewidth',2)
ylabel('\DeltaT (K)','FontSize',15);
xlabel('r (mm)','FontSize',15);
title('Temperature increase as function of distance','FontSize',14);
text(3,30.7,'---------------------- 3600 s','FontSize',14);
text(3.1,22.62,'---------------------- 3000 s','FontSize',14);
text(3.1,18.82,'---------------------- 120 s','FontSize',14);
text(3.1,15.07,'---------------------- 60 s','FontSize',14);
text(3.2,10,'---------------------- 30 s','FontSize',14);
set(gca,'FontSize',14);
grid on;
```

A.4 Figure 2.15: Power loss due to Neel relaxation vs. radius of MNP

```
%%%%%%%%%%%%%%%%%%%%%%%%%
%%% Grain size dependence
%%% of the loss power denisty
%%% due to Neel-relaxation
%%% for small magnetite
%%%%%%%%%%%%%%%%%%%%%%%%%


%%% SAR_Neel = (u0 f pi x0 (H)^2 2pi f t / [rho (1+(wt)^2)]
%%% w = Angular_Freq
%%% t = t_Neel


clc
clear all


k=1.38e-23;                              % J/K (Boltzman Constant)(J=w.s)
K=1.18e4;                                % Shape anisotropy Fe3O4 J/m^3 aspect
ratio of 1.4
u_0=pi*4e-7;                             % volts.second/amp/meter
Temperature = 273+37;                    % Kelvin (Body temperature)
volume_fraction=0.071;                   % volume fraction solid
Density = 5.18;                          % g/cm^3
H_field = 82.0;                          % Oe = 6.5 kA/m
Magnetization = 40;                      % @ H = 82 Oe, (emu /g)
Ms_emu_g = 90;                           % Magnetization saturation (emu/g)
```

```
Ms = Ms_emu_g * Density * 1e3;          % A/m
t_0 = 1e-10;
Radius = 7e-9:1e-10:12e-9;              % meter
Frequency = [2e4,2e5,2e6];              % Hz

for i=1:length(Radius)


    Volume(i)=4/3 * pi * (Radius(i))^3;                          % m^3
    t_Neel(i) = t_0 * exp(K * Volume(i)/k/Temperature);          % second

    %domain magnetization of a suspended particle
    Md = Ms / volume_fraction;

    %from Langevin relationship:
    Initial_Susc(i) = u_0 * volume_fraction * (Md^2) * volume(i) / 3 / k /
Temperature;

    xi(i) =  u_0* Md * H_field * volume(i) / k / Temperature; %dimensionless
    DC_Susc(i) = Initial_Susc(i) * 3 * (coth (xi(i)) - (1/xi(i))) / xi(i);

    for f=1:length(Frequency)

        Angular_Freq(f) = 2 * pi * Frequency(f);      % radian

        A=u_0*Frequency(f)*H_field^2*pi*DC_Susc(i)*Angular_Freq(f)*t_Neel(i);

        B=1+(Angular_Freq(f)*t_Neel(i))^2;

        SAR(i,f)=A/B/Density/1e6;

    end

end

semilogy (Radius,SAR,'Linewidth',1.5);
ylabel('SAR (W/g)','FontSize',15);
xlabel('Radius (m)','FontSize',15);
text(6.5e-9,3e1,'f = 2x10^6 Hz \rightarrow','FontSize',14);
text(7.6e-9,3,'f = 2x10^5 Hz \rightarrow','FontSize',14);
text(8.2e-9,0.2,'f = 2x10^4 Hz \rightarrow','FontSize',14);
set(gca,'FontSize',14);
%print -djpeg -r300 SARvsParticle_Jpeg_REVISED!!!
```

A.5 Figure 2.16: Biological limitation to field and frequency

```
%%%%%%%%%%%%%%%%%%%%%%%%%%%%%%%%%%%%%%%%
% this will calculate the amount of
% SAR that is absorbed by body tissue
%%%%%%%%%%%%%%%%%%%%%%%%%%%%%%%%%%%%%%%%
%%
```

```
u0 = pi*4e-7;           % permeability of vacuum (H/m)
u  = 100*u0;            % permeability of  (H/m)
Conductivity = 0.6;     % tissue conductivity (ohm^-1 m^-1)
Radius = 10;            % radius of the region EMF is applied on (cm)

density=0.8;            %average tissue density (g/cm^3)

%limitation set by 'Usable Frequencies for Hyperthemria with Thermal
%Seeds' --> 13.56 MHz at 35.8 A/m  for extended time --> 25 mW/ml

Limit = 0.025;          %SAR (W/ml) or (W/cm^3)
                        %Ref: Usable Frequencies in Hyperthermia with
                        %Thermal Seeds: limit H0f <=  4.85x10^8 A/m/s
% The resulting SAR value is
% unlikely to produce a localized temperature increment of
% more than 1°C in the limbs (Chatterjee et al. 1986; Chen
% and Gandhi 1988; Hoque and Gandhi 1988), which has
% been suggested as the upper limit of temperature increase
% that has no detrimental health effects (UNEP/WHO/
% IRPA 1993).
% In general, these have
% demonstrated that exposure for up to 30 min, under
% conditions in which whole-body SAR was less than
% 4 W/kg, caused an increase in the body core temperature
% of less than 1°C.

% Summary of biological effects and epidemiological
% studies (100 kHz–300 GHz)

% Available experimental evidence indicates that the
% exposure of resting humans for approximately 30 min to
% EMF producing a whole-body SAR of between
% 1 and 4 W/kg results in a body temperature increase of
% less than 1 °C. Animal data indicate a threshold for
% behavioral responses in the same SAR range. Exposure
% to more intense fields, producing SAR values in excess
% of 4 W/kg, can overwhelm the thermoregulatory
% capacity of the body and produce harmful levels of tissue
% heating. Many laboratory studies with rodent and nonhuman
% primate models have demonstrated the broad
% range of tissue damage resulting from either partial-body
% or whole-body heating producing temperature rises in
% excess of 1–2°C. The sensitivity of various types of
% tissue to thermal damage varies widely, but the threshold
% for irreversible effects in even the most sensitive tissues
% is greater than 4 W/kg under normal environmental
% conditions. These data form the basis for an occupational
% exposure restriction of 0.4 W/kg, which provides a
% large margin of safety for other limiting conditions such
% as high ambient temperature, humidity, or level of
% physical activity.

%initializing vectors of frequency and field amplitude
freq=[];
field=[];
```

```
H_field=1e3:1e2:10e3;        %initial to final field (A/m)

for i=1:length(H_field)

    A=0;                  %initial to final (Hz)
    B=1e6;
    Frequency=A:1e4:B;


    for ii=1:length(Frequency)


       w(ii) = 2*pi*Frequency(ii);      %angular frequency

       %W/cm^3
       P_N(i,ii) =  1e-
6*(w(ii)^2)*(u0^2)*(Conductivity/8)*(H_field(i))^2*(Radius*1e-2)^2;

       %W/g
       P_N_2(i,ii)=P_N(i,ii)/density;

         if P_N(i,ii) <= Limit && P_N(i,ii) >= (Limit-1e-3)

           freq = [freq; Frequency(ii)];
           field = [field; H_field(i)];


         end

    end

end

plot (freq,field,'LineWidth',2);
grid on;
xlabel('Frequency (Hz)','FontSize',15);
ylabel('Field (A/m)','FontSize',15);
title(['Field vs. Frequency for Loss Power limit of ',num2str(Limit*1000),'
mW/ml'],'FontSize',15)
text(2e5,8000,'Radius of the applied AC magnetic field = 10
cm','FontSize',14);
text(1.6e5,4800,'\leftarrow f = 160 kHz ','FontSize',14);
text(1.9e5,4200,'H = 4.5 kA/m','FontSize',14);
set(gca,'FontSize',14);
```

A.6 Figure 5.3: Time dependent temperature increase as function of distance

```
%%% Theoretical Estimation for Temperature distribution as a function of time
%%% and distancve
clc
clear all

%% Welcome

% r1 must be >= to t1

close all

%%

R_carrier= (50e-6)/2;
R_tumour=(30e-3)/2;

Number_carrier=110000;

V_carrier=4/3*pi*(R_carrier)^3;
V_tumour=4/3*pi*(R_tumour)^3;
V_Total_carrier=Number_carrier*V_carrier;

Percent_tumour_carrier=V_Total_carrier/V_tumour*100;
fprintf(' %0.3f Percent Carrier in Tumour',Percent_tumour_carrier);



percentage_Fe3O4=0.4;                    % 40% magnetite in each micro-carrier

V_Total_Fe3O4=percentage_Fe3O4*V_Total_carrier;

Density= 5.15e6;                         % g/m^3

gramParticle=Density*V_Total_Fe3O4;      % gram

SAR=61.02;                               % W/g

Concentration=gramParticle*1000/(V_tumour*1e6);  %mg/ml
fprintf('\n Concentration: %0.3f mg magnetite/ml Tumour',Concentration)

R = R_tumour;                            % meter radius of the spherical volume
P = SAR*gramParticle/V_tumour;           % W/m^3 power

lamda1 =0.778;                           % W/(K m) heat conductivity magnetite
ferrofluid (ref: Simulation of heat transfer in a ferrofluid using
computational fluid dynamics technique)
lamda2 = 0.642;                          % W/(K m) heat conductivity styrofoam
q_lamda = lamda2/lamda1;
```

```
rho1 = 5.15e6;                          % g/m^3 density magnetite
rho2 = 1e6;                             % tissue g/m^3 density

c1 = 2.54;                              % J/(g K) heat capacity magnetite
c2 = 3.72;                              % J/(g K) heat capacity tissue

q = (rho2*c2)/(rho1*c1);

%% detla T1

delta_T1={};

index1 = 1;
vec1 = [];
for t=[700,1500];

    for r1=1e-4:1e-4:R;

        f = @(z) (z^(-2))*exp(((-lamda1)*t*z^2)/(rho1*c1*R^2))*((z*cos(z))-
sin(z))/((( ((q_lamda-1)*sin(z))+ (z*cos(z)) )^2)+q_lamda*q*(z*sin(z))^2);
        g1 = @(z) sin(r1*z/R);
        fXg1=@(z) f(z)*g1(z);
        fg1=@(z) arrayfun(fXg1,z);
        intfg1 = quad(fg1,0,10);
        delta_T1{index1} = (P * R^2 / 3 / lamda2)*(1 + ((q_lamda / 2) *( 1 -
r1^ 2 / R^ 2))  + ( 6 /pi)*q_lamda^(3/2)*q^(1/2)*(R/r1)*intfg1);

        index1 = index1 +1;
    end


    for i=1:index1-1
        vec1 = [vec1 delta_T1{i}];
    end
    index1 = 1;
end

r1=1e-1:1e-1:15;   %150

plot(r1,vec1(1:150),'Linewidth',2)
hold on;

plot(r1,vec1(151:300),'Linewidth',2)
hold on;

%% delta T2

delta_T2={};

index2 = 1;
vec2 = [];
for t=[700, 1500]
```

```
    for r2=R:1e-4:50e-3;

        f = @(z) (z^(-2))*exp(((-lamda1)*t*z^2)/(rho1*c1*R^2))*((z*cos(z))-
sin(z))/(((  ((q_lamda-1)*sin(z))+ (z*cos(z)) )^2)+q_lamda*q*(z*sin(z))^2);
        g2 = @(z) ((((q_lamda-1)*sin(z))+
(z*cos(z)))*sin((q/q_lamda)^(1/2)*z*((r2/R)-
1)))+((q_lamda*q)^(1/2)*z*sin(z)*cos((q/q_lamda)^(1/2)*z*((r2/R)-1)));
        fXg2=@(z) f(z)*g2(z)/z;
        fg2=@(z) arrayfun(fXg2,z);
        intfg2 = quad(fg2,0,10);
        delta_T2{index2} = (P * R^3 / 3 / lamda2/r2)*(1 + ((6*q_lamda /
pi)*intfg2));

        index2 = index2 +1;
    end


    for i=1:index2-1
        vec2 = [vec2 delta_T2{i}];
    end
    index2 = 1;
end

r2=15:1e-1:50;        %351

plot(r2,vec2(1:351),'Linewidth',2)
hold on;
plot(r2,vec2(352:702),'Linewidth',2)
hold on;

ylabel('\DeltaT (K)','FontSize',15);
xlabel('Radius (mm)','FontSize',15);

text(22,4.5,'SAR = 61.02 W/g','FontSize',14);
text(22,4.1,'No. of micro-carriers = 110,000','FontSize',14);
text(22,3.7,'1.049 mg magnetite / ml Tumour','FontSize',14);
text(16,2.5,'---------------------- 1500 seconds','FontSize',14);
text(16,1.5,'---------------------- 700 seconds','FontSize',14);

set(gca,'FontSize',14);
%grid on;
%print -djpeg -r300 SAR61Time1500No1100000
```